High-Volume-Rate Ultrasound for Quantitative Assessments of Vascular Function

by

Rebekah Dianne Maffett

A thesis

presented to the University of Waterloo

in fulfillment of the

thesis requirement for the degree of

Doctor of Philosophy

in

Electrical and Computer Engineering

Waterloo, Ontario, Canada, 2023

© Rebekah Dianne Maffett 2023

Examining Committee Membership

The following served on the Examining Committee for this thesis. The decision of the Examining Committee is by majority vote.

External Examiner	Dr. Ayache Bouakaz Director of Research, Institut National de la Santé et de la Recherche Médicale (INSERM), France Adjunct Professor, Université de Tours, France
Supervisor	Dr. Alfred C. H. Yu Assistant Vice-President (Research and International), Professor, Department of Electrical and Computer Engineering, University of Waterloo
Internal Member	Dr. Liang-Liang Xie Professor, Department of Electrical and Computer Engineering, University of Waterloo
Internal Member	Dr. George Freeman Professor Emeritus, Department of Electrical and Computer Engineering, University of Waterloo
Internal-External Member	Dr. Richard Hughson Schlegel Research Chair in Vascular Again and Brain Health, Senior Director of Research, Research Institute for Aging Professor Emeritus, Department of Kinesiology and Health Sciences, University of Waterloo

Author’s Declaration

This thesis consists of material all of which I authored or co-authored: see Statement of Contributions included in the thesis. This is a true copy of the thesis, including any required final revisions, as accepted by my examiners.

I understand that my thesis may be made electronically available to the public.

Statement of Contributions

Chapters 1, 2, and 7: Rebekah Maffett was the sole author.

Chapter 3 presents material from a manuscript entitled "Chirp-Based Velocity Estimation (ChiVE): A Framework for Enhanced Flow Imaging with Wideband Transmissions" which is being prepared for submission to *IEEE Transactions of Ultrasonics, Ferroelectrics, and Frequency Control*, and is co-authored by Rebekah Maffett, Billy Y. S. Yiu, and Alfred Yu. Rebekah Maffett designed the algorithmic framework, performed all experiments, analyzed the data, and wrote the first draft of the manuscript. Billy Y. S. Yiu assisted in the framework design, provided technical feedback, and edited the manuscript draft. Alfred C. H. Yu supervised the work and reviewed the results.

Chapter 4 presents material from an article entitled "Unfocused Field Analysis of a Density-Tapered Spiral Array for High-Volume-Rate 3-D Ultrasound Imaging" which has been published in *IEEE Transactions of Ultrasonics, Ferroelectrics, and Frequency Control* © IEEE 2022. This article was co-authored by Rebekah Maffett, Enrico Boni, Adrian J. Y. Chee, Billy Y. S. Yiu, Alessandro S. Savoia, Alessandro Ramalli, Piero Tortoli, and Alfred C. H. Yu. Rebekah Maffett planned and performed all experiments, analyzed the data, and wrote the first draft of the manuscript. Enrico Boni assisted in the experimental design and reviewed the experimental results. Adrian J. Y. Chee and Billy Y. S. Yiu provided experimental guidance and reviewed the results. Alessandro S. Savoia and Alessandro Ramalli fabricated and designed the probe, respectively. Piero Tortoli and Alfred C. H. Yu co-supervised the work and reviewed the results. All authors reviewed the manuscript prior to publication.

Chapter 5 presents material from a manuscript entitled "The Effects of Transmission Scheme on 3D Vector Flow Imaging Performance" which is being prepared for submission to *IEEE Transactions of Ultrasonics, Ferroelectrics, and Frequency Control*, and is co-authored by Rebekah Maffett, Billy Y. S. Yiu, and Alfred C. H. Yu. Rebekah Maffett derived and implemented the velocity estimation pipeline, designed the parametric sweep, performed all experiments, analyzed the data, and wrote the first draft of the manuscript. Billy Y. S. Yiu provided technical feedback and reviewed the experimental results. Alfred C. H. Yu supervised the work and reviewed the results.

Chapter 6 presents material from a manuscript entitled "A Volumetric Blood Flow Estimation Framework for a Portable Ultrasound System" which is being prepared for submission to *Medical Physics*, and is co-authored by Rebekah Maffett, Hassan Nahas, Billy Y. S. Yiu, and Alfred C. H. Yu.

Rebekah Maffett implemented the volume flow estimation framework, performed all experiments, analyzed the data, and wrote the first draft of the manuscript. Hassan Nahas configured the ultrasound scanner for the 2D matrix array. Billy Y. S. Yiu provided technical feedback and reviewed the results. Alfred C. H. Yu supervised the work and reviewed the results.

Abstract

Free flap surgery is a common reconstructive technique to repair tissue damage after trauma or cancer removal. This complex procedure involves the transfer of tissue, along with its associated blood supply, from one part of the body to another. While these surgeries have high overall success rates, the risk of vascular complications remains a concern. Thus, rigorous post-operative vascular monitoring of free flaps is required for the early detection and intervention of complications to prevent tissue necrosis or complete flap failure. Despite the critical importance of vascular monitoring, clinicians do not currently have an objective measurement tool that can quantify the volume of blood perfusing the flap. Instead, they rely on tools which indicate the presence or absence of blood flow (e.g. Doppler pens) coupled with visual inspection of the flap. As a result, vascular compromise can go unnoticed for several hours which increases the risk of partial or total flap failure.

Ultrasound imaging is a potential solution to the vascular monitoring of free flaps given its ability to accurately measure blood flow velocities at the bedside. However, the accurate quantification of blood flow volumes requires the use of high-volume-rate 3D ultrasound imaging which generally lacks bedside applicability due to the large size of the associated processing electronics. The goal of this thesis is to investigate novel solutions which enable the acquisition of accurate 3D flow measurements with portable ultrasound systems. Specifically, this work has two primary focal points: 1) the investigation and validation of data reduction strategies for 3D ultrasound to facilitate the use of portable processing systems, and 2) the enhancement of high-rate ultrasound flow estimation accuracy to optimize the performance of volumetric blood flow measurements. At the end of this work, the first *in vivo* volumetric blood flow measurement with a portable 3D ultrasound system is showcased.

Overall, this thesis presents several advances on the state-of-the-art of 3D ultrasound flow imaging technology. The capabilities of small-scale 3D ultrasound technology are demonstrated indicating a positive outlook for future clinical applications. Indeed, the core focus of this work on accurate blood flow quantification is to ensure that clinicians have access to reliable, quantitative data enabling them to make objective decisions on patient care. In the case of free flap vascular monitoring, 3D ultrasound has the potential to significantly improve the early detection of vascular complications which could mitigate the need for additional surgeries and reduce the rates of partial and total flap failures.

Acknowledgements

On our annual family mountain biking trip when I was about 12 years old, my oldest brother flew over his handlebars and hurt himself (not that bad, don't worry). Being the helpful little sister I was (am), I proceeded to offer unsolicited and entirely unhelpful medical advice that earned me the family nickname of "The Doctor" for many years following. Now here we are at the end of a self-fulfilling prophecy 16 years in the making. But of course, we would not be here if it were not for some very important people that need to be acknowledged and thanked.

The first of whom is Prof. Alfred Yu, a supervisor who has taught me so much over the past five years. His ability to identify my weaknesses and help me turn them into strengths is something I will always be grateful for.

Next, I need to thank my many lab mates who have provided endless laughs, support, and coffee over the years. I would like to thank Adrian Chee and Billy Yiu whose mentorship was invaluable to my development. I would also like to thank Jason Hsu and Chris Kallweit for coming to the lab and making the strange early days post-Covid so much more fun. Lastly, I need to thank Yanyan Tran for providing solidarity as we struggled on this thesis writing journey in parallel over the past few months.

I also owe many thanks to my second lab at the University of Florence and especially Prof. Piero Tortoli for welcoming me and being a wonderful mentor.

Thank you as well to my family, my parents, my brothers, and my sister. They have all heard way more than they ever wanted to know about ultrasound and I am grateful for their love and support.

I also need to thank a very special trio in my life: Chloe, Sarge, and Oscar. Their unconditional love has got me through many hard times and for that I owe them endless treats and scritches.

Lastly, I would like to thank my best friend and dearest husband, Micah. He is the most supportive person I have ever met, and I am beyond lucky to have him by my side in this life. I truly do not think I could have made it this far without him. I cannot wait to see what the rest of our journey holds.

Table of Contents

Examining Committee Membership ii

Author's Declaration iii

Statement of Contributions iv

Abstract vi

Acknowledgements vii

List of Figures xiv

List of Tables xviii

List of Abbreviations xix

List of Symbols xxii

Chapter 1 Introduction 1

1.1 Clinical Motivation 1

1.1.1 Post-Operative Complications of Free Flaps 1

1.1.2 Monitoring of Vascular Function in Free Flaps 2

1.1.3 Ultrasound as a Solution for Free Flap Monitoring 3

1.2 Research Objectives 4

1.2.1 Objective 1: Increasing SNR of High-Frame-Rate Flow Estimations 4

1.2.2 Objective 2: Assessing Sparse Array Feasibility for High-Volume-Rate Ultrasound Imaging 5

1.2.3 Objective 3: Optimizing High-Volume-Rate Ultrasound Acquisitions for High Performance Velocity Estimations 5

1.2.4 Objective 4: Devising a VBF Estimator Using a Portable Ultrasound Scanner 6

1.3 Thesis Outline 6

Chapter 2 Background 8

2.1 Ultrasound Imaging for Free Flap Monitoring 8
2.1.1 Ultrasound Image Formation 8
2.1.2 Pulsed Wave Doppler Ultrasound 10
2.1.3 Ultrasound Color Flow Imaging 12
2.2 High-Frame-Rate Ultrasound for Enhanced Flow Estimations 13
2.2.1 Multi-Angle Doppler Ultrasound 14
2.2.2 Limitations of High-Frame-Rate Ultrasound 15
2.3 High-Volume-Rate Ultrasound: The Next Generation of Ultrasound Flow Estimation 15
2.3.1 Novel Array Designs 16
2.3.2 Reduced Receive Systems 18
2.3.3 Limitations of High-Volume-Rate Ultrasound 18
Chapter 3 Chirp-Based Velocity Estimation (ChiVE): A Framework for Enhanced Flow Imaging with Wideband Transmissions 20
3.1 Introduction 20
3.2 ChiVE Framework 22
3.2.1 RF-Doppler Frequency Domain Conversion 24
3.2.2 Mean Slope Estimation and Aliasing Detection 24
3.2.3 Modal Velocity Estimation 25
3.3 Imaging Methods 27
3.3.1 Transmission Parameters 27
3.3.2 Pre-Filtering, Pulse Compression, Beamforming, and Clutter Filtering 28
3.4 Experimental Methods 29
3.4.1 Straight Tube Phantom Studies 29
3.4.2 Stenosed Carotid Bifurcation Phantom Experiments 32

3.5 Results 34
3.5.1 Chirp Transmissions Enhance Doppler SNR Over Standard Transmissions 34
3.5.2 ChiVE Produces Aliasing Resistant Parabolic Velocity Profiles with Reduced RMSE 34
3.5.3 ChiVE Maintained Performance in a Reduced SNR Scenario 36
3.5.4 ChiVE Can Map Dynamic Flows Across the Cardiac Cycle 37
3.6 Discussion 38
3.6.1 Statement of Contribution 38
3.6.2 Interpretation of Results 40
3.6.3 Limitations and Future Work 41
3.7 Conclusions 42
Chapter 4 Unfocused Field Analysis of a Density-Tapered Spiral Array for High-Volume-Rate 3-D Ultrasound Imaging 43
4.1 Introduction 43
4.2 Experimental Methods 45
4.2.1 Hydrophone Measurements 48
4.2.2 Field Profile Simulations 49
4.2.3 Intensity Analysis 49
4.2.4 Arrival Time Analysis 49
4.2.5 In Vitro B-Mode Imaging 50
4.2.6 Probe Surface Temperature Measurements 51
4.3 Results 51
4.3.1 Spiral Array Produces High-Quality Beam Profiles for Unfocused Firings 51
4.3.2 Wavefronts Generated from the Spiral Array Match the Expected Profiles 53

4.3.3 Compounded Unfocused Firings Demonstrated High B-Mode Spatial Resolution with Limited Penetration Depth 56
4.3.4 Surface Temperature and Acoustic Exposure Levels are Within Regulatory Limits 58
4.4 Discussion 59
4.4.1 Statement of Contributions 59
4.4.2 Summative Interpretation of Findings 60
4.4.3 Limitations and Future Work 61
4.5 Conclusion 63
Chapter 5 The Effects of Transmission Scheme on 3D Vector Flow Imaging Performance 64
5.1 Introduction 64
5.2 Methods 65
5.2.1 3D Multi-Angle Least-Squares VFI Derivation 65
5.2.2 Imaging Methods 68
5.2.3 Experimental Methods 69
5.3 Results 72
5.3.1 Azimuth Angle Span is the Strongest Factor in 3D VFI Performance 72
5.3.2 Axial Flow is the Most Accurately Estimated in Multi-Directional Flow Profiles 77
5.3.3 3D VFI Maps Complex and Dynamic Flows 81
5.4 Discussion 83
5.4.1 Statement of Contributions 83
5.4.2 Summative Interpretation of Findings 84
5.4.3 Limitations and Future Work 86
5.5 Conclusions 87
Chapter 6 A Volumetric Blood Flow Estimation Framework for a Portable Ultrasound System 89

6.1 Introduction 89
6.2 Methods 90
6.2.1 Imaging Sequence and Methods 91
6.2.2 VBF Estimation Algorithm 93
6.2.3 Experimental Methods 94
6.3 Results 96
6.3.1 Constant Straight Tube VBF is Precisely Estimated with an Offset from the True Value 96
6.3.2 Estimated Pulsatile VBF Profile Aligns with the Clinical Velocity Profile 96
6.3.3 Multi-Directional VBF is Well-Estimated at Shallow Depths 97
6.3.4 *In Vivo* Volumetric Flows Agree with the Clinical Velocity Profile 99
6.4 Discussion 99
6.4.1 Statement of Contributions 99
6.4.2 Summative Interpretation of Findings 102
6.4.3 Limitations and Future Work 103
6.5 Conclusions 104
Chapter 7 Summary of Contributions and Future Research Directions 105
7.1 Summary of Thesis 105
7.1.1 Specific Contribution 1: Enhanced Flow Estimations with Wideband Transmissions 108
7.1.2 Specific Contribution 2: 3D VFI with a Sparse Array 108
7.1.3 Specific Contribution 3: VBF Estimation on a Portable Ultrasound System 110
7.2 Future Research Directions 111
7.2.1 Extension of ChiVE to 3D Ultrasound 111
7.2.2 Calibration of VBF Estimations 111
7.2.3 Visualization of 3D Ultrasound 112

7.2.4 Wearable Ultrasound for Continuous Monitoring 112

References 114

Appendix A List of Movies 129

Appendix B Full Table of RMSE Values from 3D VFI Parametric Sweep 130

List of Figures

Figure 2-1 Diagram of scanline, plane wave, and diverging wave imaging. 10

Figure 2-2 Diagram of pulsed Doppler imaging. 11

Figure 3-1 Schematic of the ChiVE framework 23

Figure 3-2 Schematic of the straight tube flow experiment setup. 30

Figure 3-3 Color flow images at (a-d) 7mL/s flow rate and (e-h) 13mL/s flow rate for each of the four tested transmissions. 32

Figure 3-4 Flow profiles from flow rates ranging from 3 to 13mL/s including the ChiVE flow estimation with the CH6 transmission, lag-one autocorrelation with the ST5 transmission, and the ideal flow profile. 33

Figure 3-5 RMSE box-whisker plots for (a-c) 3, (d-f) 5, (g-i) 7, and (j-l) 9mL/s at three vessel cross-sections (x = -10, 0, 10mm) for lag-one autocorrelation, ChiVE at three transmission bandwidths, and ChiVE with the modal velocity estimator (radon transform step) removed. 35

Figure 3-6 Flow profiles at 7mL/s flow rate with (a) 166kPa transmission pressure and (b) 286kPa transmission pressure. 36

Figure 3-7 RMSE box-whisker plot for 7mL/s flow rate with (a) 166kPa transmission pressure and (b) 286kPa transmission pressure. 37

Figure 3-8 Snapshots from Movie 3-1 (a) and (b) at systole for ChiVE and lag-one autocorrelation respectively and (c) and (d) at diastole. 38

Figure 3-9 Doppler spectrogram of the carotid bifurcation phantom flow from a range gate in the center of the stenosed region for the ST5 pulse. 39

Figure 4-1 Layout of the physical CMUT density tapered spiral array with hexagonal elements. 45

Figure 4-2 Schematic of diverging wave steering. 46

Figure 4-3 Diagrams of the hydrophone acquisition planes. 47

Figure 4-4 Intensity measurements for PW (left column), DIV30, (center column), and DIV20 (right column) for 0 and 1° steering (top row), 5° steering (second row), and 10° steering (third row). 52

Figure 4-5 Intensity measurements on XY-planes at a depth of 40 mm in hydrophone experiments (top row) and simulation (bottom row) for PW (left), DIV30 (center), and DIV20 (right). 53

Figure 4-6 Top row: Overlayed stills from Movie 4-1 at 5, 15, and 25μs from the start of the acquisition on the oscilloscope for unsteered PW (a), DIV30 (b), and DIV20 (c) firings. Bottom row: Overlayed stills from Movie 4-2 at the same timepoints as the top row for PW (d), DIV30 (e), and DIV20 (f) firings steered at 10°. 54

Figure 4-7 Cross sectional wavefront profiles for PW (left), DIV30 (center), and DIV20 (right) for 0 and 1° steering (top), 5° steering (middle), and 10° steering (bottom) at a depth of 40 mm. 55

Figure 4-8 B-mode images of point targets in a CIRS phantom formed by the coherent compounding of 10 unfocused transmissions (steering -5° to 5° along the x-axis). 56

Figure 4-9 B-mode images of point targets in an in-house made wire target phantom immersed in water formed by the coherent compounding of 10 unfocused transmissions (steering -5° to 5° along the x-axis). 57

Figure 4-10 Contour plots of the B-mode images of the point targets in water for (a) PW scan [Figure 4-9(a)] and (b) DIV20 scan [Figure 4-9(c)] with thresholds of -20, -12, and -6dB to highlight the sidelobe intensity levels. 58

Figure 4-11 Infrared image of the probe surface acquired after 30 minutes of continuous transmission. 58

Figure 5-1 Definitions of transmission elevational (θ) and azimuthal (γ) steering angles. The same definitions apply for the receive steering elevation (ϕ) and azimuth (ζ) angles. 66

Figure 5-2 Relative probe-flow orientations in straight tube experiments. 70

Figure 5-3 Lumen geometry of the helix phantom. 71

Figure 5-4 (a) Top view and (b) side view of the aneurysm phantom lumen. 72

Figure 5-5 Flow magnitude surface plots for 6 transmission angles with 5° elevational steering and (a)-(d) 75° and (e)-(h) 300° azimuthal steering. 73

Figure 1-1 Flow magnitude surface plots for 6 transmission angles with 300° azimuthal steering and (a)-(d) 7.5° and (e)-(h) 10° elevational steering. 75

Figure 5-7 Flow magnitude surface plots for 5° elevational steering and 300° azimuthal steering with (a)-(d) 3 and (e)-(h) 9 transmission angles. 76

Figure 5-8 RMSE plots for all tested transmission combinations for (a)-(c) 2mL/s flow in a 2mm ID vessel with 5, 7.5, and 10° elevational steering, respectively. (d)-(f) RMSE plots for 2mL/s flow in a 3.5mm ID vessel at the same elevation angles, respectively. 77

Figure 5-9 Velocity vectors planes from the helix phantom measured by 3D VFI. 78

Figure 5-10 Ultrasound measured and CFD flow vector components on three slices of the helix phantom. 79

Figure 5-11 Error magnitude of measured velocity vectors compared to CFD for each flow vector component on the (a) upward slice, (b) downward slice, and (c) lateral slice of the helix phantom. 80

Figure 5-12 Still frames from the dynamic vector flow in the aneurysm phantom (Movie 5-1). 82

Figure 6-1 Schematic of the transmission scheme and VBF estimation pipeline. 91

Figure 6-2 Schematic and voltages of the 2D matrix array. 92

Figure 6-3 Schematic of the helical toroid phantom from a top view (left), end view (center), and side view (right) 95

Figure 6-4 *in vitro* carotid pulse from (a) a clinical ultrasound scanner Doppler spectrogram and (b) the VBF estimation framework. 97

Figure 6-5 Approximate measurement plane locations on the helical toroid phantom. 98

Figure 6-6 Error of VBF measurements in the helical toroid phantom versus measurement depth. 99

Figure 6-7 Measurements of the in vivo brachial artery flow. 100

List of Tables

Table 3-1 Transmission parameters 26

Table 3-2 Pre-beamforming bandpass filter parameters 26

Table 3-3 Beamforming resolution 28

Table 4-1 Transmission, measurement, and medium properties 46

Table 5-1 List of elevation and azimuth angles used in 3D VFI optimization 68

Table 5-2 Transmit azimuth angle steering combinations used for 3D VFI 69

Table 5-3 Directional error on each of the helix phantom slices 81

Table 6-1 VBF measurement results from straight tube experiments 96

Table 6-2 VBF measurement results from the helical toroid phantom experiments 98

List of Abbreviations

2D	Two dimensional
3D	Three dimensional
ASIC	Application specific integrated circuit
B-mode	Brightness mode
BMF	Blood mimicking fluid
CFD	Computational fluid dynamics
CFI	Color flow imaging
CH2/CH4/CH6	Chirp pulses with 2, 4, and 6MHz bandwidth (Chapter 3)
ChiVE	Chirp-based velocity estimation
CMUT	Capacitive micromachined ultrasound transducer
CT	Computed tomography
DAS	Delay-and-sum
DIV20/DIV30	Diverging wave with virtual point source 20mm/30mm behind array (Chapter 4)
FDA	Food and Drug Administration
FFT	Fast-Fourier transform
FIR	Finite impulse response
FWHM	Full-width half-maximum
HiFRUS	High-frame-rate ultrasound
ICA	Internal carotid artery
ICU	Intensive care unit
ID	Inner diameter

MAE	Mean absolute error
MB	Microbubbles
MCA	Middle cerebral artery
MI	Mechanical index
MRI	Magnetic resonance imaging
PCA	Posterior communicating artery
PIV	Particle image velocimetry
PPG	Photoplethysmogram
PRF	Pulse repetition frequency
PRI	Pulse repetition interval
PVA	Poly-vinyl alcohol
PW	Plane wave
PWD	Pulsed wave Doppler
RCA	Row-column addressed
RF	Radio frequency
RMSE	Root mean squared error
Rx	Receive
SD	Standard deviation
SLL	Side lobe level
SNR	Signal-to-noise ratio
SPPA	Spatial peak, pulse average
ST5	Standard sinusoidal pulse with 5MHz center frequency (Chapter 3)
Tx	Transmit

VBF	Volumetric blood flow
VFI	Vector flow imaging
vps	Volumes per second

List of Symbols

γ	Receive elevation steering
$\Delta\psi$	Slow-time phase shift
ζ	Receive azimuth steering
θ	Transmit elevation steering
λ	Wavelength
σ	Beam-flow angle
ϕ	Transmit azimuth steering
$\mathbf{A}$	Angle matrix of multi-angle vector Doppler estimators
A	Number of transmit angles (Chapter 6)
c	Speed of sound
f_d	Doppler frequency
f_{DAQ}	Data acquisition frequency (effective PRF)
f_{PRF}	Pulse repetition frequency
f_{RF}	Ultrasound transmission center frequency
$\boldsymbol{g}$	Temporal range gate matrix (Chapter 3)
$\boldsymbol{G}$	Frequency-domain range gate matrix (Chapter 3)
K	Number of slow-time frames in range gate matrix (Chapter 3)
m	Radon transform projection angle (Chapter 3)
M	Number of transmit angles (Chapter 5) Number of RF frames (Chapter 6)
N	Number of fast-time pixels in range gate matrix (Chapter 3) Number of reception angles (Chapter 5)

$\hat{\mathbf{R}}$	Receive unit vector (Chapter 5)
S	Slow-time signal
t	Time
$\hat{\mathbf{T}}$	Transmit unit vector (Chapter 5)
T_{PRI}	Pulse repetition interval
$\mathbf{u}$	Mean frequency measurand vector
$\mathbf{v}$	Velocity vector
v	Velocity
v_x	Velocity x-component
v_y	Velocity y-component
v_z	Velocity z-component (axial)
$\hat{\mathbf{x}}$, $\hat{\mathbf{y}}$, $\hat{\mathbf{z}}$	Axes unit vectors
x_o, y_o, z_o	Spatial coordinates of the array elements (Chapter 4)
x_{vp}, y_{vp}, z_{vp}	Spatial coordinates of the virtual point source (Chapter 4)

Chapter 1
Introduction

1.1 Clinical Motivation

Reconstructive surgery is a form of plastic surgery that is used to rebuild portions of the body that have been impacted by diseases or injury (John Hopkins Medicine, 2023). In cases of extensive tissue damage or removal, the use of a "free flap" may be required to repair the tissue defects, recover functionality, and improve appearance (Icahn School of Medicine at Mount Sinai, 2019, Saber et al., 2022). Free flaps are donor tissues which have their blood supply severed from the donor site and re-attached at the recipient site through advanced microvascular surgical techniques. This is in contrast to tissue grafts which rely on natural revascularization of the donor tissue post-surgery and do not require the detachment and reconnection of donor blood vessels. Free flaps also differ from other flap types such as local, rotator, or pedicled flaps which are used when the blood vessels can remain intact between the donor and recipient sites. Thus, free flaps are the surgical method of choice for the repair of large defects which require significant blood perfusion as well as defects that do not have a suitable tissue donor nearby (i.e. the donor flap must be taken from a distant part of the body and the blood vessels must be severed). While free flaps can be composed of a single tissue type, they are commonly compound tissues containing any combination of skin, fat, muscle, and even bone (Icahn School of Medicine at Mount Sinai, 2019, Saber et al., 2022).

Reconstructive surgeons have a higher proclivity for the use of free flaps in specific disease and injury conditions. Indeed, one of the most common applications of free flap surgery is in breast cancer patients for reconstruction after mastectomies due to the size and compound nature of the required donor tissue (Saaristo et al., 2012, Rose & Puckett, 2023). Another common application is for head and neck cancer patients after tumor excision which requires complex surgical planning and has a high emphasis on the resulting appearance (Başaran et al., 2021). Aside from cancer, free flaps are also used for repair after trauma in both the upper (Bullocks et al., 2006, Koepple et al., 2019) and lower (Khundkar, 2019, Alam Atiq et al., 2020) extremities and, less commonly, in patients suffering from acute or secondary burns (Brewin et al., 2020, Jabir et al., 2015).

1.1.1 Post-Operative Complications of Free Flaps

Despite the many advances in surgical planning and methodologies, the rate of post-surgical complications remains high and there is a non-negligible risk of flap failure. For free flap surgeries, the

rate of complications generally ranges from 20-40% (Rose & Puckett, 2023, Allam et al., 2022, Lese et al., 2021) with complications being more common in maxillofacial surgeries (up to 70%; Denis et al., 2022). In about 5% of free flap surgeries (7% in maxillofacial surgeries) the flap undergoes total failure requiring the removal and disposal of the donor tissue (Kwok & Agarwal, 2017, Pohlenz et al., 2012). Moreover, even without a complete failure of the flap, 5-25% of complications require the surgical re-exploration of the flap (Bui et al., 2007, Salgado et al., 2009). Aside from infections and systemic complications (e.g. pneumonia), many complications are directly related to the vascular function of the flap including thrombosis, compressive occlusion, hematoma, or bleeding (Bui et al., 2007, Pohlenz et al., 2012). Even simple clinical errors such as overly tight bandages or wound closures increase the risk of vascular occlusion (Pohlenz et al., 2012). Vascular complications reduce or fully eliminate the perfusion of blood in the flap tissue which, without rapid intervention, can lead to tissue necrosis and partial or total flap failure. Furthermore, larger flaps require increased perfusion and are more at risk to vascular complications and tissue necrosis without deliberate surgical planning to increase the blood supply (Lee & Mun, 2016). While there are clinical predictors of patients at risk for post-surgical vascular complications (Lese et al., 2021), the most important factor in identifying (and ideally saving) flaps with vascular complications is extensive post-surgical monitoring by skilled clinicians (Chen et al., 2007, Salgado et al., 2009).

1.1.2 Monitoring of Vascular Function in Free Flaps

The post-operative vascular monitoring of free flaps is crucial to the success of the procedure and must be performed diligently. In most cases, patients are admitted to an intensive care unit (ICU) for recovery immediately following the procedure enabling frequent check-ins, however, there is no established universal protocol for the monitoring of free flaps. The most widely used monitoring technique utilizes Doppler pens to detect the presence of blood flow in the major vessels of the flap (Salgado et al., 2009, Knoedler et al., 2023). Doppler pens are ultrasonic devices that leverage the Doppler effect to measure the movement of acoustic scatterers (including red blood cells) and output an audible Doppler signal to the user. Alternative or supplementary methods of monitoring leverage visual inspection, temperature, blood oxygenation, tissue pH, laser Doppler, or any combination thereof (Salgado et al., 2009). Regardless of the technology being used, most centers follow a strict timeline for monitoring depending on how many hours have passed since the operation. A typical example of such a timeline is:

0 to 24 hours – Monitoring every 30 minutes.

24 to 48 hours – Monitoring every 60 minutes.

48 to 72 hours – Monitoring every 4 hours.

>72 hours – Monitoring every 8-12 hours.

Unfortunately, there remains a critical flaw in the available tools for vascular monitoring no matter how frequently they are applied. None of the existing technologies provide a quantitative, repeatable, and direct measurement of the underlying outcome of vascular complications: the volume of blood passing in and out of the tissue flap. Indeed, both clinicians and researchers have called for novel techniques that would provide a more clear-cut measurement of flap perfusion with minimal user dependence (Salgado et al., 2009, Chao et al., 2013, Knoedler et al., 2023).

1.1.3 Ultrasound as a Solution for Free Flap Monitoring

Given its bedside applicability (Díaz-Gómez et al., 2021), ultrasound imaging is a potential candidate for the post-operative monitoring of free flaps in the ICU. In fact, ultrasound color flow imaging (CFI) has already been used in multiple quantitative research studies on flaps (Dusseldorp & Pennington, 2014, Steenbeek et al., 2022, Rubino et al., 2009). However, clinical ultrasound systems are typically 2-dimensional (2D) while volumetric blood flow (VBF) is an inherently 3-dimensional (3D) quantity resulting in the need to perform multiple 2D scans to estimate its value. Additionally, several approximations about the flow and vessel characteristics are also required for the calculation. The procedure for estimating VBF from 2D ultrasound is effectively the same today as it was in the 1990s where studies questioned the accuracy of the method (Rubin, 1999, Hussain et al., 1996). A recent study on modern scanners indicates that these estimations can be reasonably accurate (at least *in vitro*), however they also acknowledge the need for updated methodologies (Hoyt et al., 2009).

The most logical solution to accurate VBF measurements with ultrasound imaging is to use 3D ultrasound instead of 2D, yet there are many roadblocks to the implementation of bedside 3D ultrasound flow imaging. Currently, clinical 3D ultrasound systems are limited to extremely low volume rates (<10Hz) which are not suitable for flow imaging. Additionally, research scanners capable of high-volume-rate imaging (up to 10kHz) are typically very large systems that are not suitable for bedside clinical applications (Jensen et al., 2013, Petrusca et al., 2018). Smaller scale solutions on the other hand suffer from reduced signal-to-noise ratios (SNRs) or lower temporal sampling (Roux et al., 2018, Sauvage et al., 2018). Because of these challenges, little research has been performed to optimize flow

estimation performance in 3D ultrasound leaving the reliability of resultant VBF estimations uncertain. Certainly, there remains a significant technological gap between the current state of 3D ultrasound and accurate bedside VBF monitoring using 3D ultrasound that must be addressed.

1.2 Research Objectives

To reliably measure VBF with 3D ultrasound at the bedside, a portable ultrasound system with improved SNR and optimized acquisition schemes needs to be developed. Ideally, such a system would be similarly sized to modern 2D ultrasound scanners and have comparable data rates. To this end, the following research objectives are pursued in this thesis:

1) To increase the SNR of ultrasound flow estimation by designing a novel framework centered around existing signal enhancement strategies.
2) To investigate the feasibility of 3D ultrasound data reduction with sparse transducer arrays that utilize similar channel counts to modern 2D ultrasound systems.
3) To optimize the high-volume-rate ultrasound acquisition scheme for maximized velocity estimation accuracy and minimized velocity estimation variance.
4) To devise a framework for estimating VBF from 3D ultrasound flow estimations acquired from a portable ultrasound system.

Each of these research objectives addresses a critical problem in the development of bedside 3D ultrasound for reliable VBF estimations. By addressing these problems, 3D ultrasound technology moves closer to the potential application to VBF monitoring in free flaps. The following subsections provide a high-level overview of the problems driving these research objectives and how the objectives themselves are approached in this thesis.

1.2.1 Objective 1: Increasing SNR of High-Frame-Rate Flow Estimations

High-rate ultrasound imaging, both in 2D and in 3D, is well known for its ability to resolve dynamic flows with high temporal resolution (Tanter & Fink, 2014); however, the benefits of dynamic imaging come at a direct trade-off with the SNR of the images. Low SNR flow estimates have generally increased variances which will in turn result in less reliable VBF estimations. Thus, there is a distinct need for SNR enhancement if a robust VBF estimation platform is to be realized. Ultrasound signal enhancement can be realized using coded excitations which are typically long-duration transmissions that can be compressed upon reception to preserve spatial resolution while increasing the intensity of

the echoes (Misaridis & Jensen, 2005a). Yet, coded excitations have long been considered incompatible with traditional ultrasound flow imaging (Misaridis & Jensen, 2005a). To address this incompatibility, a novel ultrasound flow estimation framework is described in **Chapter 3** that is specifically designed for use with coded transmissions. This framework not only increases the SNR of the flow signal, but also enhances the velocity estimation accuracy and extends the velocity estimation range.

1.2.2 Objective 2: Assessing Sparse Array Feasibility for High-Volume-Rate Ultrasound Imaging

High-volume-rate ultrasound imaging with fully populated matrix transducer arrays can produce data rates approaching 50GB/s which limits its implementation to powerful, large-scale scanners that do not fit the point-of-care ultrasound paradigm (Jensen et al., 2013, Petrusca et al., 2018). Reducing this immense data rate, thereby enabling the use of portable scanners, is possible by employing sparsely populated transducer arrays which reduce the element count and in turn the amount of raw data collected. However, the transmission characteristics of sparse arrays have yet to be established in high-volume-rate imaging schemes making their ability to accurately estimate flow velocities uncertain. Hence, a rigorous analysis of the transmission performance of a sparse array in high-volume-rate imaging schemes is presented in **Chapter 4**. This investigation demonstrates the adequate capability of sparse arrays and suggests that they are suited for high-volume-rate imaging applications including flow estimation.

1.2.3 Objective 3: Optimizing High-Volume-Rate Ultrasound Acquisitions for High Performance Velocity Estimations

Ultrasound flow estimations can be acquired along multiple directions at high-volume-rates with the use of steered transmissions. By collecting multi-directional estimates, the velocity vectors of the underlying flow can be deduced. In 2D ultrasound, studies have shown that the combination of steered transmissions directly impacts the flow vector estimation performance (Yiu & Yu, 2016). In 3D ultrasound, no such analysis has been performed to account for the additional degree of freedom in the beam steering and as such recent studies may have sub-optimal performance for their given system (Rossi et al., 2020, Holbek et al., 2017a, Holbek et al., 2017b, Correia et al., 2016, Correia et al., 2020). While these studies have shown reasonable performance, the potential use of excessive transmissions sacrifices the achievable velocity estimation limit. Therefore, velocity estimation accuracy is quantified in a parametric sweep of transmission sequences in **Chapter 5**. This study uncovers the strong effect

of transmission steering angles on the velocity estimates but also shows that relatively few transmissions are required to obtain high accuracy estimates.

1.2.4 Objective 4: Devising a VBF Estimator Using a Portable Ultrasound Scanner

To date, VBF has been estimated from 3D ultrasound flow vectors *in vivo* in previous works on large-scale ultrasound scanners (Correia et al., 2016, Holbek et al., 2017a, Correia et al., 2020) but not on any portable systems. Additionally, there has been limited investigation of the robustness of the VBF estimators to changes in flow orientation or position in the imaging frame. Nonetheless, these studies have demonstrated promising performance of VBF estimates from 3D flow vectors. To further advance this research direction, **Chapter 6** presents VBF estimations acquired from a portable ultrasound system and investigates the impact of flow properties (direction and location) on the estimation performance. This study confirmed that precise VBF estimates from a portable ultrasound scanner are possible, albeit with notable offsets from the ground truth depending on the flow orientation and location. With additional work to calibrate the VBF estimates, it is possible that this framework could be applied in clinical studies and eventually in the clinic for free flap monitoring.

1.3 Thesis Outline

The remaining chapters of this thesis are organized as follows:

Chapter 2 presents background information including 2D and 3D ultrasound imaging, ultrasound flow estimation, and high-rate ultrasound imaging. The contents of this chapter are intended to prime readers for the subsequent chapters which describe the thesis research work in detail.

Chapter 3 introduces a novel framework for the estimation of blood flow using chirp-coded excitations to enhance Doppler SNR when using unfocused transmissions. Both the theoretical explanation and in *vitro* experimental validation of the framework are provided.

Chapter 4 details the field profile study performed on a sparse spiral array to assess its suitability for unfocused imaging applications. This chapter focuses on the hydrophone and simulation study results on the array as well as demonstrates the B-mode imaging capabilities.

Chapter 5 presents a study of the effects of transmission sequences on the accuracy of 3D vector flow imaging. The effects are studied on multiple *in vitro* straight tube flow conditions and the optimal transmission scheme is demonstrated on multidirectional and anthropomorphic models.

Chapter 6 showcases VBF estimations from a portable ultrasound scanner using a fully populated matrix array. VBF estimations are performed on several *in vitro* models as well as *in vivo* in a brachial artery.

Chapter 7 summarizes the contributions of this thesis and suggests future research directions that could further extend and advance this work.

Chapter 2
Background

2.1 Ultrasound Imaging for Free Flap Monitoring

Ultrasound is a point of care imaging modality that enables the live viewing of structures within the body while simultaneously providing quantitative measurements such as blood flow velocity (Díaz-Gómez et al., 2021). The imaging capabilities of ultrasound give it a distinct advantage over existing free flap monitoring technologies, such as Doppler pens, which do not provide the user with any visual feedback. A known limitation of flap monitoring with Doppler pens is the risk of the clinician accidentally monitoring the recipient tissue vasculature and not that of the donor tissue (Salgado et al., 2009). Such errors may lead the care team to believe that a flap has normal vascular function even when it is occluded and requires immediate intervention. Currently, to differentiate the donor and recipient vessels, clinicians can compress the flap to temporarily restrict blood flow and ensure that the Doppler signal is also lost (Salgado et al., 2009). However, compressing the freshly transplanted tissue risks damage and is a non-ideal solution. Therefore, there remains a need for imaging-based technologies, such as ultrasound, enabling clinicians to distinguish between donor and recipient vessels more easily.

The following sections describe how ultrasound images and ultrasound flow estimations are performed to prime the readers for the subsequent chapters of this thesis.

2.1.1 Ultrasound Image Formation

Biomedical ultrasound is an imaging modality which uses acoustic waves, commonly in the 1-20MHz range, to construct an image of a region of interest in the human body. The acoustic waves are transmitted and received by ultrasonic transducers which can convert electrical signals into acoustic signals and vice-versa. These waves travel through a medium and are reflected off various scatterers resulting in echoes which return to the transducers and are converted back into electrical signals (referred to as radiofrequency (RF) data). In 2D ultrasound, a linear array of transducer elements is used form a planar image. In 3D ultrasound, a 2D arrangement of transducer elements (commonly referred to as a matrix array or 2D array) is used to form a volumetric image. In both 2D and 3D ultrasound imaging, the design of the transducer array is critical to the imaging properties of the system (Kino & DeSilets, 1979, Macovski, 1979, Turnbull & Foster, 1991). A typical rule of thumb in ultrasound transducer array design is to maintain an element pitch of less than or equal to one half of a

wavelength (λ), that is, the element pitch should satisfy the Nyquist sampling limit. With this element pitch, transmitted and received ultrasound beams are expected to be uniform and free from grating lobes (Macovski, 1979).

To form ultrasound images a pulse-echo sensing paradigm is leveraged. First, an aperture of the array is used to transmit a focused ultrasound beam into the imaging medium [depicted in Figure 2-1(a)]. As the beam permeates the medium it is scattered and reflected by the tissues resulting in echoes returning to the transducer array which can be received by the transducer elements (oftentimes the same aperture in transmit and receive is used, but a different aperture may be used if desired). Note that the elements are not able to simultaneously transmit and receive information and so a short transmission pulse must be used to allow shallow echoes to be recorded. The received echoes are dynamically focused using a process known as delay-and-sum (DAS) beamforming which enables every pixel location to be focused on receive. The reception on a single aperture of the array, from a single transmission event, is used to form a single scanline of the ultrasound image. The location of the scanline is centered below the aperture used in its formation. After receiving is completed, the transmit aperture is stepped laterally by a fixed number of elements and the protocol is repeated. One full image is formed when the transmit-receive aperture traverses the full array at which point it returns to the beginning to continue scanning. Typically, the output image to the scanner display is a log-compressed version of the image known as a brightness map or B-mode image.

While scanline B-mode imaging is the gold standard for ultrasound image quality, it is not without limitations. Scanline imaging requires many pulse-echo cycles to form an image covering the full array aperture which limits the achievable frame rate. The spacing between subsequent transmissions is known as the pulse repetition interval (PRI) and the corresponding inverse is the pulse repetition frequency (PRF). Therefore, the frame rate of a scanline B-mode image is the PRF divided by the number of scanlines being used. While increasing the PRF can increase the imaging frame rate, its increase is limited by the desired imaging depth since the echoes from greater depths require a longer time to reach the array and the array cannot transmit and receive simultaneously. Typical clinical ultrasound scanners operate at a B-mode frame rate around 30Hz. This frame rate is suitable for smooth live imaging; however, it is not sufficient to capture dynamic events within a single cardiac cycle.

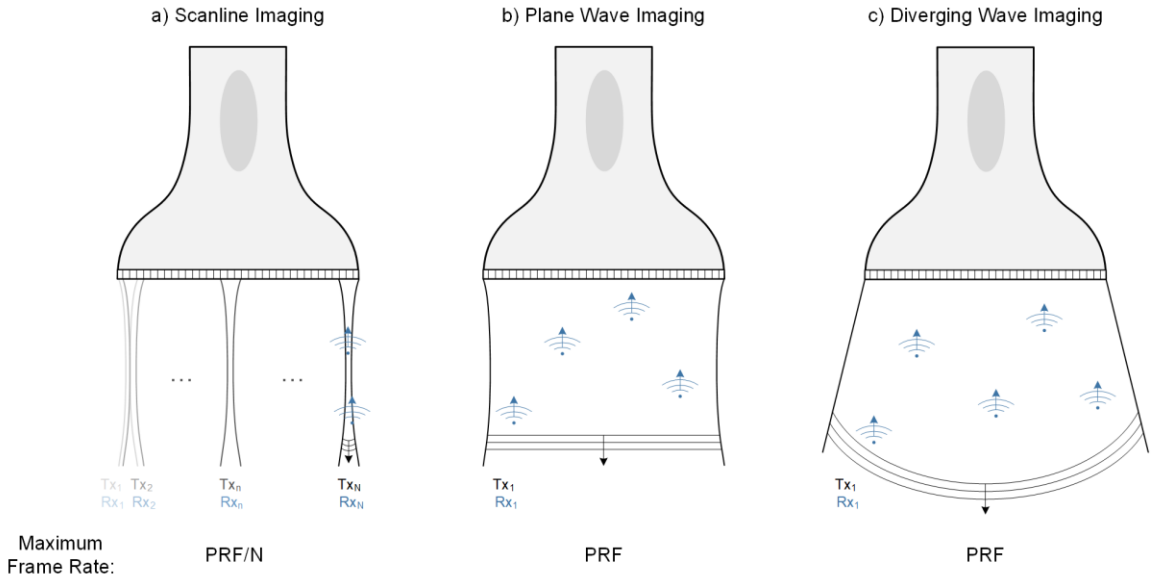


Figure 2-1 Diagram of scanline, plane wave, and diverging wave imaging. (a) Scanline imaging uses focused beam transmissions from a sub-aperture and receives the echoes on the same sub-aperture (typically). The sub-aperture is stepped laterally across the array to form an image resulting in a frame rate of PRF over the number of transmissions. (b) Plane wave imaging emits a broad view pulse with a flat wavefront from all array elements and receives on all elements simultaneously. The frame rate is equal to the transmission rate. (c) Diverging wave imaging is the same as (b) except with a spherical wavefront.

2.1.2 Pulsed Wave Doppler Ultrasound

Pulsed Wave Doppler (PWD) is one means of acquiring blood flow measurements using clinical ultrasound scanners. Like most ultrasound flow measurement techniques, PWD leverages the Doppler effect, that is, the shift in frequency of a wave when it reflects from a moving scatterer. The frequency shift, known as the Doppler frequency, f_d, is related to the frequency of the acoustic wave, f_{RF}, the speed of sound, c, the flow magnitude, v, and the beam-flow angle, σ, through the Doppler equation (2.1).

$$f_d = \frac{2 f_{RF} v \cos\sigma}{c} \tag{2.1}$$

To perform PWD, a region of interest in the B-mode image is selected by the user, known as a range gate [Figure 2-2(a)]. Then, the scanner transmits a series of focused beams centered on the range gate at a high PRF. If there is flow in region identified by the range gate, each consecutive received echo has a slight phase shift [depicted in Figure 2-2(b)] which is directly related to the Doppler frequency [as shown in Figure 2-2(c)]. By performing frequency analysis on the range gate across multiple pulses (i.e. along the slow-time direction), typically via a Fast Fourier Transform (FFT), the Doppler spectral

information is uncovered. As more pulse-echo cycles are performed, the frequency analysis slides in time producing what is known as a Doppler spectrogram. However, for the Doppler spectrum to be converted to a velocity range, the precise beam flow angle, σ, must be known [see equation (2.1)]. In clinical ultrasound scanners, the beam flow angle is typically a user input and therefore is a notable source of velocity estimation error.

The velocities estimated from PWD can be used to estimate the VBF within a blood vessel by extracting either the instantaneous mean velocity, the peak velocity, or the mean velocity over time. For this method to be accurate, it is critical that the range gate be wide enough to cover the entire width of the vessel so that the radial velocity profile is adequately sampled. The instantaneous mean velocity in the vessel can be multiplied by the cross-sectional area of the vessel (estimated from the vessel diameter) to estimate the VBF. The mean velocity over time can be used to estimate the time-averaged VBF in the same way. Alternatively, the instantaneous peak velocity divided by two can be used to approximate the mean velocity, assuming the flow profile is parabolic. Given the pulsatile nature of arterial flow, the assumption of parabolic flow is often inaccurate resulting in further VBF estimation error.

Certainly, PWD has several drawbacks that render it a non-ideal tool for VBF estimation. First, the beam-flow angle and the range gate setting are both user dependent and risk both intra- and inter-operator variability. Additionally, the measurement of the vessel cross-sectional area generally assumes

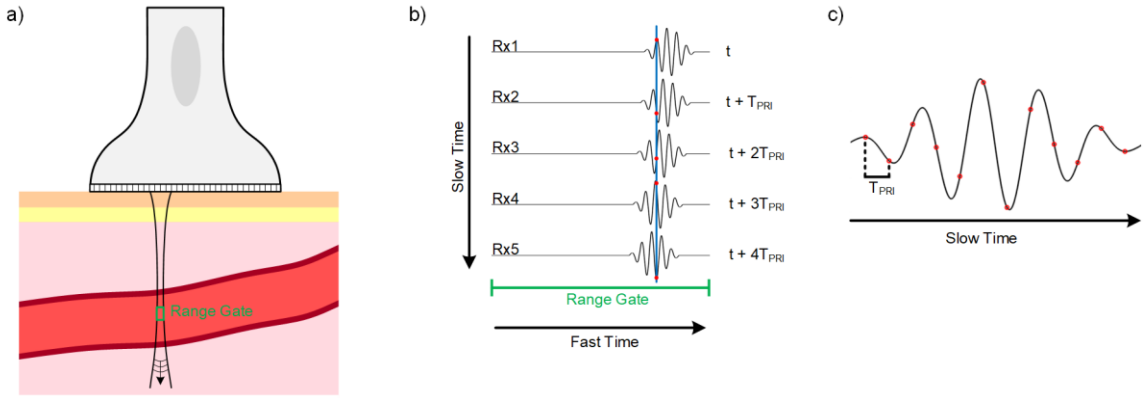


Figure 2-2 Diagram of pulsed Doppler imaging. (a) A range gate for flow estimation is placed within the transmit/receive beam. (b) Received RF data from five transmit-receive on the range gate with an interval of T_{PRI}. Fast-time is along the RF data samples and slow-time is along the transmit-receive repetitions. (c) An extracted set of slow-time data points at a single fast-time location [blue line in (b)]. The frequency of the oscillation along the slow-time direction is equal to the Doppler frequency at that point in fast-time (depth).

a circular cross-section which is often inaccurate. Finally, PWD only provides a single location measurement that limits the user's ability to average over a larger area and potentially reduce estimation errors.

2.1.3 Ultrasound Color Flow Imaging

Color Flow Imaging (CFI) is an alternative mode to produce velocity estimates from a clinical ultrasound scanner. Unlike PWD, CFI estimates velocities across the entire imaging view and not just at a single range gate. This wider view provides a more intuitive representation of the flow to the user, but the frame rate is limited to roughly 20Hz. Overall, the principle behind ultrasound CFI is the same as PWD, except, instead of outputting a Doppler spectrum, CFI computes a mean Doppler frequency at each pixel location and outputs the corresponding mean velocity as a color map overlaying the B-mode image (Merritt, 1987).

The mean Doppler frequency, $\bar{f}_d$, in CFI is estimated from the average phase shift between multiple pulses, $\Delta\psi$, at one pixel location through equation (2.2) (Cobbold, 2007).

$$\Delta\psi = 2\pi T_{PRI}\bar{f}_d \tag{2.2}$$

The phase shift is extracted using a technique known as lag-one autocorrelation (Kasai et al., 1985). Lag-one autocorrelation, as the name suggests, is the calculation of the autocorrelation between the slow-time signal at a particular range gate, S, and the once lagged copy of the same signal. The phase angle of the autocorrelation is the average phase shift from equation (2.2) within the range gate and is given in equation (2.3).

$$\Delta\psi = \angle \sum_{i=1}^{N-1} S^*(i)S(i+1) \tag{2.3}$$

As in PWD, the velocity estimates from CFI must consider the beam-flow angle which remains a user input parameter leading to significant potential for error (Mitchell, 1990). Additionally, the velocity estimation range in CFI is limited by the PRF at each pixel location. According to sampling theory, frequencies in the slow-time direction (Doppler frequencies) can only be resolved to half of the sampling frequency (PRF) before aliasing occurs. While this is also the case in PWD, the use of a spectrogram makes the identification of aliasing easier since the spectrum can be seen wrapping around the frequency axis. In CFI, aliasing results in mis-colored pixels which can be more challenging to distinguish from accurately colored pixels. These limitations of CFI have led to numerous

developments in recent decades to improve both the detectable velocity limits and reduce the operator dependence.

2.2 High-Frame-Rate Ultrasound for Enhanced Flow Estimations

The field of high-frame-rate ultrasound imaging was formed from the need to improve upon the frame rates of scanline ultrasound and CFI such that in vivo dynamics could be visualized. High-frame-rate ultrasound uses novel transmission strategies which can capture fast flow velocities without a dependence on the beam-flow angle. The key concept behind most of the work in this rapidly developing field is that by insonofying a larger area with each transmission, fewer transmissions are required to form each image frame compared to scanline imaging. Therefore, both the b-mode and flow imaging frame rates can be increased dramatically to upwards of 1kHz (Tanter & Fink, 2014).

Unfocused transmissions, such as plane and diverging waves, insonofy the entire imaging window in a single transmission thereby resulting in frame rates as high as the PRF (depicted in Figure 2-1(b) for plane waves and Figure 2-1(c) for diverging waves). However, the downfall of unfocused transmissions is the loss in image quality. The reason for the loss in image quality is twofold: (1) the transmitted signal energy into the imaging region is reduced compared to focused imaging, and (2) the returning echoes cannot easily be localized to a specific image region in DAS beamforming and thus far-away scatterers can make undesired contributions to pixels with overlapping delays. To combat the reduced image quality, methods such as coherent compounding of plane wave images (i.e. pixelwise summation of images formed from different plane waves) have been developed to improve quality while maintaining high frame rates (Montaldo et al., 2009).

Regardless of the loss in signal quality, the development of high-frame-rate ultrasound techniques has incredible value in dynamic ultrasound imaging. Since the development of unfocused imaging, the field of ultrasound flow imaging has flourished with novel techniques that take advantage of newly achievable frame rates (Coture et al., 2012, Ekroll et al., 2013, Yiu & Yu, 2013, Yiu et al., 2014, Lenge et al., 2015, Leow et al., 2015). One of the most prominent developments was the advent of vector flow imaging (VFI) techniques which can produce high-frame-rate flow estimations that are independent of the beam-flow angle. Removing the dependence of beam-flow angle from the velocity estimation eliminates a significant source of estimation uncertainty and operator dependence resulting in a more robust technique. Numerous methods have been developed to derive flow vectors from ultrasound data

(Jensen et al., 2016a, Jensen et al., 2016b), but, for the sake of brevity, only multi-angle Doppler VFI will be discussed here.

2.2.1 Multi-Angle Doppler Ultrasound

Multi-angle Doppler methods are an extension of pulsed Doppler methods, such as CFI, into the high-frame-rate VFI domain. Multi-angle Doppler techniques acquire velocity estimations along two or more different ultrasound beam directions and then use simple geometrical arguments to convert the individual estimations into flow vectors. The use of multiple known flow sampling directions facilitates velocity estimations that are independent of the beam-flow angles, eliminating the need for user input. As derived by Yiu and Yu (2016), the Doppler equation can be written in terms of the transmit and receive steering angles, θ and γ, respectively, and the flow velocity components in the x- and z-directions, v_x and v_z, given in equation (2.4).

$$v_z(\cos\theta + \cos\gamma) + v_x(\sin\theta + \sin\gamma) = \frac{c}{f_{RF}} f_d \tag{2.4}$$

This modified version of the Doppler equation is no longer dependent on the beam-flow angle, σ, but now has two unknown components: v_x and v_z. Therefore, a minimum of two independent realizations of this equation are required to solve for the 2D velocity vectors. These realizations come from Doppler frequency measurements at different transmit and receive angles.

Methods using two sets of transmit-receive angles are known as dual-angle Doppler and have been reviewed by Dunmire et al. (2000) for single range gate flow calculations. By using unfocused transmission schemes dual-angle Doppler is no longer limited to flow estimation in a single range gate but instead could be performed over an entire image simultaneously (Ekroll et al., 2013, Fadnes et al., 2015). However, dual-angle Doppler methods can be subject to high estimation variance without large slow-time ensemble lengths (Ekroll et al., 2013).

Multi-angle Doppler methods leverage more than two sets of transmit-receive beams to reduce the estimation variance (Yiu et al., 2014, Yiu & Yu, 2016). This is done by creating an over-determined system of equations and solving using a least-squares approach (Yiu & Yu, 2016). The system of equations is given in matrix form by equations (2.5) and (2.6).

$$\mathbf{Av} = \mathbf{u} \tag{2.5}$$

$$\begin{bmatrix} \cos\theta_1 + \cos\gamma_1 & \sin\theta_1 + \sin\gamma_1 \\ \vdots & \vdots \\ \cos\theta_M + \cos\gamma_N & \sin\theta_M + \sin\gamma_N \end{bmatrix} \begin{bmatrix} v_z \\ v_x \end{bmatrix} = \begin{bmatrix} u_{11} \\ \vdots \\ u_{MN} \end{bmatrix} \tag{2.6}$$

Where u is equal to the right-hand side of equation (2.4). To compute the least-squares solution to this system of equations, the pseudo-inverse of matrix $\mathbf{A}$ is used as given in equation (2.7).

$$\mathbf{v} = (\mathbf{A}^T\mathbf{A})^{-1}\mathbf{A}^T\mathbf{u} \tag{2.7}$$

Since this method relies on many transmission angles, it is robust to errors present in a single transmission due to unfavorable beam-flow angles or other factors.

2.2.2 Limitations of High-Frame-Rate Ultrasound

While high-frame-rate ultrasound techniques such as multi-angle Doppler have been widely successful in enhancing the dynamic imaging capabilities of ultrasound, they remain restricted to 2D image planes. The 2D flow vectors obtained with these methods are merely projections of the underlying 3D flow profile onto the imaging plane. One study by Hansen et al. (2014) found that VBF measurements from 2D VFI in the kidney had similar error levels compared to VBF measured from CFI in previous works (Huisman et al., 2005, Schwarz et al., 2003). These results indicate that there is a limit to the accuracy of 2D based VBF estimation methods because of the assumptions about the out-of-plane flow and vessel geometry; however, the variance was reduced using 2D VFI from the reduced operator dependence. Additionally, tasks such as vessel segmentation for calculating the cross-sectional area are more challenging in high-frame-rate ultrasound compared to scanline ultrasound because of the reduction in image quality. For ultrasound to reliably measure VBF with minimal assumptions and user input, it must be extended into 3D and leverage the recent advances in high-frame-rate 2D ultrasound.

2.3 High-Volume-Rate Ultrasound: The Next Generation of Ultrasound Flow Estimation

3D ultrasound technology enables the more intuitive capture of complex structures and dynamics *in vivo* than 2D ultrasound. 3D ultrasound has the potential to acquire complete 3D flow profiles even in traditionally difficult imaging scenarios such as bifurcations, aneurysms, and other tortuous vessels. Furthermore, capturing the complete 3D flow profile enables the derivation of VBF without any assumptions on the flow profile or vessel geometry. Indeed, 3D ultrasound could revolutionize the post-operative monitoring of free flaps providing clinicians with a reliable, objective metric on the vascular

health of the transplanted tissue. Yet, despite its promise, 3D ultrasound remains far from widespread clinical use.

Typically, 3D imaging is performed by leveraging 2D matrix transducer arrays to capture volumetric data. In modern clinical scanners with 3D imaging capabilities, these matrix arrays are operated in a similar manner to 2D scanline ultrasound except with thousands of transducer elements instead of hundreds. Given that the focused beams must now be stepped over a planar surface, the time required to capture a single volumetric image far exceeds that of 2D scanline imaging. For this reason, high-end clinical 3D ultrasound scanners are typically limited to volume rates <10Hz rendering full-volume, dynamic flow imaging impossible. The use of broad view transmissions can increase the volume rates to the PRF limit; however, this requires the simultaneous acquisition of data on the 1000+ elements of a matrix array which can reach upwards of 50GB/s. Currently, there are only a select few ultrasound scanners globally that can process data at such high rates (Jensen et al., 2013, Petrusca et al., 2018). Recent works on these systems have demonstrated their capability for high-volume rate imaging *in vivo* (Correia et al., 2016, Santos et al., 2016, Provost et al., 2014). Unfortunately, these powerful systems are large and do not preserve the portable, point-of-care reputation of ultrasound rendering them unusable in ICUs for free flap monitoring. This has led to extensive research on 3D ultrasound channel count reduction strategies which aim to minimize the loss in image quality while significantly reducing the data load.

The most prominent channel count reduction strategies fall under two broad categories: 1) novel array designs with low channel counts, and 2) traditional matrix arrays with reduced receive channels. The following subsections will provide an overview of two solutions from each of these categories.

2.3.1 Novel Array Designs

2.3.1.1 Sparse Arrays

Sparse arrays are perhaps the simplest method to reduce the channel count from 2D matrix arrays for 3D ultrasound imaging systems. Sparse array designs remove certain elements from 2D matrix arrays to reduce the channel count. This removal of elements in 2D sparse arrays generally leads to a greater than $\lambda/2$ spacing between the elements which can result in sidelobes and grating lobes in the transmit and receive beams (von Ramm & Smith, 1990). Thus, sparse arrays must be carefully designed to optimize beam quality.

Advanced sparse array design methodologies such as simulated annealing can optimize the arrays with many degrees of freedom including element counts, location, and weighting to produce arrays with good field properties (Trucco, 1999, Roux et al., 2016). Additionally, with the development of capacitive micromachined ultrasound transducer (CMUT) arrays, the design flexibility of sparse arrays has increased opening the door for more complex layouts such as spirals and with fewer restrictions on element shape and size (Martínez-Graullera et al., 2010, Diarra et al., 2013, Ramalli et al., 2015).

Recently, a few studies have applied sparse arrays in imaging (Roux et al., 2018), Doppler (Mattesini et al., 2020, Rossi et al., 2020), and even super resolution experiments (Harput et al., 2020). These results have shown comparable resolution performance between 1024-element 2D matrix arrays and sparse arrays with 256-elements with a reduction in contrast for the sparse array in focused and unfocused mode imaging (Roux et al., 2018). They have also shown comparable Doppler performance with unfocused transmissions (Rossi et al., 2020). These studies have reached a maximum volume rate of 500Hz (Harput et al., 2020) which is lower than typical 2D VFI which is often performed at >1kHz. This reduced volume-rate is a result of the significant image compounding required to maintain a suitable signal-to-noise ratio (SNR) with sparse arrays. In general, the SNR loss is the most notable limitation of using 2D sparse arrays for 3D high-volume-rate imaging.

2.3.1.2 Row-Column Addressed Arrays

RCA arrays provide a means to reduce the channel count of a 2D matrix array, without sacrificing the signal strength (Morton & Lockwood, 2003). These arrays use a full 2D matrix of elements which can only be addressed row- or column-wise and not element-wise. By removing the individual addressing of the elements, the channel count for an N-by-N array is reduced from N^2 to just 2N. However, beam-steering and focusing can only be performed along one axis in transmit and on the orthogonal axis in receive since only the rows or the columns can be addressed at any given time thus limiting the angle combinations available for methods such as multi-angle Doppler. In addition, a key consideration in the application of RCA arrays to high-volume-rate applications is that the orthogonal transmit-receive (e.g. column-row) pair must be flipped (e.g. row-column) in order to achieve an isotropic point spread function and thus image quality (Sauvage et al., 2018). This double transmission requirement effectively halves the PRF of any imaging mode resulting in a reduced velocity estimation range.

2.3.2 Reduced Receive Systems

2.3.2.1 Array Multiplexing

Multiplexing reduces the data transfer between a matrix array and the scanner by switching between sub-apertures of elements on the array (Risser et al., 2016). This technique enables a lower-channel count scanner to drive a 2D matrix array. For example, a 1024-element 2D matrix array with a 4:1 multiplexing circuit can be connected to a 256-channel scanner. The multiplexing circuits themselves can be ASICs in the probe head, directly integrated with the array chip in CMUT arrays, or be performed on the ultrasound scanner with larger electronics. The downside of multiplexing is that it divides the achievable frame rate by at least the number of multiplexing channels.

2.3.2.2 Micro-Beamforming

Micro-beamforming is a technique which divides a 2D matrix array into several sub-apertures and beamforms those apertures directly in the probe head on application specific integrated circuits (ASICs) (Savord, 2000). This means that RF channel domain data does not need to be transferred from each individual array element to the scanner. Instead, partially beamformed data with a reduced channel count according to the number of sub-apertures is transferred. This technique has been commercially adopted (for example by Frey & Chiao, 2008) and has been used to implement array designs with thousands of elements. However, micro-beamforming restricts the possible imaging modes on the probe by having fixed delay settings in the ASICs and is therefore a non-ideal candidate for researching novel high-volume-rate imaging modes. That said, one study has demonstrated volume rates up to 610 volumes/s using micro-beamforming coupled with diverging wave transmissions (Santos et al., 2016).

2.3.3 Limitations of High-Volume-Rate Ultrasound

The most apparent limitations of high-volume-rate 3D ultrasound are the achievable data transfer rate and processing rate of modern systems and the reduction in signal quality compared to 2D ultrasound techniques. With constant advancements in computing technology, such as GPUs, it is likely that data transfer and processing limitations will continuously improve over time from research outside of the ultrasound domain. However, improvements to 3D ultrasound signal quality are a less straightforward issue. Unfocused transmissions in 3D ultrasound imaging are hindered by their complete defocusing on the plane parallel to the array. In contrast, linear ultrasound arrays for 2D imaging generally employ acoustic lenses to provide focusing onto the imaging plane (i.e. in one lateral direction). The lack of

focusing combined with channel count reduction methods, such as sparse arrays, leads to severely reduced SNR which may jeopardize the ability to use unfocused transmission schemes for high-rate imaging in 3D *in vivo*. Alternative methods such as multiplexing, micro-beamforming, and RCA arrays tend to have higher SNR than sparse arrays, however, these methods each suffer from frame rate reductions or programming flexibility that limit their usability in novel high-volume-rate imaging developments.

Chapter 3
Chirp-Based Velocity Estimation (ChiVE): A Framework for Enhanced Flow Imaging with Wideband Transmissions

3.1 Introduction

Recent advances in Doppler ultrasound imaging have facilitated the quantification and visualization of highly dynamic flows through a transition from traditional low-frame-rate focused beam techniques to novel high-frame-rate ultrasound (HiFRUS) techniques with unfocused broad view transmissions (Goddi et al., 2018). Broad view transmissions have enabled the realization of numerous vector flow imaging frameworks (Jensen et al., 2016a, Jensen et al., 2016b). Yet, HiFRUS encounters performance limitations from broad view imaging though the inherent signal-to-noise ratio (SNR) reduction. While methods have been proposed to enhance B-mode SNR (Montaldo et al., 2009), to date no specialized methods have been developed to enhance the SNR of broad view Doppler ultrasound without sacrificing the frame rate. In addition to the SNR reduction, HiFRUS also has a performance trade-off related to the bandwidth of the transmitted pulse; low variance Doppler velocity estimations can only be achieved with narrow-bandwidth transmissions, whereas B-mode resolution is enhanced with wide-bandwidth transmissions. The bandwidth trade-off implies that neither mode can be optimized with a single transmission and has forced most recent works to utilize interleaved Doppler and B-mode specific transmissions to improve performance at the cost of frame rate. These frame rate reductions lead to proportional reductions in the velocity estimation limits, inhibiting the accurate estimation of high-velocity flows. Given the low SNR and the bandwidth trade-off, high-frame-rate Doppler ultrasound would benefit from a specially designed signal enhancement framework, in particular one that does not limit the achievable frame rate.

Coded transmissions are a candidate for broad view signal strength enhancement for both Doppler and B-mode imaging. Coded transmissions can be pulse compressed upon reception to yield sharp high intensity signals. Some codes, such as Golay codes and Barker codes, however, are not well suited to Doppler processing due to their intolerance to phase shifts during compression (Misardis & Jensen, 2005a) and their requirement for paired transmissions which halves the achievable frame rate. Chirped signals, in contrast, can be used as excitation codes that are robust to phase shifts and do not require paired transmissions. Additionally, chirps have recently been demonstrated in spectral Doppler

(Ramalli et al., 2021) as well as previously in B-mode imaging (Pederson et al., 2003, Chiao & Hao, 2005, Misaridi & Jensen, 2005b, Misaridi & Jensen, 2005c, Oelze, 2007).

The barrier to using chirps in Doppler ultrasound stems directly from their wideband nature which makes them incompatible with traditional processing techniques. Most commonly, Doppler ultrasound uses a narrowband pulse to produce a corresponding narrowband Doppler frequency spectrum, thus yielding a low-variance estimation of the flow velocity. While wideband chirps have been used in spectral Doppler to increase SNR (Ramalli et al., 2021), a corresponding wideband Doppler spectrum was observed which will inevitably increase the variance of the resulting velocity estimates. To reduce the velocity estimation variance stemming from wideband Doppler spectra, filter-banks can be used to parse the spectra into sub-bands (Gran et al., 2008). But sub-band processing does not utilize the continuous Doppler spectrum available and potentially loses information. A specialized pipeline to process chirped signals for Doppler velocity estimation could leverage the entire wideband spectrum to yield a more robust velocity estimation while simultaneously increasing both the Doppler and B-mode signal strength.

In this work, we present the first specialized Doppler velocity estimation technique for chirp-coded signals. Our technique, hereafter referred to as chirp-based velocity estimation (ChiVE), is intended to yield twofold benefits: 1) to enhance the Doppler signal strength, which is especially needed when performing high-frame-rate imaging with broad view transmissions, and 2) to overcome the bandwidth-related performance trade-off when utilizing a single transmission for Doppler and B-mode imaging. The guiding proposition behind ChiVE's algorithmic design is that chirped acquisitions can be used to estimate flow velocities by leveraging the linearity of frequencies (Doppler and RF) in the Doppler equation. The frequency linearity, quantified through linear regression over a 2D frequency space, can be exploited to achieve extended-range velocity estimation. The ChiVE framework presented in this work was tested on in vitro flow scenarios, including steady straight tube flows and pulsatile flows in a bifurcation, and assessed for Doppler SNR enhancements and velocity estimation performance. The ChiVE technique provides a novel approach to Doppler ultrasound that enables reliable, low-variance velocity estimations in reduced signal scenarios while facilitating uncompromised Doppler and B-mode performance.

3.2 ChiVE Framework

The ChiVE framework is a frequency-domain method of velocity estimation in Doppler ultrasound which leverages the wideband nature of chirps for robust velocity estimation. The framework is based in the linearity of the Doppler frequency, f_d, and the transmission frequency, f_{RF}, in the Doppler equation (equation (2.1)). For a chirp transmission, f_{RF} is a spectrum instead of a singular frequency value and, in turn, f_d will also be a spectrum. Therefore, the goal of the ChiVE framework is to analyze the trend relating the two spectra to evaluate v. Evaluating the trend in frequencies, rather than individual frequency components, allows the framework to identify aliasing phenomena and output aliasing resistant velocity estimations. This analysis requires a novel processing pipeline to extract and processing the frequency spectra.

To achieve robust velocity estimations, the framework is divided into three fundamental modules (Figure 3-1):

1) pre-processing steps including pulse compression, beamforming, and clutter filtering followed by the frequency domain conversion of image range gates to extract the Doppler frequency and RF components;

2) mean velocity estimation and aliasing detection from the frequency domain data to obtain a coarse estimate of the velocity at a range gate;

3) modal velocity estimation via the radon transform of the frequency domain data to refine the velocity estimate and suppress the effects of velocity averaging.

These three modules are an alternative to the traditional CFI processing pipeline based on lag-one autocorrelation.

The first module forms the ultrasound images, performs clutter filtering, and extracts the image range gates. The range gates are formed into arrays and converted to the frequency domain such that an analysis of the ultrasound and Doppler frequency spectra can be performed. From these spectra, the second module fits the mean Doppler frequencies to a linear trend with the RF frequencies. The linear fitting used in this module accounts for potential aliasing in the Doppler frequency axis and enables the framework to detect aliasing and correct for it before the final velocity estimation. Finally, the slope of the linear fit from the second module is used in the third module as an initial guess at the velocity estimate as well as to unwrap the frequency array as needed. The third module takes a projection

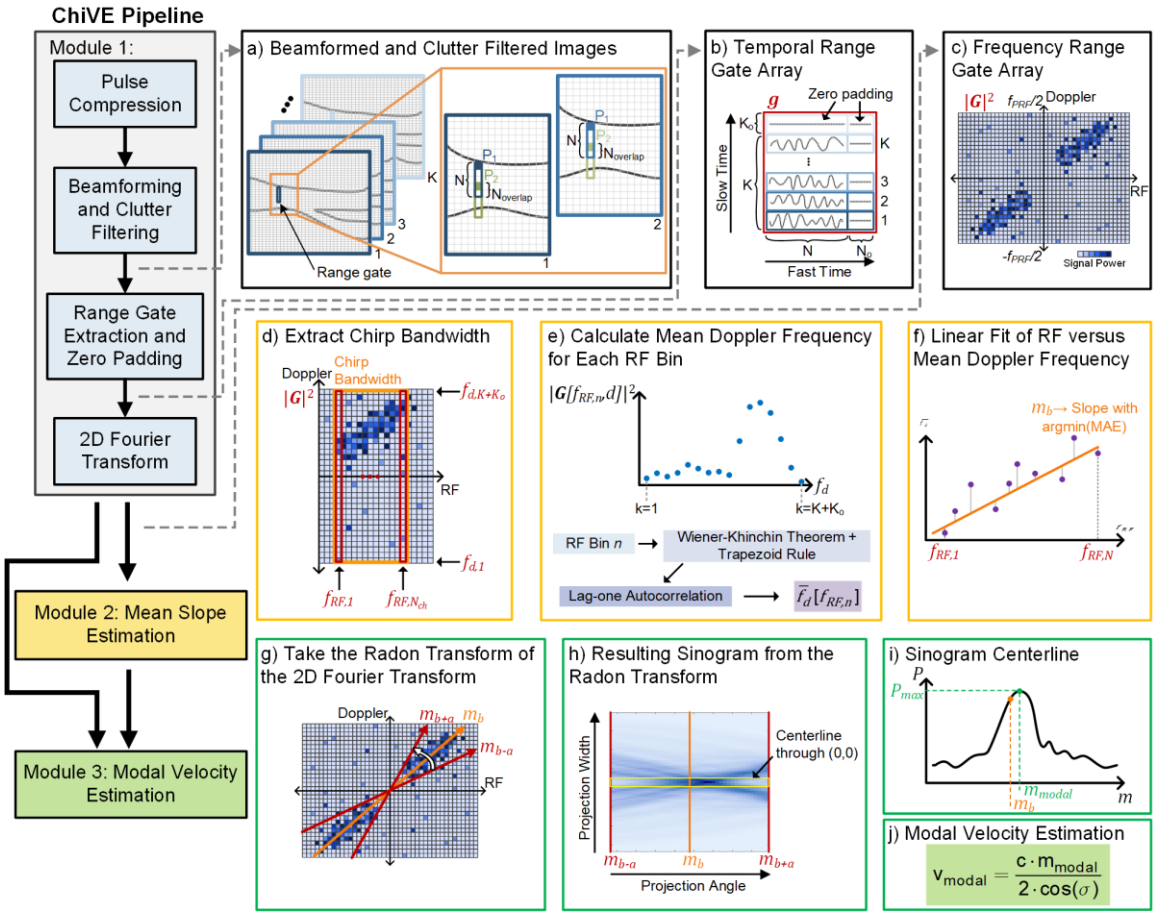


Figure 3-1 Schematic of the ChiVE framework. Module 1 – pre-processing, range gate extraction, and frequency domain conversion; module 2 – mean slope estimation, and module 3 – modal velocity estimation. Details of the modules are presented in the sub-panels. Module 1: (a) post-beamforming and clutter filtering, the range gates with N pixels are extracted from each frame (for K frames). P_1 corresponds to the current flow processing pixel and P_2 is the subsequent flow processing pixel; (b) the range gates for P_1 are assembled into a temporal array with fast-time and slow-time components. The array can be zero-padded in the fast-time direction with N_o pixels and the slow-time direction with K_o pixels; (c) the 2D Fourier transform converts the temporal range gate array into a frequency range gate array with RF and Doppler frequency components. Module 2: (d) the frequency range gate array from which the chirp bandwidth is used; (e) for each RF band within the chirp bandwidth, use the Wiener-Khinchin theorem and lag-one autocorrelation to calculate the mean Doppler frequency; (f) the mean Doppler frequencies for each RF bin are linearly fitted and the value of the slope, m_b, is outputted. Module 3: (g) a radon transform is performed on the frequency range gate array over a range surrounding the mean slope estimate, m_b; (h) The resulting sinogram from the radon transform where the centerline can be extracted for analysis. The centerline is the portion of the projection that passes through the origin of the frequency range gate array; (i) The centerline of the sinogram will have a peak corresponding to the modal slope, m_{modal}; (j) the modal slope can be converted to a modal velocity estimate via the Doppler equation.

through the frequency matrix and determines the highest power slope from the projection. The highest power slope is equivalent to the modal velocity estimate.

3.2.1 RF-Doppler Frequency Domain Conversion

The first module of the ChiVE framework (see Figure 3-1) performs all pre-processing steps in the pipeline prior to the initial coarse velocity estimate. This begins with matched filtering of the raw RF data to compress the chirp pulses. Then, the compressed signals are beamformed into a series of image frames which are subsequently clutter filtered on the slow-time direction. It is important to note that since ChiVE is a frequency domain framework, the axial sampling rate after beamforming must be at least twice the wavenumber of the maximum chirp frequency used in transmission to satisfy the Nyquist criterion. Additionally, analytic signal conversion is omitted from the framework to preserve both positive and negative frequency components of the RF spectrum. Otherwise, the requirements for beamforming and clutter filtering for the ChiVE framework are identical to that of a typical lag-one autocorrelation-based CFI framework.

The resulting images are divided into range gates containing N fast-time pixels each [Figure 3-1(a)]. The range gate is extracted from a slow-time ensemble of K frames at the same spatial location. The range gate is configured into a 2D N-by-K temporal array denoted as $\mathbf{g}$ [Figure 3-1(b)]. The temporal array, $\mathbf{g}$, can be zero-padded in both the fast-time and slow-time directions by N_o pixels and K_o frames. Then, the 2D Fourier transform of $\boldsymbol{g}$ is taken to produce the 2D frequency range gate array, $\boldsymbol{G}$, where one direction corresponds to the Doppler frequency, f_d, and the other to the RF, f_{RF}. By taking the squared magnitude of $\boldsymbol{G}$, the power of each individual RF-Doppler frequency pair is obtained. The array $|\boldsymbol{G}|^2$ [Figure 3-1(c)] is expected to contain a linear trend amongst the highest power components within the RF frequencies transmitted in the chirp, according to the Doppler equation. Each frequency range gate array is used to compute the value of a single flow pixel in the final flow map.

When the algorithm steps to the subsequent range gate location for processing, $N_{overlap}$ pixels axially are shared with the previous range gate. At the bottom of an image column, the algorithm steps to the subsequent column and no pixels are shared with the previous range gate.

3.2.2 Mean Slope Estimation and Aliasing Detection

The second module of the ChiVE framework performs a coarse estimation of the slope between the RF and Doppler frequencies as well as determines the number of aliasing cycles present on the Doppler

axis. This process starts by computing the mean Doppler frequency at each RF bin in the 2D Fourier transform (module 2 in Figure 3-1). First, the RF bins corresponding to the transmitted chirp are identified in the matrix $|\boldsymbol{G}|^2$ [Figure 3-1(d)]. Then, for each RF bin in the chirp, the power spectral density is calculated. Using the power spectral density, lag-one autocorrelation can be performed in the frequency domain by leveraging the Wiener-Khinchin theorem and the trapezoid rule for numerical integration [Figure 3-1(e)]. The angle of the lag-one autocorrelation output is an estimate of the mean Doppler frequency for a given RF bin. Thus, this process generates a set of RF-mean Doppler frequency pairs which, according to the Doppler equation, should follow a linear trend passing through the origin. The slope of this trend is directly proportional to the underlying flow velocity.

However, in cases where some of the Doppler frequencies have aliased (i.e. surpassed the Nyquist limit of $|f_{PRF}/2|$) the linear trend will wrap around the Doppler axis resulting in a discontinuity in the trend. To fit the linear trend while accounting for aliasing-based discontinuities, ideal RF-Doppler frequency datasets can be generated for a range of possible velocities. The ideal datasets, computed from the Doppler equation, cover the RF spectrum of the chirp bandwidth and give the corresponding Doppler frequency value according to the velocity being tested. Doppler frequencies within the ideal datasets that exceed the aliasing limit are wrapped around the Doppler frequency axis such that they match the experimental data in $|\boldsymbol{G}|^2$. For every test velocity, the ideal Doppler frequency values are compared to the mean Doppler frequencies computed from $|\boldsymbol{G}|^2$ for every RF bin in the chirp. A mean absolute error (MAE) value is computed for each test velocity. The test velocity value that yields the minimum MAE is the best fit to the experimental data [Figure 3-1(f)]. The MAE is used here instead of root mean squared error (RMSE) to prevent outlying datapoints from skewing the slope estimate. Since the number of Doppler frequency axis unwraps is known for all test velocities, the number of aliasing cycles for the best fitting velocity is also determined.

While at this point in the framework the slope could be converted to a velocity estimate, mean Doppler frequency estimators are known to suffer from underestimation of the true peak velocity. Thus, the framework can improve upon the slope estimate using the third framework module which is a modal velocity estimator.

3.2.3 Modal Velocity Estimation

Modal velocity estimation is performed via the discrete radon transform of $|\boldsymbol{G}|^2$ [Figure 3-1(g)]. Prior to performing the radon transform, $|\boldsymbol{G}|^2$ is unwrapped according to the number of aliasing cycles found

Table 3-1 Transmission parameters

	CH2	CH4	CH6	ST5
Pulse Type	Linear up-chirp			Sinusoid
Center Frequency	5MHz			
Pressure at Center Frequency	286.4kPa (100V bias) 166.3kPa (60V bias)			
Duration	5μs			1μs (5 pulse cycles)
Programmed Bandwidth	2MHz	4MHz	6MHz	N/A
Real Bandwidth (-6dB)	1.66MHz	3.60MHz	5.46MHz	1.28MHz
Window	10% Tukey			Hamming
PRF	2kHz			

Table 3-2 Pre-beamforming bandpass filter parameters

	CH2	CH4	CH6	ST5
Transmission band -6dB limits (MHz)	4.17 – 5.83	3.2 – 6.8	2.27 – 7.73	4.36 – 5.64
Passband limits (MHz)	3.5 – 6.5	2.5 – 7.5	1.5 – 8.5	4 – 6
Filter Order	150			

in the mean slope estimation module. The radon transform is a projection through $|\boldsymbol{G}|^2$ over a range of angles (or slopes) which, in this case, are defined based on the mean slope estimate from the previous module of the framework. For each angle in the radon transform, the data in $|\boldsymbol{G}|^2$ is summed along the direction defined by the angle into a vector. Subsequent angle projections are stacked side-by-side to for a radon transform matrix. The radon transform matrix is known as a sinogram. In Figure 3-1(g), the mean slope estimate is shown as the orange line and the maximum and minimum projection slopes are shown as the red lines marked m_{b+a} and m_{b-a}, respectively. When the radon transform is performed, the sinogram in Figure 3-1(h) is produced. Here, the slopes m_{b-a} and m_{b+a} are on the right and left edges of the sinogram respectively and the mean slope estimate, m_b, is the vertical line in the center marked in orange. Since the frequency relationship in the Doppler equation passes through the origin of the

frequency range gate array, only the center portion of each projection angle needs to be analyzed [see yellow box in Figure 3-1(h)]. The centerline (or alternatively an average of the centerline and surrounding lines can be used) is plotted in Figure 3-1(i). The peak of the centerline corresponds to the projection slope that had the highest total power through the origin and is thus the modal slope. This slope can be used in the Doppler equation to produce a modal velocity estimate [Figure 3-1(j)].

3.3 Imaging Methods

The acquisitions for the ChiVE framework have been realized using the ULA-OP 256 research ultrasound scanner (Boni et al., 2016) and a prototype 256-element linear capacitive micromachined ultrasound transducer (CMUT) array. The ULA-OP 256 system allows for arbitrary waveform generation and is thus suitable for the transmission of chirped waves. The wide bandwidth of the CMUT array enables the accurate conversion of the programmed chirp waveforms into acoustic transmissions. The array was biased with 100V in all imaging experiments unless otherwise noted. A working voltage of $20V_{peak\text{-}peak}$ was used in all experiments. The ULA-OP 256 system was set to a sampling rate of 39.06MHz. Upon reception, all RF data was transferred to storage for offline processing.

3.3.1 Transmission Parameters

In this study, the ChiVE framework was tested with three unique chirp transmissions and compared to a CFI framework with a standard transmission. All chirp transmissions were 5μs in length and swept linearly from low- to high-frequency with a center frequency of 5MHz. Chirp bandwidths of 2, 4, and 6MHz were tested (note that these are the ideal programmed bandwidths, not the true -6dB bandwidths after windowing). To simplify the descriptions in this work, the chirp pulses are given the shortforms CH2, CH4, and CH6, respectively. The standard transmission for the CFI framework was centered at 5MHz with a length of 5-pulse cycles. The standard pulse is given the shortform ST5 from here forward. A pulse repetition frequency (PRF) of 2kHz was used in all studies. A complete summary of the transmission parameters can be found in Table 3-1. Here, it is shown that the bandwidths of the chirped and standard pulses do not match. The standard pulse was intentionally left unmatched to the bandwidths of the chirped transmissions such that it would better reflect a commonly used transmission

Table 3-3 Beamforming resolution

	CH2	CH4	CH6	ST5
Lateral resolution (µm)	100			
Axial resolution (µm)	58.33	50	43.75	100

in a typical CFI framework and thus provide a reasonable baseline to compare the ChiVE framework to commonly used flow imaging schemes.

3.3.2 Pre-Filtering, Pulse Compression, Beamforming, and Clutter Filtering

After the data were transferred and saved for offline processing, all subsequent steps were performed in Matlab (MathWorks, Natick, MA, USA), including filtering, pulse compression, beamforming, and velocity estimations. First, the channel-domain RF data was filtered using an FIR bandpass filter to remove frequency components outside of the expected frequency bands (the specific filter parameters varied depending on the transmission and are listed in Table 3-2). At this point, the standard transmissions to be used in the CFI framework are ready to be beamformed, however, the chirped transmissions for the ChiVE framework must undergo pulse compression first. Pulse compression of the chirped transmissions is executed in this study via matched filtering. The matched filter kernels were generated from hydrophone measurements (HGL-400, ONDA Corporation, Sunnyvale, CA, USA) of the chirp pulses.

The received signals for both frameworks were beamformed with a previously described GPU-based delay-and-sum beamformer (Yiu et al., 2011). The F-number was set to 1 in all cases. The lateral beamforming resolution was fixed for all scenarios in this study while the axial beamforming resolution was varied for the images to be used in the ChiVE framework. The axial sampling rate (post-beamforming) in the ChiVE framework was increased linearly with the chirp bandwidth to prevent aliasing in the RF (fast-time) axis which would be detrimental to the performance of the framework. The maximum axial sample spacing to satisfy the Nyquist criterion is half the wavenumber of the maximum transmission frequency and thus the axial sample spacing in beamforming was set to be 10% shorter than this limit in each case. Details of the beamforming parameters for both the CFI and ChiVE frameworks are found in Table 3-3.

The post-beamformed image frames were then passed through an FIR high-pass filter for clutter filtering (order: 365, cutoff: 20Hz). The parameters of the clutter filter were kept constant between all transmissions for both frameworks. With the tissue signals suppressed from clutter filtering, the flow regions were segmented via thresholding of the Doppler power signal. This segmentation method provided satisfactory results for simple flow scenarios (constant flows) while more challenging scenarios (pulsatile flows) were cleaned up via manual segmentation.

3.4 Experimental Methods

To evaluate the performance of the ChiVE framework and comprehensively compare it to a typical CFI framework a series of experiments were performed. First, Doppler SNR and flow estimation performance was assessed in constant flow conditions in a straight tube phantom. Then, the impact of the Doppler SNR changes between ChiVE and the typical CFI framework were investigated by reducing the transmission pressure to simulate a reduced SNR scenario. Finally, performance in a more clinically relevant scenario was studied via a complex anthropomorphic flow model.

3.4.1 Straight Tube Phantom Studies

To evaluate the accuracy of the ChiVE framework compared to a typical CFI framework, *in vitro* straight tube flow experiments were performed with constant flows. The flow phantom used in these experiments was a wall-less poly-vinyl alcohol (PVA) based vessel fabricated in-house using previously described protocols (Yiu & Yu, 2013). In brief, the PVA mixture for this phantom was composed of 10% PVA (341584; Sigma-Aldrich, St Louis, MO, USA), 3% graphite (282863; Sigma-Aldrich), 0.3% potassium sorbate (85520; Sigma-Aldrich), and 86.7% degassed water. The mixture was cast in a box mold around a 6mm diameter rod. After 3 freeze-thaw cycles of the phantom, the tissue mimic was removed from the box and the rod was extracted to yield a 6mm diameter vessel. After fabrication, the phantom was connected to the flow circuit shown in Figure 3-2 (a). This circuit had the phantom inlet connected to a straight pipe (length: 1m, inner diameter: 6mm) which ensured that fully developed laminar flow was entering into the phantom. The inlet pipe was connected to a programmable flow pump (Ho et al., 2017) through vinyl tubing and flow connectors which was in turn connected to the fluid reservoir. The outlet end of the phantom was connected back to the fluid reservoir to complete the flow circuit. The flow fluid in this study was orgasol-based blood mimicking fluid (Ramnarine et al., 1998) which was fabricated via previously described procedures (Ho et al., 2017).

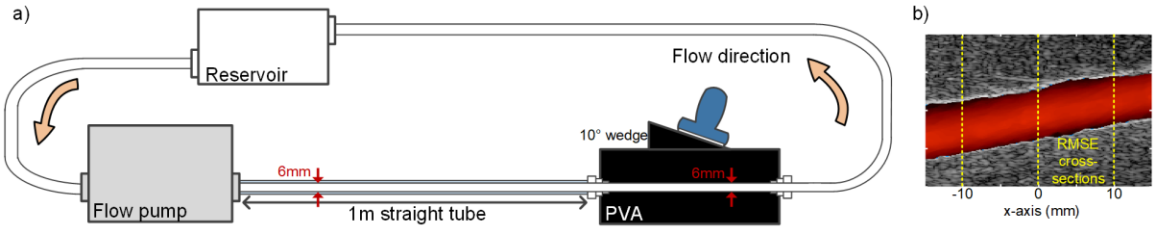


Figure 3-2 (a) Schematic of the straight tube flow experiment setup. (b) Diagram of a straight tube acquisition highlighting the locations of the cross-sections on which the RMSE was evaluated

All experiments in this work on the straight tube phantom setup described above were performed with constant flow rates. Since the flow in the phantom is laminar, the flow profile was assumed to be parabolic. Even so, since there is potential deviation between the pump output flow and the programmed values, the peak flow velocity was measured experimentally as well as calculated analytically. The peak flow measurements were performed using the mean spectrogram trace from a clinical ultrasound scanner (SonixTouch; Analogic Ultrasound) over several seconds. To acquire peak flow measurements with minimal angle dependence, a beam-flow angle of 60° was used (10° transmit steering + 20° probe-vessel angle). The 60° beam-flow angle was chosen to limit the impact of the angle on the conversion between measured Doppler frequency and velocity estimation.

3.4.1.1 Doppler SNR Measurements

The Doppler SNR was evaluated from the Doppler spectrogram over 2000 frames at a range gate in the center of the straight tube vessel with a 5mL/s flow rate. The spectrogram was segmented to yield distinct noise and signal regions along the Doppler frequency axis. The signal region was defined from the -6dB bandwidth of the transmitted signal (see Table 3-2 for the RF band limits) which were then converted to Doppler frequencies. The conversion from transmission to Doppler frequencies used the Doppler equation with the measured peak velocity. The noise region was defined as a fixed region for all transmissions and ranged from the normalized frequencies of 0.6 to 0.8 (normalized by the PRF). The signals in the noise and signal bands were integrated at each time point in the spectrogram. The noise signal was then normalized by the bandwidth it was measured over and then multiplied by the total Doppler bandwidth to yield the total noise energy in the spectrogram. The total signal and noise energies were then averaged over time and the ratio of mean signal energy over mean noise energy was taken to obtain the Doppler SNR.

3.4.1.2 Constant Flow Estimation

The ChiVE framework was tested on a range of constant flow rates in the straight tube phantom and compared to the CFI framework. The range gate length was set to 19-pixels for ChiVE with 20-pixel zero-padding. The ensemble length was set to 59-frames for both the ChiVE and CFI frameworks with no zero-padding added for the ChiVE framework. The flow rates examined in this experiment were 3, 5, 7, 9, 11, and 13mL/s. Considering the transmission center frequency, PRF, and beam-flow angle, it is expected that the flow rates of 11 and 13mL/s will contain aliased flow estimations. In addition to the standard ChiVE framework, a simplified framework will also be studied where the modal velocity estimation is omitted [i.e. the mean slope estimate is converted to a velocity estimate and the steps in Figure 3-1(g-j) are not performed]. The addition of the simplified framework is intended to assess the value in adding the modal velocity estimation steps.

The RMSE of the measured flow profiles will be evaluated based on the ideal parabolic profile calculated from the experimentally measured peak velocity at each flow rate. The RMSE was calculated on three cross-sections of the vessel [cross-sections indicated in Figure 3-2(b)] over 48-frames. The RMSE values of the ChiVE and CFI frameworks will be compared directly to assess the framework performance at each cross-section. A Kolmogorov-Smirnov test will be run to assess the normality of the RMSE data for the three standard ChiVE framework test cases, the three simplified ChiVE framework test cases (without modal velocity estimation), and the lag-one autocorrelation test case prior to significance testing. If the data in any of the test cases is found to be non-normal, then all the data will be log transformed. Levene's test will be used to assess the homogeneity of variance of the RMSE data between the different test cases. If Levene's test indicates the variances are homogeneous then an ANOVA will be run to test for a significant main effect between the RMSE data of each of the test cases. If a significant main effect is found, then a corrected t-test will be used where the correction factor will be equal to the number of tests run (similar to a Bonferroni correction). If Levene's test indicates that the variances are inhomogeneous, then Welch's ANOVA will be used instead. If a significant main effect is found with Welch's ANOVA, then a corrected Welch's t-test will be used where the correction factor is the same as above. The significance level for all testing will be set at α=0.01.

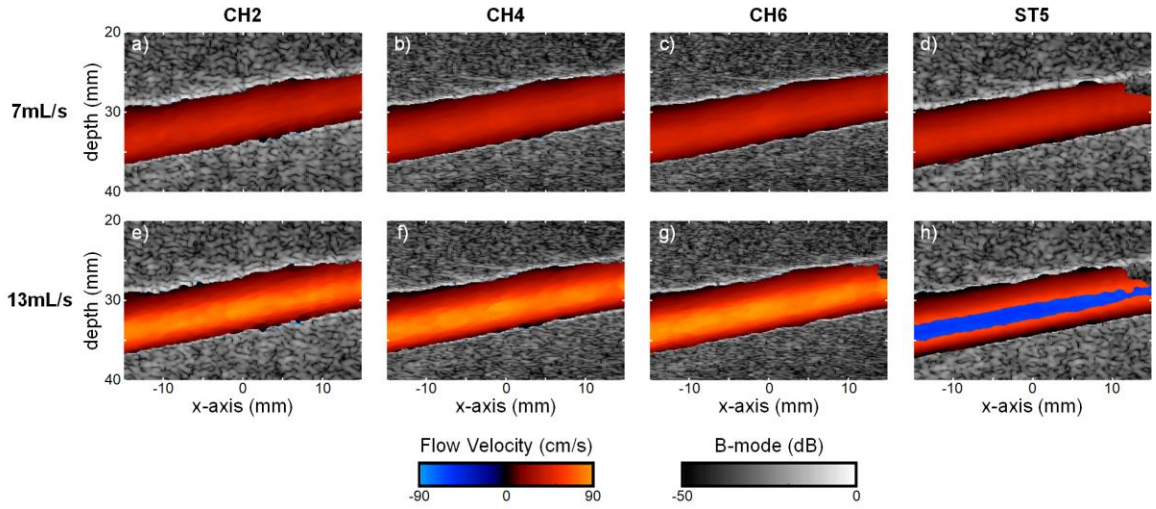


Figure 3-3 Color flow images at (a-d) 7mL/s flow rate and (e-h) 13mL/s flow rate for each of the four tested transmissions. The peak velocity in the 7mL/s flow was within the aliasing limit of the 5MHz center frequency of each transmission. The peak velocity in the 13mL/s flow exceeded the aliasing limit.

3.4.1.3 Reduced Transmission Pressure Experiments

The chirp transmissions utilized in the ChiVE framework are hypothesized to yield enhanced SNR in velocity estimation. Therefore, a functional test of the velocity estimation performance in a reduced SNR scenario was performed by reducing the transmission bias voltage applied to the CMUT array in both the ChiVE and CFI frameworks from 100V to 60V. The reduction in bias voltage yielded a lower transmitted pressure at 5MHz from 286.4 to 166.3kPa (measured by a hydrophone) and thus lowered the received echo signals returning to the array and in turn lowered the SNR. Like the previous flow estimation experiment, this experiment will assess the velocity estimation performance under these new conditions by calculating the RMSE between the measured velocity profiles at 3 cross-sections and the ideal parabolic profile. The RMSE values of the ChiVE and CFI frameworks will be directly compared as an indicator of relative performance in reduced SNR scenarios. In this study, only the CH6 and ST5 transmissions were compared.

3.4.2 Stenosed Carotid Bifurcation Phantom Experiments

To compare the ChiVE and CFI frameworks in a more challenging and clinically relevant scenario, experiments on a stenosed carotid bifurcation phantom were performed. In this study, a wall-less carotid bifurcation phantom with a 50% internal carotid artery stenosis was used. This phantom was fabricated

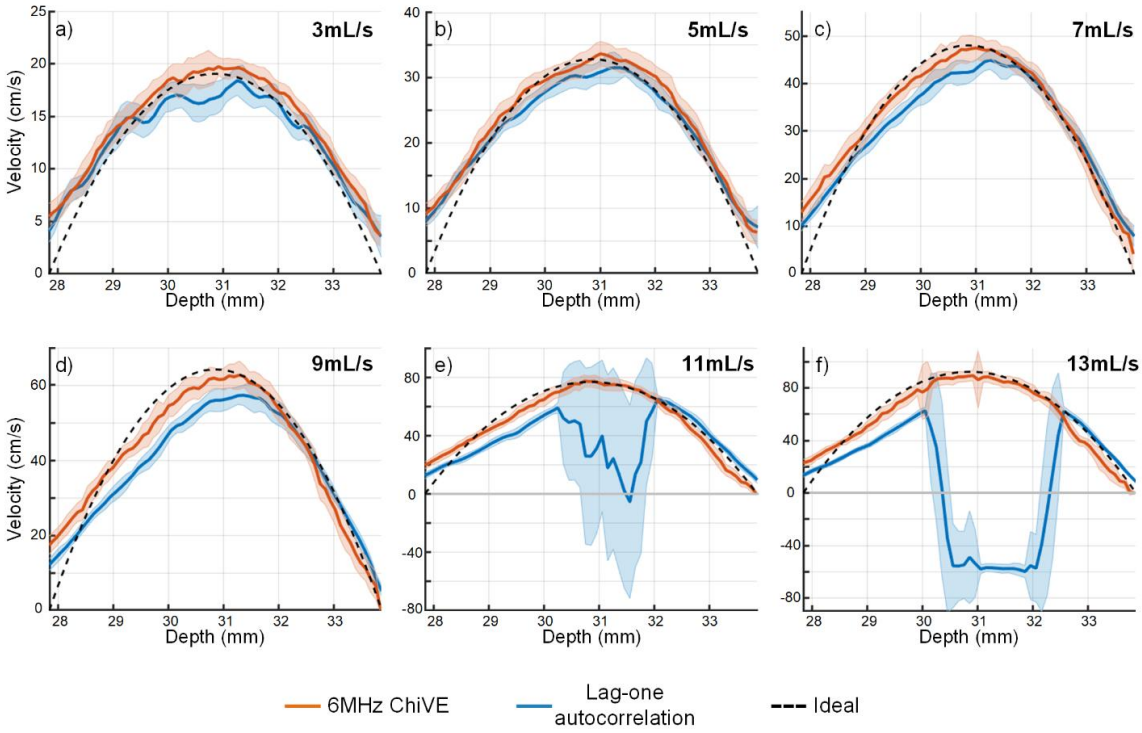


Figure 3-4 Flow profiles from flow rates ranging from 3 to 13mL/s including the ChiVE flow estimation with the CH6 transmission, lag-one autocorrelation with the ST5 transmission, and the ideal flow profile. The solid line indicates the mean estimate over 48 frames and the shaded region represents one standard deviation above and below the mean. (e) and (f) have the zero-velocity line marked in grey.

using the protocols described in previous work for tortuous vessel geometries (Ho et al., 2017). The composition of this phantom is identical to the straight tube phantom described above. The common carotid artery of the phantom was connected to the programmable flow pump via flow connectors and vinyl tubing. The internal and external carotid artery outlets of the phantom were connected back to the BMF reservoir to complete the flow circuit. In this study the flow pump was set to output a carotid pulsatile flow with a peak flow rate of 5mL/s and a pulse rate of 60 beats per minute. The flow estimation performance between the two frameworks will be qualitatively compared for the CH6 and ST5 transmissions.

3.5 Results

3.5.1 Chirp Transmissions Enhance Doppler SNR Over Standard Transmissions

The chirp transmissions were found to have an increased Doppler SNR compared to the standard pulse (with the same transmission bias). The CH2, CH4, and CH6 transmissions had Doppler SNRs of 22.8±5.4, 21.3±3.9, 22.6±3.6dB, respectively, whereas the ST5 transmission had a Doppler SNR of 13.4±5.2dB.

3.5.2 ChiVE Produces Aliasing Resistant Parabolic Velocity Profiles with Reduced RMSE

The CFI images produced by ChiVE appear similar to lag-one autocorrelation at modest flow rates and, at high flow rates, are found to be aliasing resistant when lag-one autocorrelation aliases. Figure 3-3 shows CFI images at flow rates of 7mL/s (a-d) and 13mL/s (e-h) for each ChiVE transmission and the standard transmission, respectively. In the 7mL/s case, all ChiVE cases perform similarly to the standard method. However, in the 13mL/s case aliasing has occurred in the standard transmission estimation but not in the ChiVE estimations. Yet, even in flow scenarios without aliasing, ChiVE was found to improve the estimation of peak velocities in the flow profiles. Figure 3-4 shows the cross-sectional flow profiles for ChiVE with CH6 compared to lag-one autocorrelation with ST5 and the ideal flow profile. In general, ChiVE estimations have a better resemblance of a parabolic flow profile [Figure 3-4(a-d)] and maintain this shape even if the PRF is sampling below the Nyquist limit when lag-one autocorrelation is afflicted by aliasing [Figure 3-4(e-f)]. Despite the three-times increased bandwidth from ST5 to CH6, ChiVE achieves similar standard deviations to lag-one autocorrelation.

When the RMSE was analyzed, ChiVE was found to perform outperform lag-one autocorrelation with statistical significance in nine of twelve tested cases. Also, the full implementation of ChiVE generally performed better than the simplified version without the third module of the framework. The RMSE for all cases was found to be normally distributed (Kolmogorov-Smirnov test at x = -10, 0, 10mm, respectively for each flow rate: 3mL/s – p=0.12, 0.53, 0.37; 5mL/s – p=0.67, 0.88, 0.42; 7mL/s – p=0.012, 0.23, 0.97; 9mL/s – 0.31, 0.90, 0.29). The RMSE between test cases was found to have unequal variances (Levene's test: $p<0.01$), therefore Welch's ANOVA was used to test for main effects in the data. In every cross-sectional location and at every flow rate a significant main effect was detected through Welch's ANOVA ($p<0.01$). A Welch's t-test (with the p-value corrected by a factor of six to

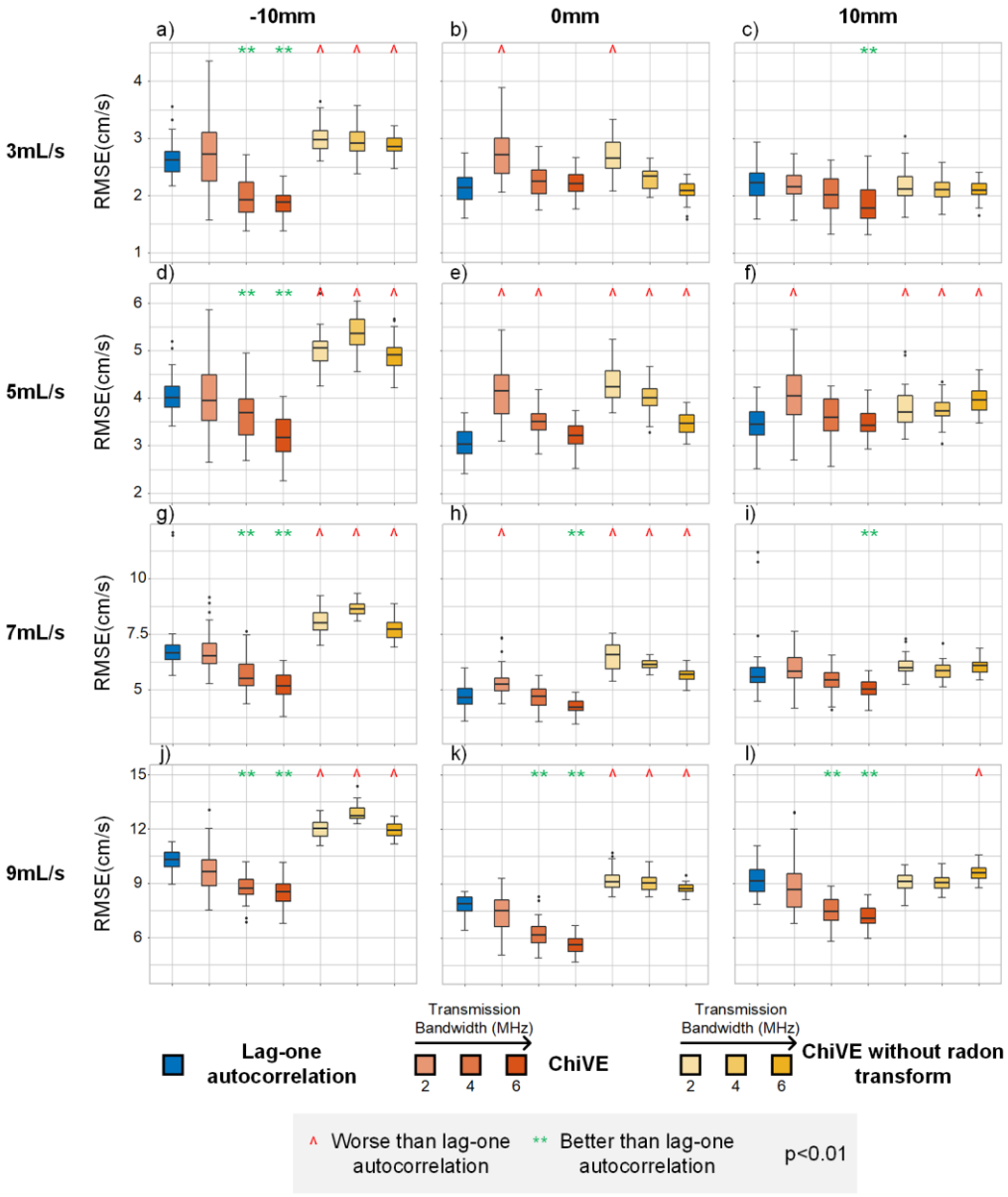


Figure 3-5 RMSE box-whisker plots for (a-c) 3, (d-f) 5, (g-i) 7, and (j-l) 9mL/s at three vessel cross-sections (x = -10, 0, 10mm) for lag-one autocorrelation, ChiVE at three transmission bandwidths, and ChiVE with the modal velocity estimator (radon transform step) removed. The boxes signify the range from the first to the third quartile of each dataset where the centerline is the median value. The whiskers represent the interquartile range (i.e. Q3+1.5*IQR where IQR = Q3-Q1) and the dots are outliers beyond that range. Significance of $p<0.01$ is indicated separately for results with lower RMSE than lag-one autocorrelation and results with higher RMSE.

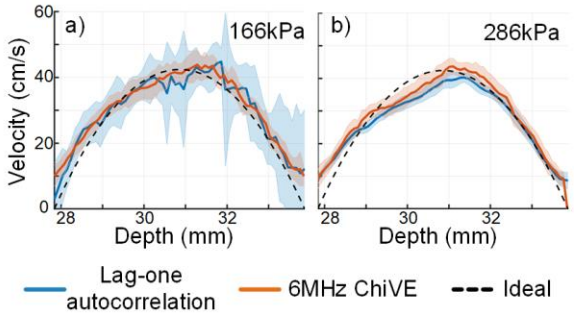


Figure 3-6 Flow profiles at 7mL/s flow rate with (a) 166kPa transmission pressure and (b) 286kPa transmission pressure. The solid line indicates the mean estimate over 48 frames and the shaded region represents one standard deviation above and below the mean.

account for each instance of ChiVE being compared to lag-one autocorrelation) was used to determine the specific effects. Note that at the 7mL/s flow rate, two out of the 48 ST5 frames processed by lag-one autocorrelation contained strong artifacts and were omitted from the statistical analysis. To better visualize the differences in performance, the RMSE is plotted for each algorithm on a box-whisker plot (Figure 3-5) for the flow rates below the aliasing limit at the 5MHz center frequency. Figure 3-5 also contains the results for the simplified ChiVE algorithm in which the velocity estimates are extracted before the radon transform is performed. Here, it is observed that ChiVE with CH6 most often has the lowest RMSE; the improvement of CH6 over lag-one autocorrelation with ST5 is statistically significant ($p<0.01$) in all but 3 plots shown [Figure 3-5(b, e, f)]. Also, there is a decrease in the RMSE of ChiVE corresponding to the increase in transmission bandwidth in all tested cases. The simplified version of ChiVE without the radon transform generally has a higher median RMSE than lag-one autocorrelation and never outperforms lag-one autocorrelation with statistical significance.

3.5.3 ChiVE Maintained Performance in a Reduced SNR Scenario

When tested at a reduced transmission pressure (166kPa from 286kPa), the performance of ChiVE was minimally impacted compared to lag-one autocorrelation. Figure 3-6 shows the estimated centerline flow profiles form a straight tube vessel with transmission pressures of 166kPa (a) and 286kPa (b). The performance of ChiVE is consistent both in error and variance between (a) and (b) whereas lag-one autocorrelation has increased error and variance. The data at both 166kPa and 286kPa were found to be normally distributed (Kolmogorov-Smirnov test at 60V: $p=0.054$; 100V: $p=0.49$) with unequal variances (Levene's test at 60 and 100V: $p<0.01$). Welch's t-test indicated that the RMSE distributions for lag-one autocorrelation (median RMSE of 4.2cm/s) and ChiVE (median RMSE of 4.3cm/s) were

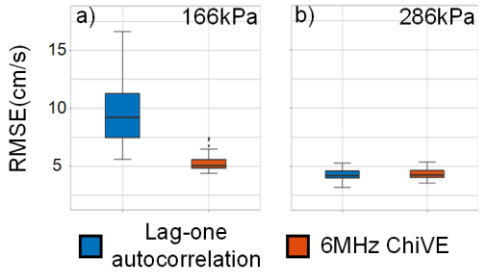


Figure 3-7 RMSE box-whisker plot for 7mL/s flow rate with (a) 166kPa transmission pressure and (b) 286kPa transmission pressure. The boxes signify the range from the first to the third quartile of each dataset where the centerline is the median value. The whiskers represent the interquartile range (i.e. Q3+1.5*IQR where IQR = Q3-Q1) and the dots are outliers beyond that range.

not significantly different at 286kPa (p=0.48). At 166kPa, the RMSE of ChiVE (median RMSE of 5.0cm/s) was significantly lower than lag-one autocorrelation (median RMSE of 9.2cm/s) ($p<0.01$). Figure 3-7 shows a box-whisker plot of the RMSE for both pressures and both transmissions. Here, the change in RMSE is very apparent in the lag-one autocorrelation when the transmit pressure is lowered. In this test, the Doppler SNR at 166kPa was -3.2±4.49dB and 6.14±3.21dB for ST5 and CH6, respectively. At 286kPa, the SNRs were 12.27±5.3dB and 18.82±3.42dB respectively.

3.5.4 ChiVE Can Map Dynamic Flows Across the Cardiac Cycle

ChiVE was found to produce aliasing-free flow estimations in a 50% stenosed carotid bifurcation phantom with pulsatile flow. Movie 3-1 shows a complete cardiac pulse cycle in the bifurcation phantom estimated using ChiVE with CH6 (a) and lag-one autocorrelation with ST5 (b). Throughout the cardiac cycle, ChiVE remains aliasing-free and produces a smooth color flow map. In contrast, lag-one autocorrelation has large, aliased regions for most of the systolic phase and sporadic inconsistencies during the diastolic phase. Figure 3-8 showcases a frame from peak systole and end diastole for each method from Movie 3-1. ChiVE demonstrates aliasing-free performance during the systolic phase while the standard method is one-cycle aliased [see snapshot in Figure3-8(a-b)]. During diastole, ChiVE demonstrates a more stable performance on the slow flow than lag-one autocorrelation, especially within the lower branch of the bifurcation [Figure 3-8(c-d)]. The regions of slowest flow (i.e. near the wall at diastole) contained more noise in lag-one autocorrelation compared to ChiVE.

At systole, ChiVE better traced the maxima and minima of the flow compared to lag-one autocorrelation. Figure 3-9 shows the Doppler spectrogram from the ST5 pulse at a range gate in the

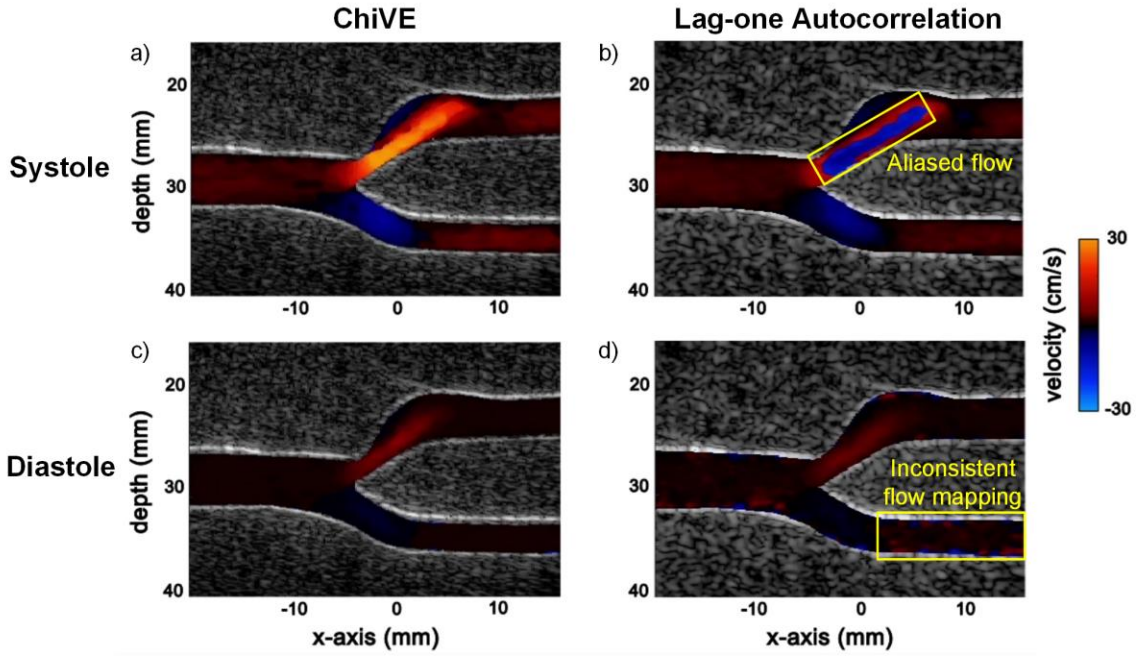


Figure 3-8 Snapshots from Movie 3-1 (a) and (b) at systole for ChiVE and lag-one autocorrelation respectively and (c) and (d) at diastole.

stenosed region of the bifurcation phantom in Movie 3-1. The traces overlayed on the spectrogram are the velocity estimations from ChiVE with CH6 (yellow) and lag-one autocorrelation with ST5 (red) from the same spatial location as the spectrogram. The peak flow estimation from ChiVE surpassed the two-cycle aliasing limit and better follows the upper limit of the Doppler spectrogram compared to lag-one autocorrelation. The velocity estimations from ChiVE are inherently aliasing-free whereas the velocity estimations from lag-one autocorrelation were manually de-aliased.

3.6 Discussion

3.6.1 Statement of Contribution

This work presents the first Doppler velocity estimation technique that is fully customized for chirp-coded transmissions. The use of chirps has previously been shown to enhance Doppler and B-mode SNR (Ramalli et al., 2021, Pederson et al., 2003, Chiao & Hao, 2005, Misaridis & Jensen, 2005b, Oelze, 2007), but their high bandwidths have limited their application in velocity estimation as it leads to large variances in traditional velocity estimation frameworks. The ChiVE framework, by contrast, leverages the wideband nature of chirps and the linearity of the Doppler equation to enhance the velocity

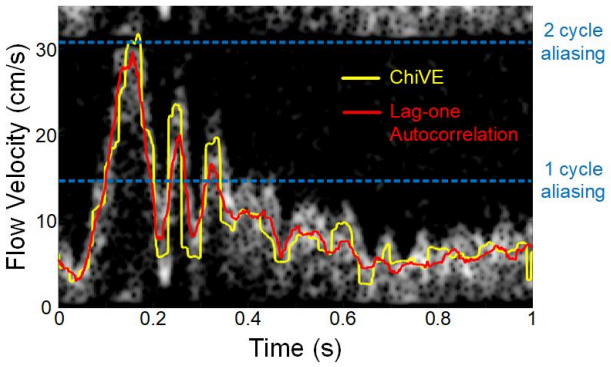


Figure 3-9 Doppler spectrogram of the carotid bifurcation phantom flow from a range gate in the center of the stenosed region for the ST5 pulse. The velocity estimation traces at the same spatial location are overlayed for ChiVE with CH6 (yellow) and lag-one autocorrelation with ST5 (red). The lag-one autocorrelation trace and the spectrogram itself were manually unwrapped along the flow velocity axis. The aliasing limits are labelled in blue.

estimation while maintaining a low estimation variance. Our study focused on several key performance indicators including: 1) Doppler SNR, 2) flow estimation error, and 3) aliasing resistance. An average Doppler SNR increase of 8.8dB was found between all chirp transmissions and the ST5 transmission. When tested on a range of flow rates, the RMSE (shown in Figure 3-5) was significantly lower for ChiVE (with the highest bandwidth) compared to lag-one autocorrelation in 9 out of 12 cases. Figure 3-4 shows that ChiVE can produce smooth parabolic flow profiles with estimated peak velocities closer to the true peak than lag-one autocorrelation. Additionally, Figure 3-4 highlights the aliasing resistance inherent to the ChiVE framework that is unmatched by traditional methods. When tested at a reduced SNR, as shown in Figures 3-8 and 3-9, the velocity estimation performance of ChiVE is minimally affected compared to the baseline SNR whereas the estimation from lag-one autocorrelation is severely degraded. Finally, Figure 3-11 demonstrates the ability of ChiVE to track the extrema of the flow profile in a dynamic flow scenario. With these results, it has been demonstrated that the ChiVE framework succeeds in increasing the Doppler SNR of broad view imaging schemes while also providing accurate velocity estimation, even in the case of high velocity, dynamic flows. This outcome is promising for the use of chirps to enhance performance in high-frame-rate flow imaging studies with broad view transmissions.

3.6.2 Interpretation of Results

This study substantiated that chirp transmissions, coupled with pulse compression, are an effective means of increasing Doppler SNR which can, in turn, facilitate higher fidelity flow estimations in low-SNR scenarios. However, the increases in Doppler SNR observed in this work did not follow the anticipated trend in which the SNR increase scales proportionally to the time-bandwidth product of the chirp transmission (Wehner, 1995). The deviation from the expected trend is likely due to waveform non-idealities in the transmitted chirps; both varying pulse amplitudes and slight phase shifts compared to the ideal pulse were observed in hydrophone measurements of the chirp transmissions. Since the waveform distortions are more prominent in the higher bandwidth chirp transmissions, the Doppler SNRs produced were similar to that of the lowest bandwidth chirp transmission. Yet, in the low-SNR test, the ST5 pulse resulted in an unreliable velocity estimation with lag-one autocorrelation (median RMSE increase of 5.0cm/s) whereas the ChiVE estimation saw only a modest increase in RMSE compared to the baseline transmission pressure (median RMSE increase of 0.7cm/s). Moreover, the velocity estimates in the lower branch of the bifurcation model were visibly smoother with ChiVE because of the increased SNR (see Figure 3-8). The difference in performance between ChiVE and lag-one autocorrelation in low SNR conditions highlights the performance impact of increasing Doppler SNR in broad view imaging.

The specialized design of the flow estimation pipeline of the ChiVE framework also contributed to the improved performance compared to lag-one autocorrelation. By considering a frequency spectrum rather than an isolated frequency value, ChiVE is more robust to estimation errors. A key novelty in the design of the ChiVE framework is the use of the radon transform to extract the RF-Doppler frequency trend. Using the maximum of the radon transform projection rather than linearly fitting the individual mean Doppler frequency components produces a modal velocity estimation instead of a mean velocity estimation. This methodology was well-justified according to the results in Figure 3-5 where a poor relative performance of the mean frequency fitting method is observed. The modal velocity estimation also contributes to a better estimation of the peak velocities in the parabolic profiles compared to lag-one autocorrelation (see Figure 3-4).

The velocity estimations produced by ChiVE have also been shown to be resistant to aliasing when imaging high velocity flows. Our results show that ChiVE is aliasing resistant on flows that were 2.2-times the aliasing limit of the center frequency (5MHz) or 3.4-times the aliasing limit of the peak frequency (8MHz). Aliasing resistance was demonstrated in a highly dynamic flow scenario as well as

for constant flow. As a result, post-hoc de-aliasing algorithms (Muth et al., 2011, Yatchenko et al., Nahas et al., 2020) may not be required in many scenarios when using ChiVE thereby removing additional processing steps after the velocity estimation. Nevertheless, it must be noted that ChiVE is not an aliasing-proof framework. When the slope of the Doppler and RF components becomes too steep, the algorithm may not be able to reliably extract the trend. Thus, the aliasing resistant limits of ChiVE should be determined to ensure it always operates within those conditions, otherwise, novel aliasing-related error removal methods would need to be developed (e.g. extrapolation of incorrect flows).

3.6.3 Limitations and Future Work

This work has demonstrated the capabilities of a framework to increase Doppler SNR while also enhancing flow estimation accuracy through wideband transmissions, yet there are still some limitations and directions that require follow-up. First, a more thorough investigation of the effect of chirp transmission parameters on the framework performance should be performed. Such an investigation should include additional chirp duration and bandwidth combinations to assess the Doppler SNR gain limits as well as to inspect unwanted effects such as spatial averaging of the velocity estimates stemming from the long duration chirps. Additionally, a study on different chirp center frequencies should be performed to investigate the effects of attenuation and dispersion on the framework. These effects are predicted to become more prominent as the frequency contained in the chirp increases (either from higher center frequency or higher bandwidth) and may limit the applicability of ChiVE in applications such as deep vessel imaging.

A second study direction is on the computational efficiency of the ChiVE framework. The addition of frequency spectrum analysis in this framework adds significant computational complexity compared to lag-one autocorrelation. Therefore, GPU-based acceleration of the framework is required for real-time velocity estimations. A real-time mode for this framework is likely to operate with a live visualization at 30-60Hz and a slow-motion playback at the PRF limited frame rate similar to previous implementations in HiFRUS (Yiu et al., 2019).

Finally, the Doppler SNR enhancement shown in this work is of benefit to broad view imaging in general, however, its benefits may be even greater if extended to the field of high-volume-rate imaging. Currently, 3D ultrasound imaging with 2D matrix arrays suffers from low SNRs which are critically reduced by utilizing broad view transmissions. Furthermore, the use of channel count reduction

strategies such as sparse matrix arrays reduces the SNR even further (Maffett et al., 2022). Thus, a key area of future investigation is the application of the ChiVE framework in high-volume-rate flow imaging studies.

3.7 Conclusions

HiFRUS flow imaging with broad view transmissions is hindered by low SNR, yet traditional methods of SNR enhancement such as chirp coded excitations are known to undesirably increase the Doppler estimation variance. Here, we described a novel velocity estimation framework called ChiVE which leverages chirps to increase the Doppler SNR without increasing the Doppler estimation variance. This framework produces more accurate velocity estimates than lag-one autocorrelation while providing aliasing resistance to over twice the Nyquist limit of the center frequency. With the ChiVE framework, Doppler ultrasound is no longer limited to narrowband transmissions for high quality velocity estimations, in fact wideband transmissions have been shown to have several notable advantages. This framework improves performance when acquiring B-mode and Doppler data in a single transmission as it eliminates any trade-off between velocity estimation accuracy and transmission bandwidth, thereby maximizing the achievable framerate. Finally, it is predicted that the Doppler SNR and corresponding velocity estimation improvements shown here will be invaluable when applied to high-volume-rate 3D flow imaging with broad-view transmissions.

Chapter 4
Unfocused Field Analysis of a Density-Tapered Spiral Array for High-Volume-Rate 3-D Ultrasound Imaging

© 2022 IEEE. Reprinted, with permission, from R. Maffett, et al., "Unfocused Field Analysis of a Density-Tapered Spiral Array for High-Volume-Rate 3-D Ultrasound Imaging," *IEEE Trans. Ultrason. Ferroelectr. Freq. Control*, vol. 69, no. 10, Oct. 2022.

4.1 Introduction

Dynamic 3-D ultrasound imaging has demonstrated potential in tracking physiological events such as blood flow on a time-resolved basis (Holbek et al., 2016, Correia et al., 2016). However, the development of dynamic 3-D ultrasound methods is dependent on high-volume-rate acquisitions [e.g., 1000 volumes per second (vps)] that cannot be realized using conventional 3-D imaging strategies based on mechanical scanning, as these strategies typically yield volume rates below 1 vps. The advent of 2-D matrix arrays has been a major step in this field that increased volume rates significantly over the physical scanning of linear arrays (from <1 to ~10 vps) (Fenster et al., 2001, von Ramm & Smith, 1990); yet, the volume rate remains too low to image dynamic flow events within a single cardiac cycle if traditional scanline (focused beam) imaging is used (Hoskins, 2010). To address the volume rate limitations of 3-D scanline methods, unfocused transmission schemes developed in 2-D ultrasound (Jensen et al., 2016a, Jensen et al., 2016b) could potentially be extended into the 3-D imaging space. Unfocused transmissions have enabled 2-D ultrasound imaging at rates of 10,000 frames/s through the insonification of the full imaging view on each firing. Nevertheless, the extension of unfocused transmission schemes from 1-D arrays to 2-D matrix arrays is nontrivial given the immense increase in element count.

A 2-D matrix array typically contains over 1000 transducer elements [e.g., (Petrusca et al., 2018)] that correspond to high channel counts as well as high pre-beamformed data rates. The costs of using 2-D matrix arrays become especially apparent in unfocused imaging schemes where all elements are receiving data simultaneously. The corresponding data rates on 2-D matrix arrays can easily exceed 50 GB/s depending on the acquisition parameters (i.e., pulse repetition frequency and sampling rate). Such high data rates are not manageable by clinical or research ultrasound scanners [e.g., Verasonics or ULA-OP 256 (Boni et al., 2016)] without hardware modifications, thereby rendering high-volume-rate 3-D

ultrasound investigations with 2-D matrix arrays unattainable except on highly specialized and bulky systems (Petrusca et al., 2018, Jensen et al., 2013). To make high-volume-rate ultrasound studies available for the wider research community, data rate reduction strategies must be developed to eliminate the need for expensive scanner hardware modifications. A more economical approach is to reduce the data rates directly from the probe rather than altering the scanner. Currently, there are two proposed solutions that reduce data rates directly on the probe: row–column addressing (RCA) and sparse arrays. RCA arrays maintain the element density of 2-D matrix arrays and reduce channel counts via crossed electrodes where only entire rows and columns can be addressed at a time (Morton & Lockwood, 2003, Demore et al., 2009). However, RCA prevents full 3-D steering and halves the maximum volume rate (Holbek et al., 2016). Sparse arrays instead reduce the element density to reduce the channel counts. This latter type of 2-D array is not subjected to constraints in 3-D steering and volume rate that are faced by RCA arrays.

In general, 2-D sparse arrays have the potential in realizing high-volume-rate 3-D ultrasound imaging. Yet, the beam degradation arising from exceeding a $\lambda/2$ element spacing may hinder the ability of sparse arrays to produce accurate flow measurements. Therefore, for sparse arrays to truly be suitable for high-volume-rate 3-D ultrasound, the arrays must be appropriately designed so that they can produce high-quality field transmission profiles. Many studies have focused on optimizing the layout of sparse arrays using in silico methods (Lockwood & Foster, 1996, Trucco, 1999, Yen et al., 2000, Austeng & Holm, 2002, Martínez-Graullera et al., 2010, Diarra et al., 2013, Ramalli et al., 2015, Roux et al., 2016). To robustly assess the performance of prototype sparse arrays in a range of transmission conditions, direct field profile measurements should be acquired. Such measurements will allow researchers to mitigate imaging irregularities stemming from nonideal beam profiles in any imaging mode. They are also important to exposure safety assessments in determining whether the generated acoustic intensities are within regulatory limits, such as those set forth by the Food and Drug Administration (FDA) (Duck, 2007).

In this work, we assess the acoustic field performance and the safety of a spiral array transducer with a sparse 2-D aperture to determine whether it can properly support the realization of high-volume-rate 3-D ultrasound imaging. Specifically, we evaluate the field profiles of unfocused transmissions (both plane and diverging waves) from a density-tapered spiral array, which has demonstrated high-quality focused beam characteristics in silico (Ramalli et al., 2015) and in vitro (Savoia et al., 2018) but has yet to be investigated for unfocused beam transmissions. In addition, we examine the surface

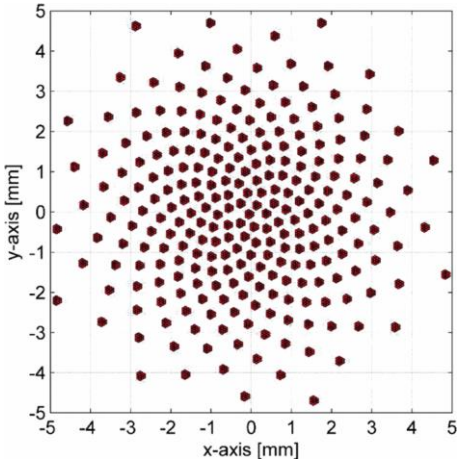


Figure 4-1 Layout of the physical CMUT density tapered spiral array with hexagonal elements.

temperature of the array to evaluate its safety for future in vivo studies. The physical array studied in this work is a density-tapered spiral array design that preserves the nongridded and nonsymmetric layout, and it was realized through a capacitive micromachined ultrasound transducer (CMUT) fabrication approach (Savoia et al., 2018). We posit that the transmission characteristics of the spiral array, such as beam intensity and arrival time profile, will be preserved in unfocused transmission modes. The field profile analysis, performed both in silico and in vitro, will examine both steered and unsteered transmissions over a range of depths relevant to peripheral vascular imaging in vivo. This study serves to lay the groundwork for future applications of the density-tapered spiral array as a viable transducer configuration for high-volume-rate 3-D ultrasound imaging of physiological dynamics.

4.2 Experimental Methods

The rationale for performing both hydrophone measurements and field profile simulations in this study is twofold. First, hydrophone measurements can directly assess the true transmission properties of an array, whereas simulations provide reference profiles to ensure that there is no systemic error from the experimental setup. Second, direct field profile measurements will be subject to nonidealities of the array (e.g., nonuniform element excitations and sensitivity), whereas simulation results have idealized array performance, which provides a theoretical base for the hydrophone measurements.

The density-tapered spiral array used in this study is a CMUT array with 256 elements (Ramalli et al., 2015, Savoia et al., 2018). It has a two-way–6-dB bandwidth centered at 7 MHz. The array, shown

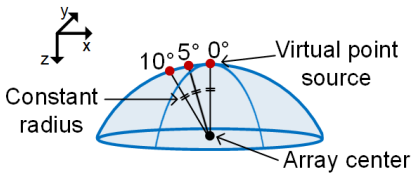


Figure 4-2 Schematic of diverging wave steering. Virtual point sources are shifted on the surface of a sphere centered at the center of the array to maintain a constant degree of divergence with steering.

Table 4-1 Transmission, measurement, and medium properties.

Parameter	Experimental Setup	Simulation
Center frequency	7.5 MHz	
Pulse shape	5-cycle sinusoid	
Window	20% Tukey	
Sampling frequency	100 MHz	
Speed of sound	~1480 m/s (degassed water)	1480 m/s
Wavelength	~197.3μm	
Attenuation	~0 dB/cm·MHz	0 dB/cm·MHz
Spatial sample spacing	100 μm (~λ/2) or 200 μm (~λ)	50 μm (~λ/4)
Spatial averaging	0.13 mm^2	0 μm^2

in Figure 4-1, has hexagonal elements with a diameter of 220 μm where each element is composed of 19 circular subelements. The elements follow a Blackman window-based density tapering with the center and edges of the array containing, respectively, the highest and lowest element spatial density. This type of density tapering is used here since it was found to have a favorable performance tradeoff (in focused beam simulations) between various parameters, including lateral resolution, grating lobe levels, and effective aperture for small vessel imaging compared to other density tapering functions of the Fermat spiral (Ramalli et al., 2015). The total footprint of the array is a circular surface with a 1 cm diameter. With density tapering, the effective array diameter is 0.6 cm.

Three types of unfocused transmissions were studied: 1) plane wave (PW); 2) diverging wave with a virtual point source 30 mm behind the array (DIV30); and 3) diverging wave with a virtual point source 20 mm behind the array (DIV20). Every pulsing event involved the use of a five-cycle, 7.5-MHz

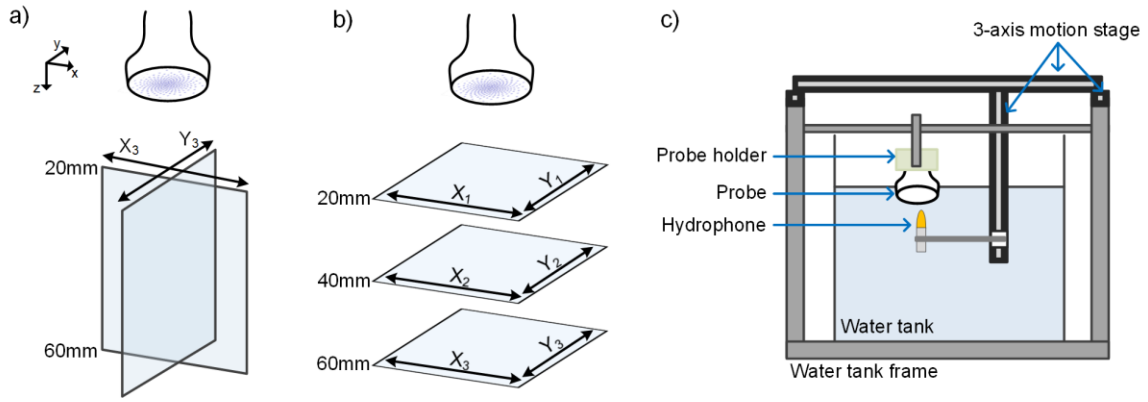


Figure 4-3 (a) Acquisition planes on the XZ- and YZ- planes where the width in X_3 is two-times the theoretical beam width at 60 mm depth. (b) Acquisition planes on XY-planes where the widths $X_{1,2,3}$ and $Y_{1,2,3}$ are defined by the theoretical beam width at each depth. (c) Schematic of the hydrophone measurement setup with the hydrophone mounted to the 3-axis motion stage and the spiral array mounted to the water tank frame.

sinusoidal pulse with a 20% Tukey window. The pulse parameters were selected to generate the typical pulse used for pulsed Doppler measurements. The array was biased at 75 V (the maximum voltage without damaging the array elements), and a working voltage of 20 V peak-to-peak was used for all transmissions. No transmit apodization was applied on the array since the density tapering serves as a physical apodization. The DIV30 and DIV20 firings were studied at transmission angles of 0°, 5°, and 10° with the virtual point source maintaining a constant distance from the center of the array (see Figure 4-2). The PW firings were studied at transmission angles of 1°, 5°, and 10°; 0° was not studied because it caused unexpected behavior of the pulsers due to the high peak current required during the simultaneous firing of all 256 elements. The range of steering angles studied in this work was an empirical parameter choice that was made based on previous studies that often used an angle span of 20° (i.e., from −10° to +10°) for multi-angle Doppler estimation (Yiu & Yu, 2016). Complete transmission specifications are listed in Table 4-1.

The pressure field profile was acquired over two planes perpendicular to the probe surface and three planes parallel. The perpendicular planes, one on the XZ plane and one on the YZ plane, had a width of two times the theoretical maximum main beamwidth in the X - and Y -directions. They each spanned from 20 to 60 mm depth in the Z -direction [see Figure 4-3(a)]; this range in depths of the measurement planes was set to match the typical depths used in peripheral vascular imaging (e.g., brachial and carotid). The remaining three acquisition planes were parallel to the probe surface on XY planes at

depths of 20, 40, and 60 mm and were sized to match the maximum main beamwidth as well as centered with the main beam [see Figure 4-3(b)].

4.2.1 Hydrophone Measurements

Hydrophone measurements were performed in a degassed water tank (20 °C, ~1480 m/s) with an attached three-axis motion stage (IntelLiDrives, Inc., Philadelphia, PA, USA). The motion stage has a 20-μm motion resolution on all three axes and was controlled by a personal computer. An Onda HGL-400 capsule hydrophone (Onda Corporation, Sunnyvale, CA, USA) was mounted on the motion stage and was immersed in the water tank [see Figure 4-3(c)]. The hydrophone was oriented such that the measurement surface was directed upward toward the array surface. This model of hydrophone has an aperture of 400 μm resulting in spatial averaging of the measurements at each point. The hydrophone was connected to an AH-2010-100 preamplifier (Onda Corporation, Sunnyvale, CA, USA) and the signal was routed to a Rigol DS1104 oscilloscope (Rigol, Portland, OR, USA) that sampled at 100 MHz. The same personal computer controlling the motion stage was used to read the hydrophone acquisitions from the oscilloscope.

The density-tapered spiral array was mounted on the water tank frame using a custom 3-D printed probe holder and was placed in the scan tank with the array pointing downward [see Figure 4-3(c)]. The probe orientation thus had a fixed alignment with the frame of the water tank. The surface of the array was located < 5 mm below the surface of the water. The array was driven by a ULA-OP 256 research ultrasound scanner (Boni et al., 2016) with a CMUT adapter board. A sync output from the scanner was also connected to the oscilloscope to provide a trigger for the hydrophone measurements. The scanner was controlled through a second personal computer where the transmission profiles were programmed.

With the array and hydrophone in place in the scan tank, the hydrophone was moved underneath the array. The origin of the XY scan planes for the hydrophone was set at the center of the array using a focused beam transmission from the array. Using increasingly fine step sizes, the hydrophone could be placed at the peak of the transmission with 50-μm accuracy. For steered transmissions, the origin was moved in the X- or Y-directions from the array center to the center of the steered beam. To set the desired depth of the hydrophone below the array, the time between the trigger pulse and the recorded wave on the hydrophone was measured on the oscilloscope. The time between the pulses (after subtracting a fixed transmission delay value) was multiplied by the speed of sound in the water, 1480

m/s, to yield the depth of the hydrophone below the array. The depth of the array was accurate to 50 μm.

To record the field profile of various transmissions, the hydrophone was stepped over a 2-D grid on the desired plane. For acquisition planes up to 9 cm^2 in area, a step size of 100 μm (λ/2) was used. For all larger acquisition planes, step sizes of 200 μm (λ) were used for intensity and arrival time analysis.

4.2.2 Field Profile Simulations

Simulations of the pressure field profile from the density tapered spiral array were performed in MATLAB (MathWorks, Natick, MA, USA) using Field II (Jensen & Svendsen, 1992, Jensen, 1997). The simulated array contained 256 square elements with a 200 μm width in the same locations as the physical spiral array. The element size between simulation and the physical array is similar since a 220-μm -diameter hexagon when measured from corner to opposite corner has a 200 μm width measured from side to opposite side. The simulated transmissions were set identically to the experimental transmissions and the simulated medium was set to match the properties of water. Unlike the hydrophone measurements, the simulated data points have no spatial averaging. All other key simulation parameters are listed in Table 4-1.

4.2.3 Intensity Analysis

The peak absolute pressure at each point on the acquisition planes was extracted and converted to decibels to yield the intensity of the point. The XZ and YZ planes were used to observe the beam properties across depth while also identifying secondary lobes outside of the main beam. In this work, secondary lobes are considered to be regions outside the main beam with an intensity close to the main beam intensity (e.g., greater than one-quarter of the main beam intensity). Their emergence may be attributed to grating lobes and sidelobes in the field profile. They were identified by applying a –12-dB intensity threshold relative to the main beam peak on each XZ and YZ plane. The XY planes were used to study the radial properties of the beam.

4.2.4 Arrival Time Analysis

The XZ and YZ planes were used to observe the propagation of the generated wavefront across depth. A cineloop of the wavefront propagation across depth can be formed by stepping sample-by-sample on all acquisition points on the XZ and YZ planes simultaneously and saving each sample time as a video frame. On the XY planes, the wavefront arrival time can be calculated at each acquisition point by

computing the lag of the maximum cross correlation between the excitation pulse and the measured waveform. To evaluate the main beam arrival time performance, the wavefront arrival time profiles in experiments and simulations were compared to an expected profile for the transmission. For PWs, the expected profile is simply a plane that matches the steering angle. For diverging waves, the expected profile takes the form of a hyperboloid. Specifically, for a given spatial point in front of the array aperture (x_o, y_o, z_o) and a virtual point source location (x_{vp}, y_{vp}, z_{vp}), the arrival time t of a diverging wavefront can be theoretically calculated from equation (4.1).

$$t^2 = \left(\frac{x_o - x_{vp}}{c}\right)^2 + \left(\frac{y_o - y_{vp}}{c}\right)^2 + \left(\frac{z_o - z_{vp}}{c}\right)^2 \tag{4.1}$$

where c is the speed of sound. The root-mean-squared error (RMSE) between the expected and acquired arrival time profiles was accordingly calculated for both simulations and experiments.

4.2.5 In Vitro B-Mode Imaging

Unfocused B-mode imaging performance of the array was assessed using two phantoms: 1) CIRS Multi-Purpose Multi-Tissue Ultrasound Phantom (CIRS, Inc., Norfolk, VA, USA) with an attenuation of 0.3 dB/cm·MHz and 2) an in-house fabricated wire target phantom immersed in water (100-µm tungsten wires aligned axially spaced 1 cm apart). Wire targets in both phantoms were imaged with the y -axis of the spiral array aligned parallel with the line targets. PW and DIV20 firings (the least- and most-divergent firings) were used with ten transmission angles spanning from −5° to 5° on the x -axis, omitting 0°, with no steering on the y -axis. A 3-D GPU-based delay-and-sum beamformer, essentially an extended version of the 2-D GPU beamformer (Yiu et al., 2011), was used to form the images for each transmission angle followed by coherent compounding of all angles. The resulting images were assessed for their penetration depth and spatial resolution. The penetration depth in the CIRS phantom was assessed qualitatively by observing at which depth the targets became indistinguishable from the surrounding speckle pattern. The spatial resolution was calculated from the full-width at half-maximum (FWHM) of the point targets in the x - and z -axes of the images of both phantoms. The average sidelobe level (SLL) was evaluated on the images from the water phantom on the ZX plane. The SLL was extracted from lateral positions of $x<-1.5$ mm and $x>1.5$ mm (to exclude the point target) and over an axial range from 5 pixels above the point target depth to the depth of the point target (to include the upward curving nature of the sidelobes). The average SLL for each point target was then normalized to the peak intensity of the point target.

4.2.6 Probe Surface Temperature Measurements

Surface temperature measurements on the array were acquired in accordance with the International Electrotechnical Commission (IEC) standard protocol (IEC 60601-2-37). In brief, a tissue-mimicking phantom made from a poly(vinyl)-alcohol hydrogel was immersed in a 33°C water bath for 1 h. Then, with the phantom still in the water bath, the probe was placed on the phantom surface. The probe was set to transmit a DIV20 transmission without steering at 5-kHz PRF for 30 min, after which an infrared camera (TG165, Teledyne FLIR, Wilsonville, OR, USA) was used to measure the temperature of the array surface. A final surface temperature of 43°C or less is considered safe for external in vivo use of an ultrasound array.

4.3 Results

4.3.1 Spiral Array Produces High-Quality Beam Profiles for Unfocused Firings

The density-tapered spiral array had measured peak negative pressures (PNPs) of 93.9, 59.3, and 45.6 kPa for PW, DIV30, and DIV20, respectively. Figure 4-4(a)–(i) shows the intensity of the XZ planes measured by the hydrophone. The left, center, and right columns, respectively, show the XZ planes for PW, DIV30, and DIV20 firings, whereas the top, middle, and bottom rows, respectively, show the XZ planes at the steering angle of 0°/1°, 5°, and 10°. The inset figure on each XZ plane is a binary map with a −12-dB threshold from the main beam peak applied. Overall, Figure 4-4 shows the intensity profiles across all transmission types. The PW firings show a consistent beamwidth across depth, while the DIV30 and DIV20 firings expand across depth as expected. The presence of secondary lobes in all firings is apparent from the intensity profiles; however, only a few of them are within the −12-dB threshold (i.e., higher than one-quarter) of the main beam intensity. Figure 4-4(j) and (l) shows an intensity cross-sectional plot taken at a depth of 40 mm and overlaid for each steering angle of the same transmission type. These plots highlight the secondary lobe levels compared to the main lobe. For PW [Figure 4-4(j)], the main lobe-to-secondary lobe ratio is 24.84 dB for 1° steering and 14.26 dB for 10° steering; for DIV30 [Figure 4-4(k)], it is 18.67 dB for 0° and 6.74 dB for 10°; and for DIV20 [Figure 4-4(l)], it is 18.45 dB for 0° and 14.40 dB for 10°. While not explicitly shown here for brevity, the array performed similarly between the x- and y-axis steering.

Figure 4-5(a)–(c) shows the XY plane of the 1° PW, 0° DIV30, and 0° DIV20 firings, respectively, at a depth of 40 mm as measured by the hydrophone. Figure 4-5(d) – (f) shows the same planes from

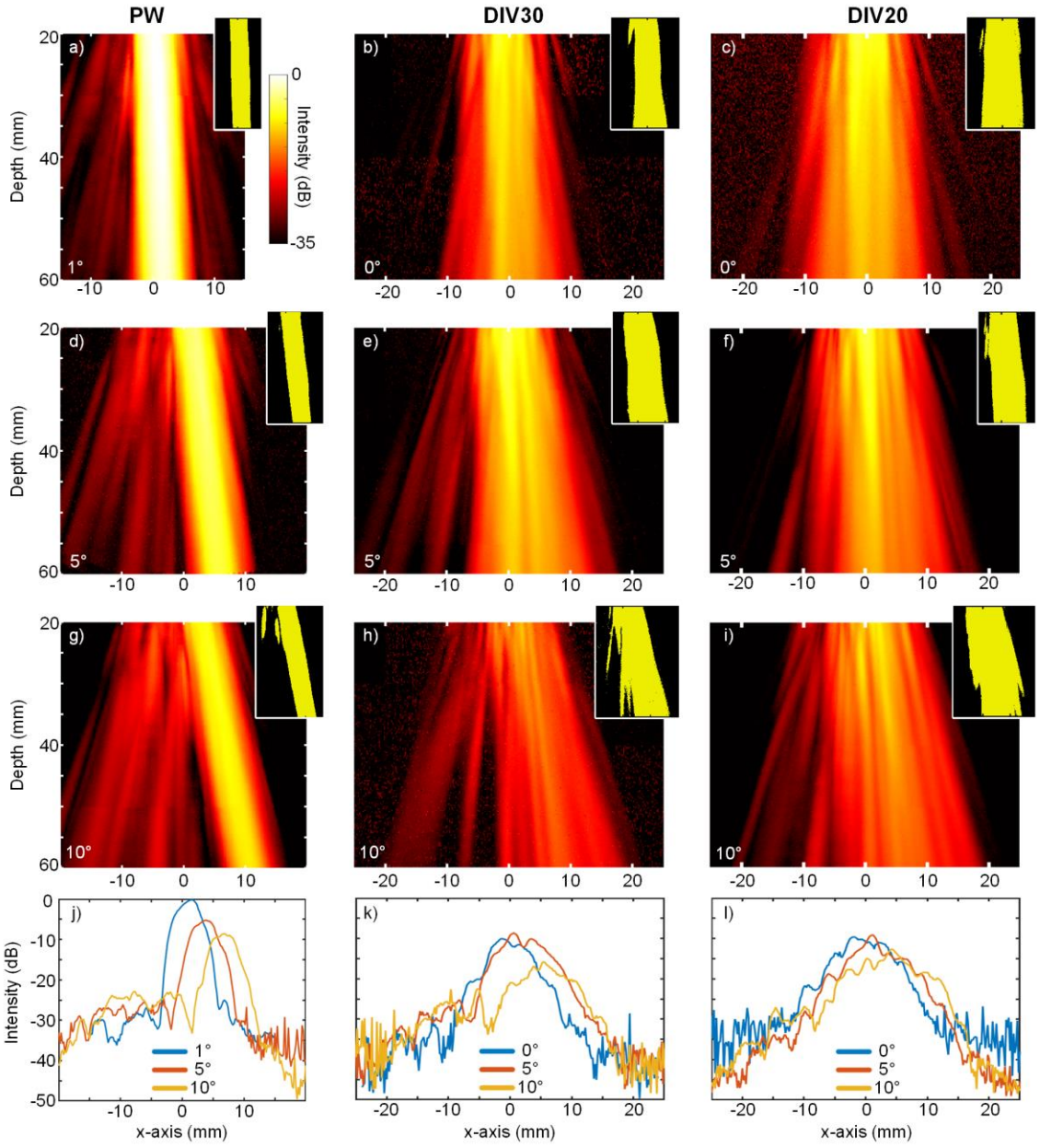


Figure 4-4 Intensity measurements for PW (left column), DIV30, (center column), and DIV20 (right column) for 0 and 1° steering (top row), 5° steering (second row), and 10° steering (third row). Insets in the top three rows of the figure show the beam intensity plots with a -12dB threshold applied. Intensity profiles at 40 mm depth are shown in the bottom row overlayed for each steering angle to highlight the reduction in main beam intensity with steering coinciding with the increase in secondary lobe intensity.

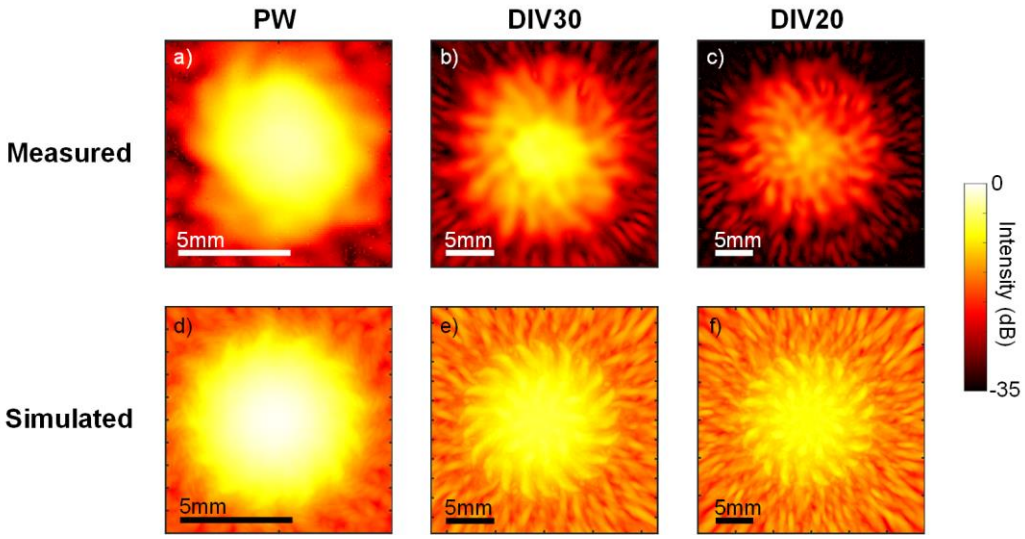


Figure 4-5 Intensity measurements on XY-planes at a depth of 40 mm in hydrophone experiments (top row) and simulation (bottom row) for PW (left), DIV30 (center), and DIV20 (right).

the simulated results. Here, the radial beam characteristics of the array can be observed and compared to the ideal performance of the simulated array. The simulated results show a uniform radial performance since each element is transmitting at identical amplitudes. The physical array has some beam imperfections resulting in a less uniform radial performance [e.g., Figure 4-5(a) has a less circular intensity pattern than Figure 4-5(d)]. On all XY planes in simulation and hydrophone measurements, there are no direction-dependent beam patterns and the main beams are relatively circular in nature. However, there is a notable difference in intensity between the hydrophone and simulated results, especially toward the outer edges of the main beam where the simulations show a much higher intensity than the hydrophone measurements.

4.3.2 Wavefronts Generated from the Spiral Array Match the Expected Profiles

Movie 4-1 shows the wavefront propagation for the 1° steered PW as well as 0° steered DIV30 and DIV20 firings on the XZ plane as measured by the hydrophone. Here, it can be observed that the wavefront profile remains consistent as it propagates without any significant distortion in the main beam area (highlighted by the white borders). Outside of the main beam, the secondary lobe wavefront has an uneven and fluctuating profile as it propagates in all cases. Figure 4-6(a)–(c) shows the snapshots from Movie 4-1 at three overlayed timepoints on each panel. The expected main beam profile is traced by the dotted lines and shows a close match to the measurements. Figure 4-6(a)–(c) also shows that the

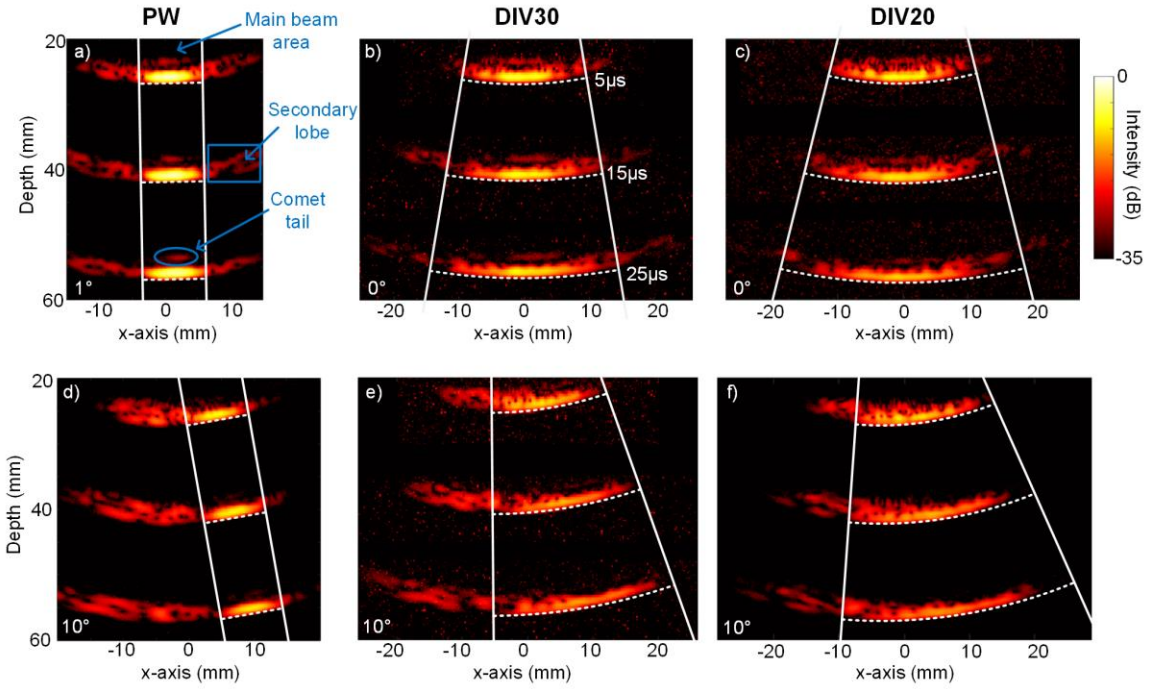


Figure 4-6 Top row: Overlayed stills from Movie 4-1 at 5, 15, and 25μs from the start of the acquisition on the oscilloscope for unsteered PW (a), DIV30 (b), and DIV20 (c) firings. Solid white lines mark the edges of the theoretical main beam. Dashed white lines mark the expected wavefront profile. Bottom row: Overlayed stills from Movie 4-2 at the same timepoints as the top row for PW (d), DIV30 (e), and DIV20 (f) firings steered at 10°.

wavefronts are followed by comet tails, which are secondary axial peaks that emerged as a result of using an element spacing larger than λ/2 on the sparse array aperture. Such artifacts in the beam profile correspondingly give rise to axial image artifacts near echogenic image features. Movie 4-2 shows a similar wavefront propagation for the 10° steered firings of each type. Here, the main beam wavefront again remains coherent over its axial course of propagation. Figure 4-6(d)–(f) shows the snapshots from the steered propagations and highlights the close match between the expected and measured profiles.

Figure 4-7 plots the wavefront profiles at a 40 mm depth, including the expected, simulated, and measured profiles. Figure 4-7(a), (d), and (g) shows the profiles for the PW firings, Figure 4-7(b), (e), and (h) shows the profiles for the DIV30 firings, and Figure 4-7(c), (f), and (i) shows the profiles for the DIV20 firings. Each row of Figure 4-7 shows a different steering angle of the firing with the top row being 0/1°, the center row 5°, and the bottom row 10°. The RMSE values of the simulated and measured profiles are shown in the figure panels. From the PW profiles, the wavefronts are observed

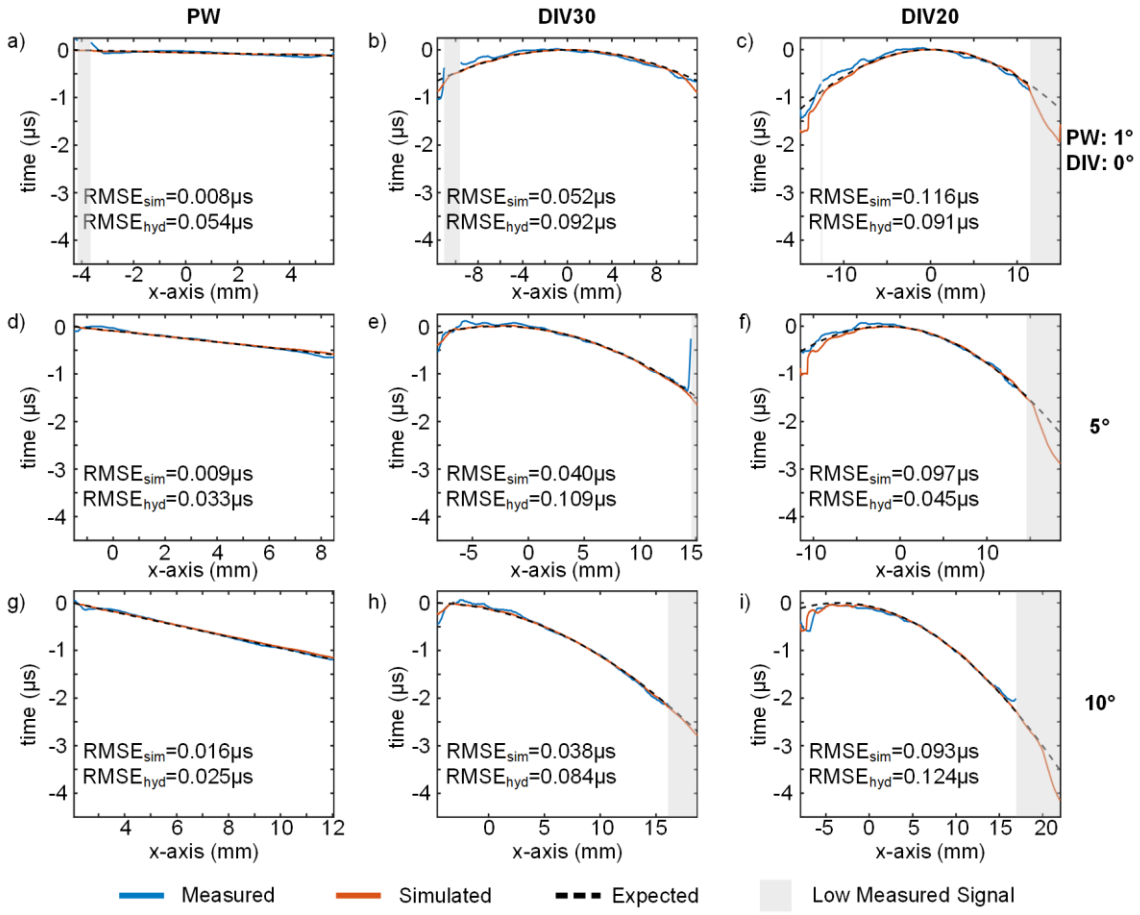


Figure 4-7 Cross sectional wavefront profiles for PW (left), DIV30 (center), and DIV20 (right) for 0 and 1° steering (top), 5° steering (middle), and 10° steering (bottom) at a depth of 40 mm. RMSE values calculated for the simulated and hydrophone profiles are shown as insets. Grey bars indicate regions where the voltage read from the hydrophone was within 2mV of the noise floor and therefore the wavefront could not be accurately identified. These regions were omitted in all RMSE calculations.

to have only minor deviations from the expected profile near the edges of the main beam where the intensity is lower. The DIV30 and DIV20 firings follow a similar trend with the center of the profile being the smoothest with increasing deviations toward the edges. Generally, the simulated data match slightly closer to the expected profile than the hydrophone data. However, in the case of the DIV20 firing, the simulated data show some deviation at the right and left sides of the plots due to the sparsity of elements at the edges of the array aperture and the widespread of the wavefront. In both the DIV30 and DIV20 firings, the hydrophone RMSE increases as the degree of steering increases, which is not

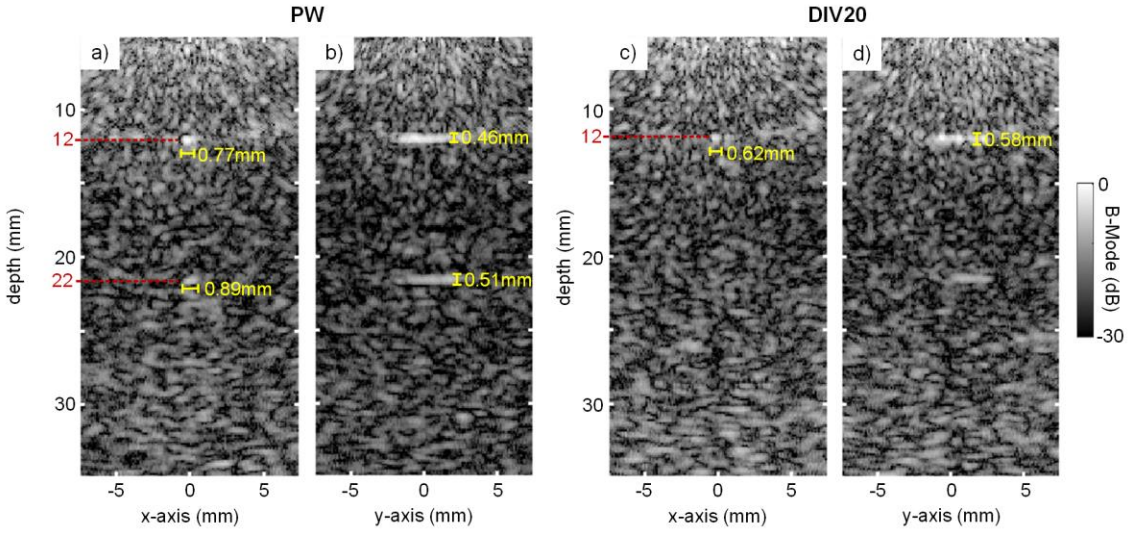


Figure 4-8 B-mode images of point targets in a CIRS phantom formed by the coherent compounding of 10 unfocused transmissions (steering -5° to 5° along the x-axis). a) PW image of XZ-plane at y=0, b) PW image of YZ-plane at x=0, c) DIV20 image of XZ-plane at y=0, and d) DIV20 image of YZ-plane at x=0.

observed in the simulated data. The PW RMSE values are lower than the other firings and show smaller changes in RMSE between firing angles.

4.3.3 Compounded Unfocused Firings Demonstrated High B-Mode Spatial Resolution with Limited Penetration Depth

B-mode images of a CIRS point target phantom (wire targets in 3-D) acquired with ten-angle compounded PW and DIV20 scans are shown in Figure 4-8. Figure 4-8(a) and (c) shows the B-mode slices on the x-axis of the array, which is perpendicular to the wires in the CIRS phantom. Figure 4-8(b) and (d) shows the B-mode slices on the y -axis of the array that is parallel to the wires. In Figure 4-8(a) and (b), the PW firings are able to resolve the wires to a depth of 22 mm with a lateral (x-axis) FWHM of 0.77 mm for the target at 12 mm depth and 0.89 mm for the target at 22 mm. The axial FWHM is 0.46 mm at 12 mm depth and 0.51 mm at 22 mm for PW. Figure 4-8(c) and (d) shows that the DIV20 firing was able to resolve the 12-mm target in the x - and y planes, but the 22-mm target is indistinguishable from the speckle pattern on the x plane and is only visible on the y plane. The lateral (x-axis) FWHM is 0.62 mm for the target at 12 mm depth and the axial FWHM is 0.58 mm for the same target.

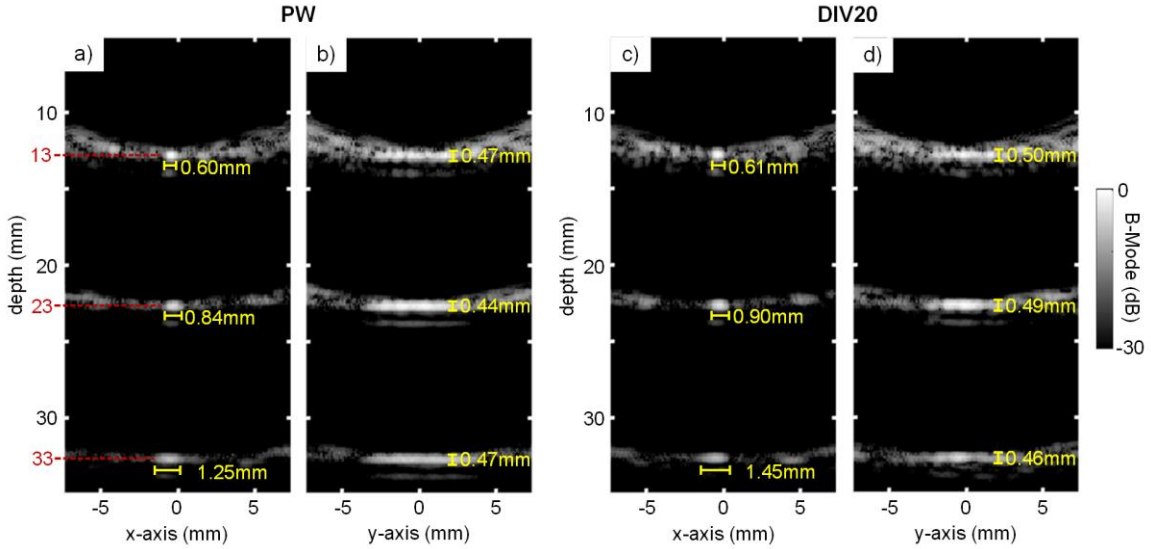


Figure 4-9 B-mode images of point targets in an in-house made wire target phantom immersed in water formed by the coherent compounding of 10 unfocused transmissions (steering -5° to 5° along the x-axis). a) PW image of XZ-plane at y=0, b) PW image of YZ-plane at x=0, c) DIV20 image of XZ-plane at y=0, and d) DIV20 image of YZ-plane at x=0.

Figure 4-9 shows the B-mode images for the same PW and DIV20 scans on the wire target phantom immersed in water. Here, the targets were resolvable in both PW and DIV20 scans to a depth of 33 mm. In Figure 4-9(a) and (b), the PW scans show a lateral FWHM of 0.60, 0.84, and 1.25 mm, respectively, for the 13-, 23-, and 33-mm depth targets. The axial FWHM on the same targets are 0.47, 0.44, and 0.47 mm. In Figure 4-9(c) and (d), the DIV20 scans produced the lateral FWHM of 0.61, 0.90, and 1.45 mm for the 13-, 23-, and 33-mm target depths along with the axial FWHM of 0.50, 0.49, and 0.46 mm, respectively. Generally, the FWHM results of the water-based phantom align with those on the CIRS phantom. A notable difference in the measurements is the presence of the secondary lobes, which is much more apparent with the hypoechoic background of the water-based phantom. For the PW scan, the average SLL was −19.46, −20.87, and −24.87 dB for the 13-, 23-, and 33-mm depth targets, respectively. For the DIV20 scan, the average SLL was −19.37, −22.91, and −21.29 dB. Figure 4-10 shows a contour plot of the ZX plane B-mode images in Figure 4-9 with intensity thresholds of −20, −12, and −6 dB. The secondary lobes are normalized to the peak value of their adjacent point target. Figure 4-10(a) shows the PW scan where the majority of the secondary lobes are between −20 and −12 dB. There are, however, localized pockets of higher secondary lobe intensity that surpass −12 dB. Figure 4-10(b) shows a similar representation for the DIV20 scan.

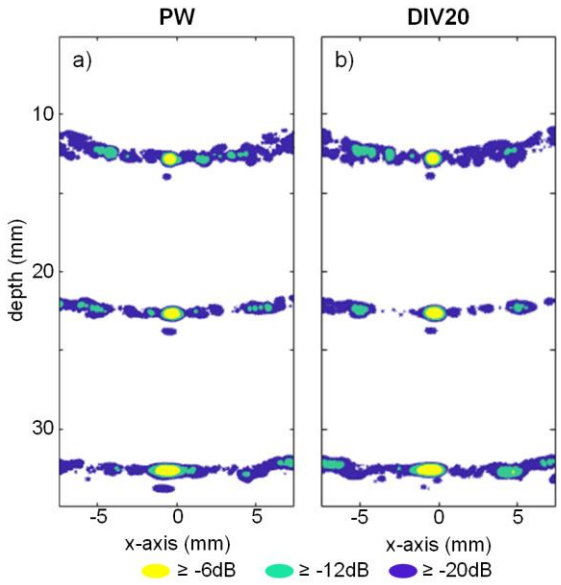


Figure 4-10 Contour plots of the B-mode images of the point targets in water for (a) PW scan [Figure 4-9(a)] and (b) DIV20 scan [Figure 4-9(c)] with thresholds of -20, -12, and -6dB to highlight the sidelobe intensity levels.

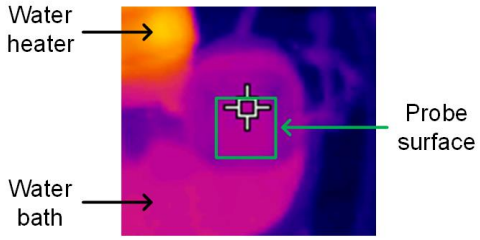


Figure 4-11 Infrared image of the probe surface acquired after 30 minutes of continuous transmission.

4.3.4 Surface Temperature and Acoustic Exposure Levels are Within Regulatory Limits

The surface temperature of the density-tapered spiral array was found to be 30.2°C ± 0.7°C (± one standard deviation) after 30 min of continuous transmission. This temperature is below 43°C limit set forth by IEC 60601-2-37 (Duck, 2007). Figure 4-11 shows an infrared image of the probe surface. The probe temperature was observed to be uniform across the entire surface.

Based on the established acoustic exposure formulas (Duan et al., 2019), the spatial-peak, pulse-average (SPPA) intensity and mechanical index (MI) of the PW mode were, respectively, 0.298 W/cm2

and 0.034 for a maximum unfocused PNP of 93.9 kPa (Section 4.3.1). For DIV30 and DIV20 that had the maximum measured PNP of 59.3 and 45.6 kPa, respectively (Section 4.3.1), the corresponding SPPA intensity was 0.119 and 0.070 W/cm^2, while the MI was 0.022 and 0.017, respectively. All the intensities and MI values reported here are below FDA's emission limits for diagnostic imaging (Duck, 2007).

4.4 Discussion

4.4.1 Statement of Contributions

This work presents a detailed study of unfocused transmission characteristics from the density-tapered spiral array to evaluate its viability in facilitating high-volume-rate 3-D ultrasound imaging. In principle, the use of a spiral array to facilitate 3-D imaging eliminates the need for expensive scanner hardware modifications and provides flexibility in imaging mode development. While the spiral array has previously been studied in focused firings (Savoia et al., 2018), here, we study unfocused transmissions that are essential to realizing high-volume-rate 3-D imaging, particularly for transmissions involving multicycle pulses that are required to perform flow mapping.

In our investigation, three acoustic field properties of unfocused firings have been evaluated for the spiral array: 1) beam intensity; 2) wavefront arrival time profile; and 3) B-mode image quality. Figure 4-4 highlights the uniformity of the unfocused beam intensity within the main beam region as well as demonstrates the relatively low secondary lobe intensity compared to the main beam. Movies 4-1 and 4-2 show that, despite the low element density, the wavefront profile remains smooth throughout propagation, while Figure 4-7 shows that the wavefronts have only small deviations from the expected profiles. Together, these results indicate that the array's sparsity does not dramatically impact wavefront shape. Figures 4-8 and 4-9 present the first compounded PW and diverging-wave images from the density-tapered spiral array, which shows promising spatial resolution. Yet, penetration depth remains limited, suggesting a need for the development of signal enhancement strategies (to be discussed in Section 4.4.3).

Another component of this investigation is an experimental analysis of the spiral array's exposure safety when it operates under unfocused transmission modes. The maximum unfocused PNP measured by the hydrophone was 93.9 kPa (Section 4.3.1), while the highest SPPA intensity and MI were, respectively, 0.298 W/cm^2 and 0.034 (Section 4.3.4). These exposure values are well within FDA's

regulatory limits for imaging (Duck, 2007). Also, the entire array exhibited a homogeneous surface temperature distribution (Figure 4-11) with an average temperature (30.2 °C ± 0.7 °C) that is well below the IEC requirement of 43 °C after 30 min of continuous imaging (Duck, 2007). These results confirm that the spiral array does not pose acoustic exposure concerns when it operates in unfocused transmission modes.

4.4.2 Summative Interpretation of Findings

Our investigation has generally attested that the density-tapered spiral array can produce unfocused transmissions with the desired field profile characteristics. Specifically, the main beam of the unfocused transmissions had a smooth intensity profile without large fluctuations. Such a smooth beam profile signifies that the propagation of the main wavefront is homogeneous and dispersion is limited. The main beam also had a radially uniform pressure field. One minor irregularity to be noted is that, for diverging waves, the peak of the main wavefront was not laterally centered against the angle steering axis. This issue can be observed in Figure 4-4(k) and (l) that plot the x -axis field intensities at 40 mm depth for steering angles of 0°, 5°, and 10°; for instance, the main peak was not located at the x-axis origin for 0° steering. Such a field characteristic is likely attributed to the sparse positioning of spiral array elements that resulted in the generation of anomalous interference patterns on the main wavefront as it propagates across depth. Nevertheless, it is after all not a serious issue since the main wavefront remained laterally homogeneous with deviations within 3 dB.

From an imaging perspective, the field characteristics generated from the spiral array favor homogeneous insonation of the image volume, which is desirable for volumetric pulse-echo sensing. While secondary lobes are present in the firings due to the $>\lambda/2$ element spacing, their intensity is below the −12 dB threshold relative to the main beam peak in nearly all observed cases. The relatively low secondary lobe intensity is due to the non-gridded element layout of the density tapered spiral array, which prevents strong constructive interference outside of the main beam as is present when regular gridded sparse arrays are used (Yen et al., 2000, Austeng & Holm, 2002).

The secondary lobes from the spiral array are expected to have a limited impact on imaging performance unless steering of more than 10° is applied, which is generally not required for multi-angle Doppler flow estimation (Yiu & Yu, 2016). For instance, as demonstrated in the B-mode images of Figure 4-8 which used −5° to +5° steering, adjacent to the point targets, we did not observe echogenic artifacts that are attributed to secondary lobes. In the B-mode images of Figure 4-9, the average SLLs

were all found to be below −19 dB with only small local regions above −12 dB. For Doppler flow imaging, secondary lobes may lead to errors in the mean Doppler frequency estimation process since these lobes may spatially encompass nearby vessels with flow characteristics different from that in the main sample volume. Nevertheless, with the relatively low SLL magnitudes observed in Figure 4-9, the weighted impact of these secondary lobes on mean Doppler estimation is expected to be limited.

This work, combined with previous works on focused beams (Savoia et al., 2018), demonstrates the promising acoustic field profile performance of the spiral array layout. Although the spiral array's field profile characteristics are less desirable than those for a fully populated 2-D matrix array, the significant reduction in the spiral array's element count is an important factor that favors its integration with ultrasound scanners designed for 2-D imaging. Note that the measured peak pressure value is lower than typical PW transmissions from PZT arrays. Some pressure reduction is to be expected from 2-D arrays due to the lack of elevation focusing, but in this case, the CMUT architecture of the array is also likely a contributing factor. CMUT arrays generally have limited transmission sensitivity. Moreover, the CMUT array used in this study suffered from a high parasitic capacitance introduced by the "dummy" (passive) ASIC used to route the element signals, as described by Savoia et al. (2018), resulting in poor signal strength for the array during imaging. The B-mode images presented in this work show a penetration depth of just 1–2 cm confirming the low signal levels. Increasing the bias voltage of the array elements may enhance the signal strength, but this risks permanent damage to the array elements. Therefore, alternative means of increasing the transmit and receive signals must be investigated (to be discussed in Section 4.4.3).

4.4.3 Limitations and Future Work

Although the density-tapered spiral array has yielded favorable acoustic field patterns for unfocused transmissions, it is subject to some notable limitations that should be addressed. As mentioned in Section 4.4.2, signal strength needs to be enhanced to increase the effective imaging depth when using unfocused transmissions for imaging. On this topic, three directions of investigation are worth pursuing: 1) the design of coded excitation schemes; 2) the development of PZT-based spiral arrays; and 3) the development of CMUT arrays with enhanced interconnection strategies. For the first direction, the CMUT spiral array is an excellent candidate for the implementation of coded excitation imaging schemes due to its wideband nature, which enables the transmission of various codes, including chirps. Recently, chirp transmissions have been shown to increase the Doppler SNR making them a potential

candidate to improve high-volume-rate 3-D imaging (Ramalli et al., 2021). However, when wideband transmissions such as chirps are used for flow estimation, a large estimation variance occurs. Therefore, to implement chirps for dynamic flow imaging, future works should focus on novel methods to reduce the flow estimation variance.

For the second future research direction, the use of a PZT array architecture can effectively reduce the SNR loss related to parasitic capacitance and the transmission sensitivity issue that CMUT arrays are susceptible to. Previous work has shown that a PZT sparse array can produce high-quality diverging wave images (Roux et al., 2018), although a lower transmission frequency of 3 MHz was used, which naturally improves penetration according to ultrasound physics. The main drawback of the PZT architecture is that the arrays are currently limited to gridded layouts making the true density tapered spiral design not possible to exactly replicate (Roux et al., 2017). Thus, there is a tradeoff between the PZT and CMUT versions of the spiral array design where PZT produces higher signal levels in transmit and receive, while CMUT demonstrates an improved secondary lobe performance. The considerations required to assess this tradeoff are nontrivial and will likely necessitate a more direct comparison of the two technologies in the future.

The third research direction on designing CMUT arrays with enhanced interconnection strategies would lower the parasitic capacitance. In turn, these arrays would expectedly reduce the attenuation of the received signals. In addition, the array can be integrated with low-noise amplifiers connected as close as possible to the array elements to minimize the capacitance, such as the alternative version of the array described previously (Savoia et al., 2018).

Besides the need to enhance signal strength, the spiral array's small physical aperture (0.6 cm effective diameter) is another technical limitation to be noted. While it may be tempting to increase the array aperture beyond its current size while maintaining the frequency characteristics of the array, doing so would result in stronger secondary lobes as the sparsity of the element distribution would increase. Lowering the center frequency of the array (thereby increasing λ) could mitigate the increase in secondary lobe level. Nevertheless, such an approach would naturally degrade the spatial resolution.

It is worth noting that such a physical size limitation is not unique to the density-tapered spiral array used in this work, as other 2-D arrays currently under development have similar dimensions [see work by Ramalli et al. (2021)]. Yet, the limited aperture is particularly problematic in unfocused imaging studies where the compounding of multiple transmissions is required to achieve good imaging

performance. Since the aperture is small, the region of overlap between oppositely steered PW transmissions is quite limited, thereby reducing the number of unique transmissions that can be used to resolve a specific region. For example, the B-mode images presented in this work include only −5° to 5° steering since higher degrees of steering for PWs no longer intersect with the point targets as they would with wider aperture arrays. To a certain extent, the use of diverging waves can help to mitigate this issue, but the resulting field pressure magnitude is lower than that of PWs and the penetration depth becomes more limited.

4.5 Conclusion

In the development of 3-D ultrasound systems, spiral arrays with a sparse 2-D aperture have been investigated as a transducer front end that can acquire volumetric data at rates similar to 2-D imaging. However, they have yet to be investigated for their unfocused field properties and potential in high-volume-rate imaging. To fill this knowledge gap, this article has presented a detailed analysis of the unfocused firing characteristics of a density-tapered spiral array and observed smooth wavefront profiles and negligible secondary lobe characteristics. Since the wavefront profile was found to be consistent and predictable, there is little delay difference from a fully populated array making existing beamforming strategies readily portable to this array. This statement is underscored by the good spatial resolution observed in the presented B-mode images formed using delay-and-sum beamforming (even though penetration depth was limited). Sparse arrays, such as the density-tapered spiral array, coupled with unfocused transmissions, provide a viable means of acquiring high-volume-rate 3-D imaging data without the need for a massive system with over 1000 channels of transceiver electronics. With these arrays, high-volume-rate 3-D imaging can potentially be realized on 2-D imaging systems and, in turn, be mobilized for use at a broader scale.

Chapter 5
The Effects of Transmission Scheme on 3D Vector Flow Imaging Performance

5.1 Introduction

Ultrasound 3D vector flow imaging (VFI) enables the estimation of complete hemodynamic profiles as well as volumetric flow rates with high temporal resolution (Wigen et al., 2018). Indeed, ultrasound 3D VFI surpasses the temporal and spatial resolution limits of phase-contrast magnetic resonance imaging (MRI) which is the current gold standard. Yet, ultrasound 3D VFI is not clinically available and there has been little research towards the optimization of 3D VFI techniques. The limited research progress is, in part, a result of the large data rates associated with 3D VFI and high-volume-rate ultrasound in general, particularly with the use of fully addressed matrix arrays. Additionally, challenges with array fabrication and the high-cost of acquiring 3D ultrasound-capable hardware have further limited the extent of research on the topic.

To date, research on ultrasound 3D VFI falls under two broad categories depending on whether: 1) high-performance, large-scale scanners, or 2) low-channel count, benchtop scanners were used. Studies on large-scale scanners typically utilize fully addressed matrix arrays with high SNR to conduct *in vivo* demonstrations of 3D VFI techniques including comparisons with MRI (Correia et al., 2016, Holbek et al., 2017a, Holbek et al., 2017b, Wigen et al., 2018, Correia et al., 2020). Studies on low-channel count scanners or arrays are more limited and, so far, have been restricted to phantom models (Rossi et al., 2020, Holbek et al., 2016). Nevertheless, these past works have focused on demonstrating the feasibility of 3D VFI methodologies rather than optimizing the techniques for flow vector estimation performance. As such, there has been little justification for the algorithmic and imaging parameters. Only one study on 3D VFI has performed a parametric sweep to improve performance (Holbek et al., 2016).

The dependence of vector estimation performance on the number of transmissions and their steering angles is noteworthy. For least-squares 3D VFI, a minimum of 3 unique transmission or reception vectors are required to estimate the flow vectors. However, any number of additional transmits or receives can be added to the least-squares fitting. In 2D VFI, both the number of transmit and receive events as well as their elevation angles have been shown to directly impact the velocity estimation performance (Yiu & Yu, 2016). In 3D VFI, both the number and elevation angles of transmissions and

receptions need to similarly be investigated. Additionally, 3D ultrasound has a second steering angle which rotates the transmissions and/or receptions around the xy-plane called the azimuth angle. This angle is likely to have a strong impact on the flow estimation fidelity in the x- and y-directions.

Here, we present an optimization of the transmission scheme for 3D least-squares VFI using plane waves. The number of unique transmissions, elevation angle, and azimuth angle are all studied for their impact on vector estimation performance. The estimated flow profiles from all parametric combinations are compared to known flow profiles to determine the optimal configuration. The goal of this study is to isolate the effects of steering on the vector estimation performance and thus it is imperative that an array with axis independent steered beam profiles is used. For this reason, the investigation leverages the CMUT density tapered spiral array (Maffett et al., 2022). By determining the effect of transmission schemes on estimation performance, future work on in vitro and in vivo 3D VFI can be designed to produce the highest quality results possible. As such, future works can focus on novel hardware and processing methods to extend the performance and test the limits of ultrasound 3D VFI.

5.2 Methods

3D ultrasound least-squares VFI follows the same overarching principles as 2D least-squares VFI methods (described in detail by Yiu & Yu, (2016)). It is well established that multi-angle Doppler methods can only extract velocity information along the direction of the transmit or receive steering vectors. Thus, in 2D ultrasound, only the x (lateral) and z (depth) components of the velocity can be measured since linear transducer arrays are restricted to steering in the xz-plane. In 3D ultrasound, the use of matrix transducer arrays enables full volumetric steering. This extended steering capability facilitates the extraction of velocity information in the x-, y-, and z-components simultaneously. Naturally, the added dimension increases the complexity of 3D VFI methodologies and computations compared to their 2D VFI counterparts with the distinct advantage of capturing the full flow profile.

5.2.1 3D Multi-Angle Least-Squares VFI Derivation

The goal of 3D VFI is to estimate the 3D velocity vectors at every pixel location in the ultrasound imaging region. In cartesian coordinates, this velocity vector is defined by equation (5.1).

$$\vec{\mathbf{v}} = v_x\hat{\mathbf{x}} + v_y\hat{\mathbf{y}} + v_z\hat{\mathbf{z}} \tag{5.1}$$

As mentioned above, the use of matrix transducer arrays in 3D ultrasound enables 3D steering along the x-, y-, and z-directions in front of the array. The steering vectors in transmission and reception are

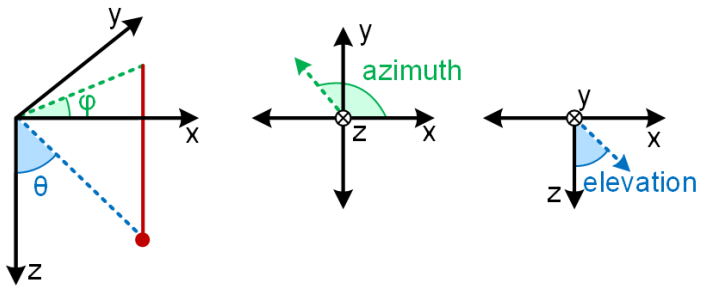


Figure 5-1 Definitions of transmission elevational (θ) and azimuthal (γ) steering angles. The same definitions apply for the receive steering elevation (ϕ) and azimuth (ζ) angles**.**

most succinctly described using their elevational and azimuthal angles. The elevation angle (Tx: θ, Rx: γ) is defined here as the angle from the surface normal of the transducer array (i.e. measured from the z-axis). The azimuth angle (Tx: ϕ, Rx: ζ) is defined as the angle from the positive x-axis of the array towards the positive y-axis rotating around the surface normal. A graphical depiction of these angles is provided in Figure 5-1 for reference. With these two angles, any transmission and reception unit vectors, $\hat{\mathbf{T}}$ and $\hat{\mathbf{R}}$ respectively, can be realized through equations (5.2) and (5.3).

$$\hat{\mathbf{T}} = \sin\theta\cos\phi\,\hat{\mathbf{x}} + \sin\theta\sin\phi\,\hat{\mathbf{y}} + \cos\theta\,\hat{\mathbf{z}} \tag{5.2}$$

$$\hat{\mathbf{R}} = \sin\gamma\cos\zeta\,\hat{\mathbf{x}} + \sin\gamma\sin\zeta\,\hat{\mathbf{y}} + \cos\gamma\,\hat{\mathbf{z}} \tag{5.3}$$

The theoretical observed Doppler frequency, given any pair of transmission and reception vectors and a known transmission frequency, f_{RF}, is dependent on the velocity component along the transmission direction, v_t, and along the reception direction, v_r. This is expressed in an alternate version (compared to equation (2.1)) of the Doppler given by equation (5.4).

$$f_d = \frac{f_{RF}(v_t + v_r)}{c} \tag{5.4}$$

The precise Doppler frequency, f_d, cannot be directly obtained in pulsed Doppler methods. However, the mean Doppler frequency, $\bar{f}_d$, can be found through the commonly used lag-one autocorrelation technique (Kasai et al., 1985).

The velocities v_t and v_r in the Doppler equation (5.4) are projections of the true underlying velocity vector, **v**, onto the transmit and receive unit vectors given by a dot product as in equations (5.5) and (5.6), respectively.

$$v_t = \mathbf{v} \cdot \hat{\mathbf{T}} \tag{5.5}$$

$$v_r = \mathbf{v} \cdot \hat{\mathbf{R}} \tag{5.6}$$

By substituting the expressions for **v**, $\hat{\mathbf{T}}$, and $\hat{\mathbf{R}}$, the expanded relationships between v_t, v_r, and the transmission and reception angles are shown in equations (5.7) and (5.8).

$$v_t = v_x \sin\theta \cos\phi + v_y \sin\theta \sin\phi + v_z \cos\theta \tag{5.7}$$

$$v_r = v_x \sin\gamma \cos\zeta + v_y \sin\gamma \sin\zeta + v_z \cos\gamma \tag{5.8}$$

Rearranging the Doppler equation and subbing in these expanded definitions of v_t and v_r yields:

$$\frac{f_d c}{f_{RF}} = v_x(\sin\theta \cos\phi + \sin\gamma \cos\zeta) + v_y(\sin\theta \sin\phi + \sin\gamma \sin\zeta) + v_z(\cos\theta + \cos\gamma) \tag{5.9}$$

For a scenario with M unique transmission vectors and N unique reception vectors, there will be a total of $M*N$ instances of equation (5.9). This system of equations can be presented in matrix form with the left-hand-side replaced by a placeholder variable, **u**.

$$\mathbf{u} = \mathbf{A}\mathbf{v} \tag{5.10}$$

$$\begin{bmatrix} u_{11} \\ \vdots \\ u_{MN} \end{bmatrix} = \begin{bmatrix} \sin\theta_1 \cos\phi_1 + \sin\gamma_1 \cos\zeta_1 & \sin\theta_1 \sin\phi_1 + \sin\gamma_1 \sin\zeta_1 & \cos\theta_1 + \cos\gamma_1 \\ \vdots & \vdots & \vdots \\ \sin\theta_M \cos\phi_M + \sin\gamma_N \cos\zeta_N & \sin\theta_M \sin\phi_M + \sin\gamma_N \sin\zeta_N & \cos\theta_M + \cos\gamma_N \end{bmatrix} \begin{bmatrix} v_x \\ v_y \\ v_z \end{bmatrix} \tag{5.11}$$

To solve this system of equations, a minimum of three unique transmit-receive pairs are required. These combinations could involve multiple transmission vectors at a single receive vector, a single transmission vector with multiple receive vectors, or any combination of the two. Finally, to solve equation (5.11) with $M*N \geq 3$ independent equations for the components of **v**, the pseudoinverse of **A** as described by Yiu & Yu (2016) and given in equation (5.12) can be used.

$$\mathbf{v} = \begin{bmatrix} v_x \\ v_y \\ v_z \end{bmatrix} = \left(\mathbf{A}^\mathbf{T}\mathbf{A}\right)^{-\mathbf{1}}\mathbf{A}^\mathbf{T}\,\mathbf{u} \tag{5.12}$$

It is critical to note that additional transmissions reduce the effective frame rate for each transmission direction. For an ultrasound system with a pulse repetition frequency of f_{PRF}, the effective frame rate with multi-angle transmissions is given by equation (5.13).

$$f_{DAQ} = \frac{f_{PRF}}{M} \tag{5.13}$$

This reduction in frame rate in turn reduces the maximum velocity estimation limit in the lag-one autocorrelator.

5.2.2 Imaging Methods

This work was performed on a CMUT density tapered spiral array (Ramalli et al., 2015, Savoia et al., 2018) driven by an ULA-OP 256 research ultrasound scanner (Boni et al., 2016). The CMUT spiral array was used because it is the only realization of the original spiral array design that preserves the non-gridded layout of the elements. As such, this array has modest secondary lobe levels as well as a radially uniform beam profile (Maffett et al., 2022). Unlike row-column-addressed arrays, sparse arrays can be steered at any azimuth angle enabling the investigation of the full 3D steering space. The CMUT array was biased at 75V and driven with a 20V working voltage.

Plane wave transmissions (7.5MHz center frequency, 5-pulse cycle, 10% Tukey windowed) at 3 elevation angles and 18 azimuth angles were examined. A complete list of the transmission angles can be found in Table 5-1. Receive steering was not investigated in this work due to the small size and density tapering of the spiral array aperture. Indeed, even small receive elevational steering results in the aperture being shifted towards the highly sparse edges of the array yielding poor signal quality.

RF data acquired on the scanner was saved to an external computer for offline processing. The RF data was band-pass filtered (FIR; passband: 6.5-8.5MHz) and then beamformed using a GPU-beamformer modified for 3D ultrasound imaging with a non-gridded array (Yiu et al., 2011). All beamformed datasets were clutter filtered [FIR; cutoff: 12Hz (straight tube), 8Hz (helix), 42Hz (aneurysm)] and passed through a lag-one autocorrelator to estimate the mean Doppler frequency (ensemble length: 100 frames). Then, sets of mean Doppler frequency estimations at varying transmission angles were processed through a 3D VFI estimator following the derivation in the previous section. The number of transmission angles used in the estimator, M, the elevational steering, θ, and

Table 5-1 List of elevation and azimuth angles used in 3D VFI optimization.

Elevation Angles (°)	Azimuth Angles (°)
5, 7.5, 10	0, 15, 30, 45, 60, 75, 90, 105, 120, 135, 150, 180, 210, 225, 240, 270, 300, 315

Table 5-2 Transmit azimuth angle steering combinations used for 3D VFI. All combinations were used with 5, 7.5, and 10° elevation steering. Colors indicate azimuth angle spacing.

Azimuth Angle Span	Number of Transmission Angles								
		3	4	5	6	7	8	9	10
	30	0, 15, 30							
	45		0, 15, 30, 45						
	60	0, 30, 60		0, 15, 30, 45, 60					
	75				0, 15, 30, 45, 60, 75				
	90	0, 45, 90	0, 30, 60, 90			0, 15, 30, 45, 60, 75, 90			
	105						0, 15, 30, 45, 60, 75, 90, 105		
	120	0, 60, 120		0, 30, 60, 90, 120				0, 15, 30, 45, 60, 75, 90, 105, 120	
	135		0, 45, 90, 135						0, 15, 30, 45, 60, 75, 90, 105, 120, 135
	150	0, 75, 150			0, 30, 60, 90, 120, 150				
	180	0, 90, 180	0, 60, 120, 180	0, 45, 90, 135, 180		0, 30, 60, 90, 120, 150, 180			
	210	0, 105, 210					0, 30, 60, 90, 120, 150, 180, 210		
	225		0, 75, 150, 225		0, 45, 90, 135, 180, 225				
	240	0, 120, 240		0, 60, 120, 180, 240				0, 30, 60, 90, 120, 150, 180, 210, 240	
	270	0, 135, 270	0, 90, 180, 270			0, 45, 90, 135, 180, 225, 270			0, 30, 60, 90, 120, 150, 180, 210, 240, 270
	300	0, 150, 300		0, 75, 150, 225, 300	0, 60, 120, 180, 240, 300				
	315		0, 105, 210, 315				0, 45, 90, 135, 180, 225, 270, 315		

the azimuth steering, ϕ, were varied to produce different velocity estimates. Table 5-2 shows all transmission combinations used to derive the 3D flow vectors.

5.2.3 Experimental Methods

To investigate the performance of 3D VFI and the dependence on the transmission scheme, three experimental testbeds were leveraged: 1) constant flow in a straight tube, 2) constant flow in a helical

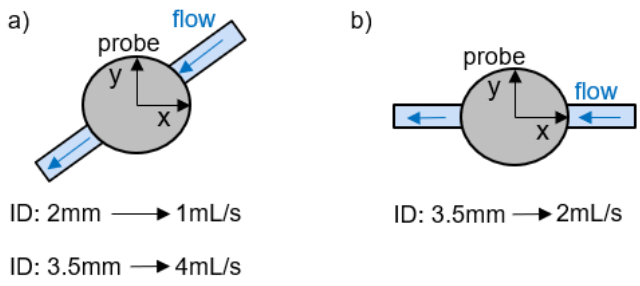


Figure 5-2 Relative probe-flow orientations in straight tube experiments.

vessel, and 3) pulsatile flow in a cerebral aneurysm model. The straight tube experiment is leveraged for a detailed parametric sweep of the transmission scheme to assess the error of the estimated velocities on a simple flow scenario. The helical flow experiment enables the validation of flow estimation accuracy on multi-directional flow. The aneurysm phantom demonstrates the performance and resulting utility of optimized 3D VFI for mapping highly complex and dynamic flows.

Given the limited SNR and penetration of unfocused transmission with the density tapered spiral array (Maffett et al., 2022), all experiments leveraged microbubble contrast agents (Definity-like microbubbles) to capture the flow signal. Prior to each acquisition, a 150μL bolus of contrast (10^9MB/mL) diluted at a concentration of 15% v/v was injected into the Orgasol-based blood mimicking fluid (BMF) upstream from the imaging region. A toroidal vessel (Chee et al., 2021) was placed in the flow circuit between the contrast injection port and the phantoms to ensure the contrast was uniformly dispersed across the vessels.

5.2.3.1 Straight Tube Experiments

Walled poly-vinyl alcohol (PVA) phantoms with inner diameters (ID) of 3.5 and 2 mm were imaged in water. The phantoms were fabricated with a previously described protocol (Chee et al., 2016). The inlet of the phantoms was connected to a 1m-long rigid tube to ensure the flow entering the phantoms was laminar. Flow in the straight tubes was produced using a programmable flow pump (Ho et al., 2017). In the 2mm ID phantom a flow rate of 1mL/s was used, and the vessel was aligned approximately 45° from the x- and y-axes [Figure 5-2(a)]. In the 3.5mm ID phantom flow rates of 2 and 4mL/s were used. In the scenario with 4mL/s flow, the vessel was aligned again at 45° from the x- and y-axes [Figure 5-2(a)]. For the 2mL/s flow, the vessel was aligned parallel to the x-axis to test the performance at a different lateral flow direction [Figure 5-2(b)].

3D VFI estimations were performed with every transmission combination provided in Table 5-2 for all three straight tube flow scenarios. All transmissions studied were acquired in batches of four angles at a PRF of 10kHz resulting in an effective PRF, f_{DAQ}, of 2.5kHz for all angles. Therefore, the performance results do not account for the velocity estimation limit changes that occur when additional angles are added but the system PRF is maintained. The performance of the 3D VFI estimations were compared to the ideal parabolic flow over cross-sections of the vessel. The maximum flow velocity in the ideal parabolic profile was measured using the Doppler spectrogram from a clinical ultrasound scanner (GE Venue Go, GE Healthcare, Chicago, IL, USA) with an L4-12t probe (GE Healthcare) and a 60° beam-flow angle to minimize the angle dependence.

5.2.3.2 Helix Phantom Experiments

The helix phantom was developed to validate the multi-directional estimation performance of the optimal 3D VFI scheme assessed from the parametric sweeps on the straight tube phantoms. The helical vessel (Figure 5-3) was designed to have a 2.5mm ID with a 6mm rotational diameter over four rotations. The phantom was fabricated using a lost-core technique (Ho et al., 2017) from a propylene glycol-PVA mixture with low attenuation (attenuation coefficient: 0.18dB/cm·MHz). The phantom underwent two 24-hour freeze-thaw cycles prior to removing the vessel core. Post-fabrication, the

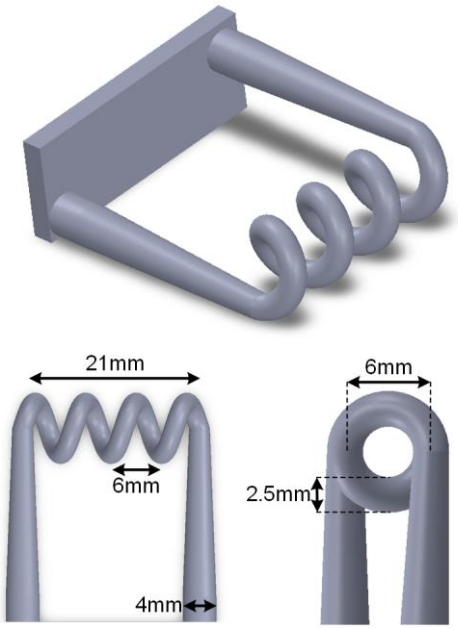


Figure 5-3 Lumen geometry of the helix phantom.

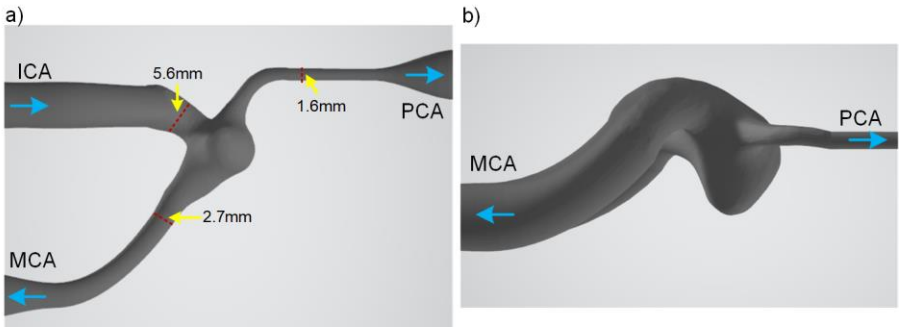


Figure 5-4 (a) Top view and (b) side view of the aneurysm phantom lumen.

lumen ID was measured to be 3.5mm due to contraction of the PVA mixture during the freeze-thaw cycling. A constant flow rate of 1mL/s was used.

The 3D VFI flow profile was compared to computational fluid dynamics (CFD) simulations performed in SolidWorks (Dassault Systemes, Waltham, MA, USA). In the CFD model, the lumen size was expanded to 3.5mm to match the dimensions of the physical phantom. The inlet boundary condition was set to a uniform 1mL/s volumetric flow rate and the outlet was set to atmospheric pressure. A no slip boundary condition was used on all vessel walls.

5.2.3.3 Aneurysm Phantom Experiments

The cerebral aneurysm model is based on CT-scans of a 60-year-old patient (Ho et al., 2017) (see Figure 5-4 for the model geometry). The aneurysm phantom was fabricated in an identical manner to the helix phantom. The internal carotid artery (ICA) inlet of the phantom was connected to the output of the flow pump through the laminar mixer. The posterior communicating artery (PCA) and middle cerebral artery (MCA) outlets of the phantom were routed to 10cm of 2mm ID flow resistors and then rejoined and returned to the pump reservoir. The flow resistors are intended to mimic the downstream flow resistance encountered in the cerebral vasculature (Ho et al., 2017). The pump was set to output a carotid flow profile with a peak systolic flow rate of 3.5mL/s.

5.3 Results

5.3.1 Azimuth Angle Span is the Strongest Factor in 3D VFI Performance

Figure 5-5 shows flow magnitude surface plots and flow vector plots for all straight tube flow conditions with 6 transmissions and 5° elevational steering. Figure 5-5(a)-(d) use an azimuth angle span

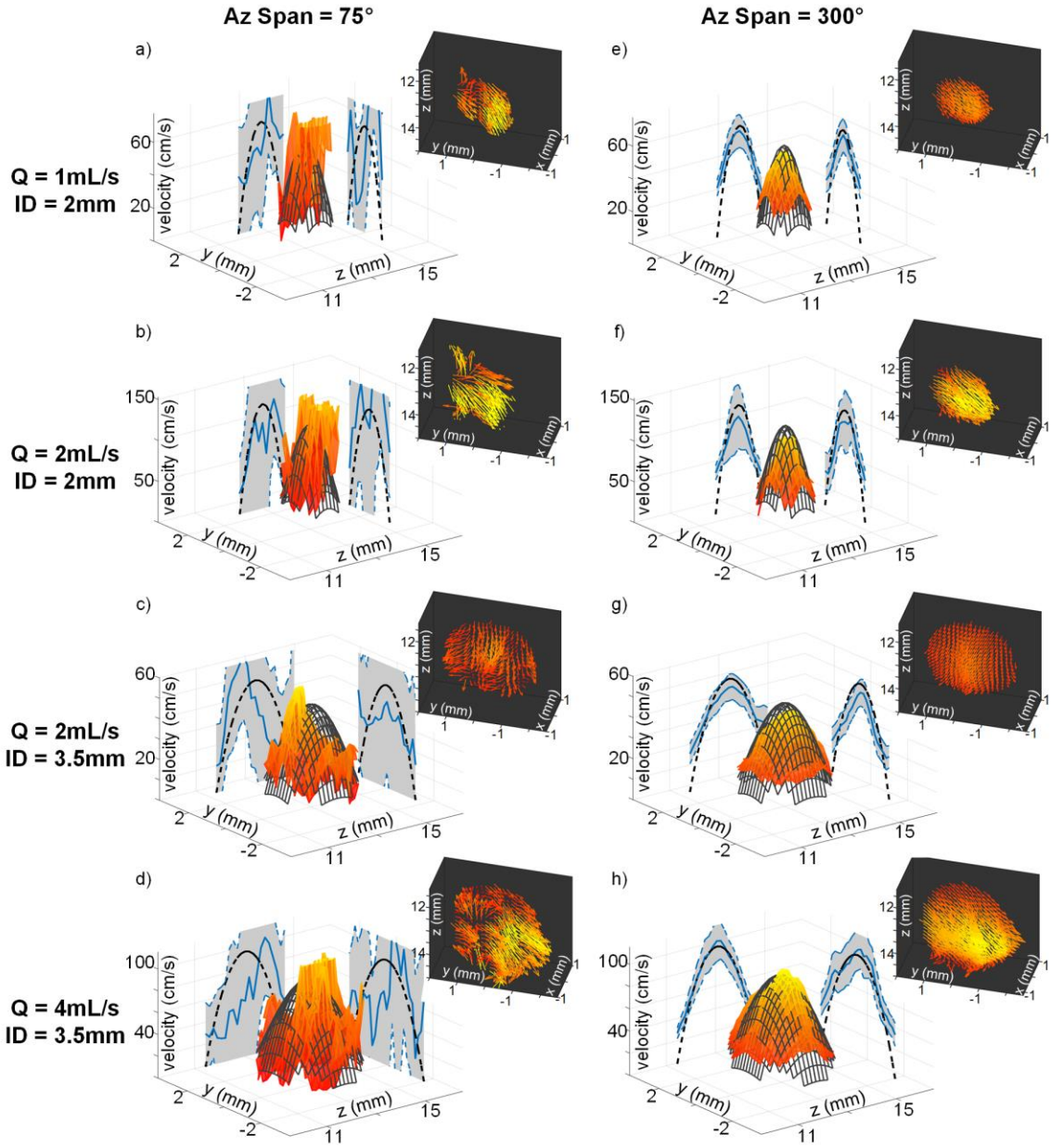


Figure 5-5 Flow magnitude surface plots for 6 transmission angles with 5° elevational steering and (a)-(d) 75° and (e)-(h) 300° azimuthal steering. The ideal parabolic profile is shown as the mesh. The centerline ideal and estimated profiles are projected on the velocity axes (dashed black line – ideal, solid blue line – estimated, dashed blue line – ±1SD). Small insets show the flow vectors at the same cross-section.

of 75° whereas Figure 5-5(e)-(h) use an azimuth span of 300°. The centerline cross-sections along the y- and z-axes are plotted in each surface plot with the ideal parabolic profile. From Figure 5-5(a)-(d) it can be observed that the 75° azimuth span results in uneven velocity magnitudes across the vessel with many sharp peaks of overestimation and high standard deviations (in the cross-sectional profiles). The vector plots in Figure 5-5(a)-(d) highlight the non-uniformity of the estimation with many vectors out of alignment with the expected flow direction. In Figure 5-5(e)-(h), the velocity magnitudes are much smoother in every flow condition. The cross-sectional profiles show smaller standard deviations and reasonable alignment with the expected parabolic profiles. The vector plots in Figure 5-5(e)-(h) have largely aligned vectors in the expected flow direction with the exception of some vectors near the vessel edges.

Figure 5-6 shows the same flow magnitude and vector plots with 6 transmissions and an azimuth span of 300°. Figure 5-6(a)-(d) use 7.5° elevational steering and Figure 5-6(e)-(h) use 10° elevational steering. In general, the performance of the flow estimation is degraded with the increase in elevational steering. 10° elevational steering results in an underestimation of the peak flows in the parabolic profiles and an increase in estimation variance. Considering Figure 5-5(e)-(h), which uses the same number of transmissions and azimuth span but with 5° elevation, it can be observed that the lowest elevational steering results in the closest matching estimations to the ideal flow profiles.

Figure 5-7 again shows the flow magnitude and vector plots but in this case with varying transmission numbers, a constant azimuth span of 240°, and elevational steering of 5°. Figure 5-7(a)-(d) use 3 transmissions for the flow vector calculations and Figure 5-7 (e)-(h) use 9 transmissions. The magnitude of the flow estimates closely follow the expected parabolic profiles in all cases with both numbers of transmissions. Generally, the 9 transmission cases have smoother profiles (particularly on the y-axis centerline cross-sections), lower standard deviations, and better vector alignments.

Figure 5-8(a)-(c) includes error plots for the 2mL/s, 2mm-diameter flow condition (this condition has the maximum peak velocity of all tested cases) and all transmission combinations at 5°, 7.5°, and 10° elevational steering, respectively. In these plots, it can be seen that the estimation error is strongly dependent on the azimuth angle span, with low angle spans (e.g. <150°) having much higher error than larger spans. This observation is in agreement with the results shown in Figure 5-5. It is also apparent that the number of transmissions has a smaller impact on the velocity estimation error than the azimuth span, which matches the results in Figure 5-7 where subtle differences were observed between 3 and 9

transmissions. The error magnitude at all transmission combinations is the highest with 10° elevational steering and the lowest with 5° steering as confirmed in Figure 5-5(e)-(h) and in Figure 5-6. Figure 5-8 (d)-(f) shows the same results for the 2mL/s, 3.5mm-diameter flow condition (this condition has the minimum peak velocity of all tested cases). Generally, the results are in close agreement between the

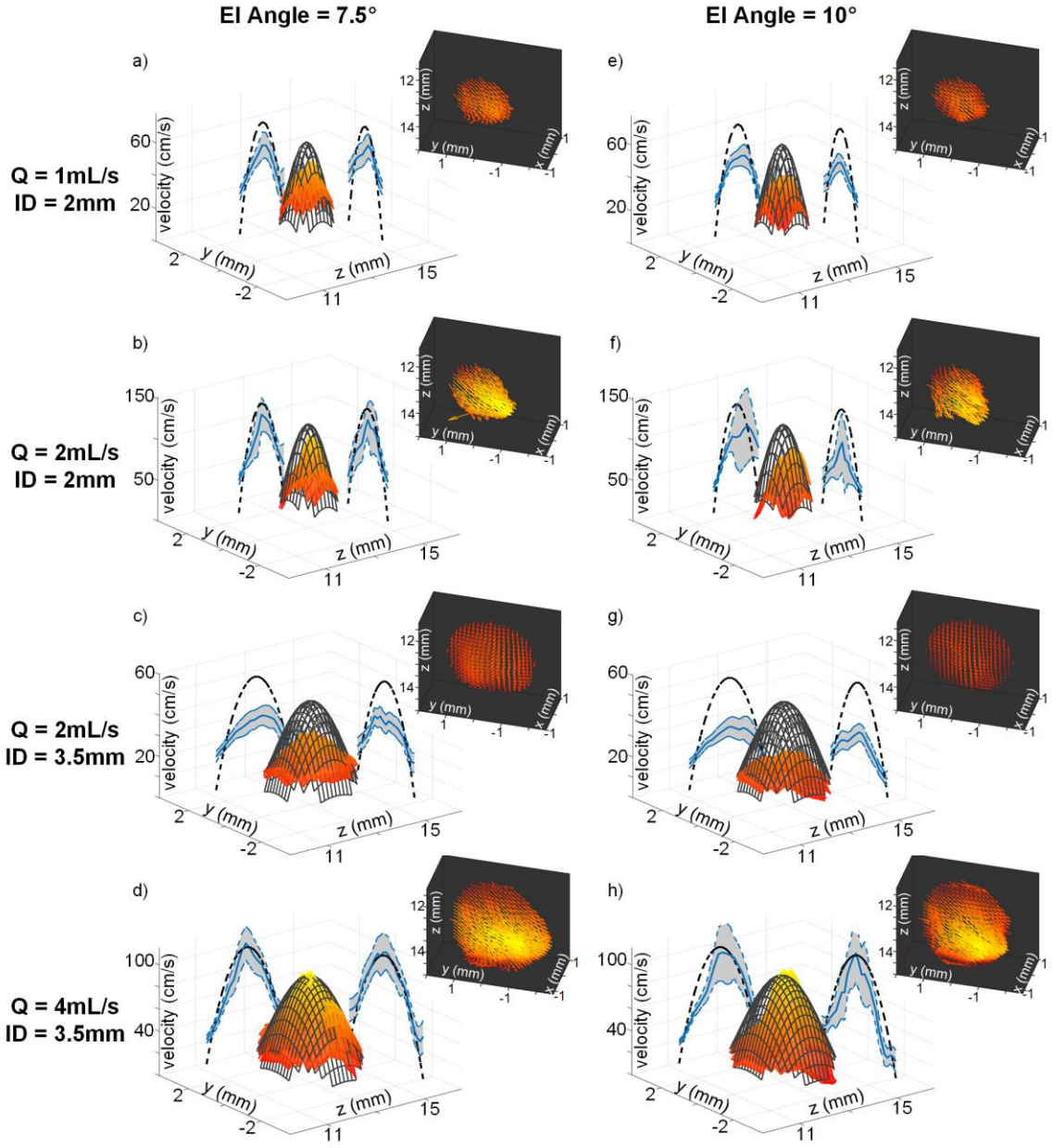


Figure 5-6 Flow magnitude surface plots for 6 transmission angles with 300° azimuthal steering and (a)-(d) 7.5° and (e)-(h) 10° elevational steering.

two flow conditions. A complete table of the RMSE values for all flow conditions and transmission combinations can be found in Appendix B.

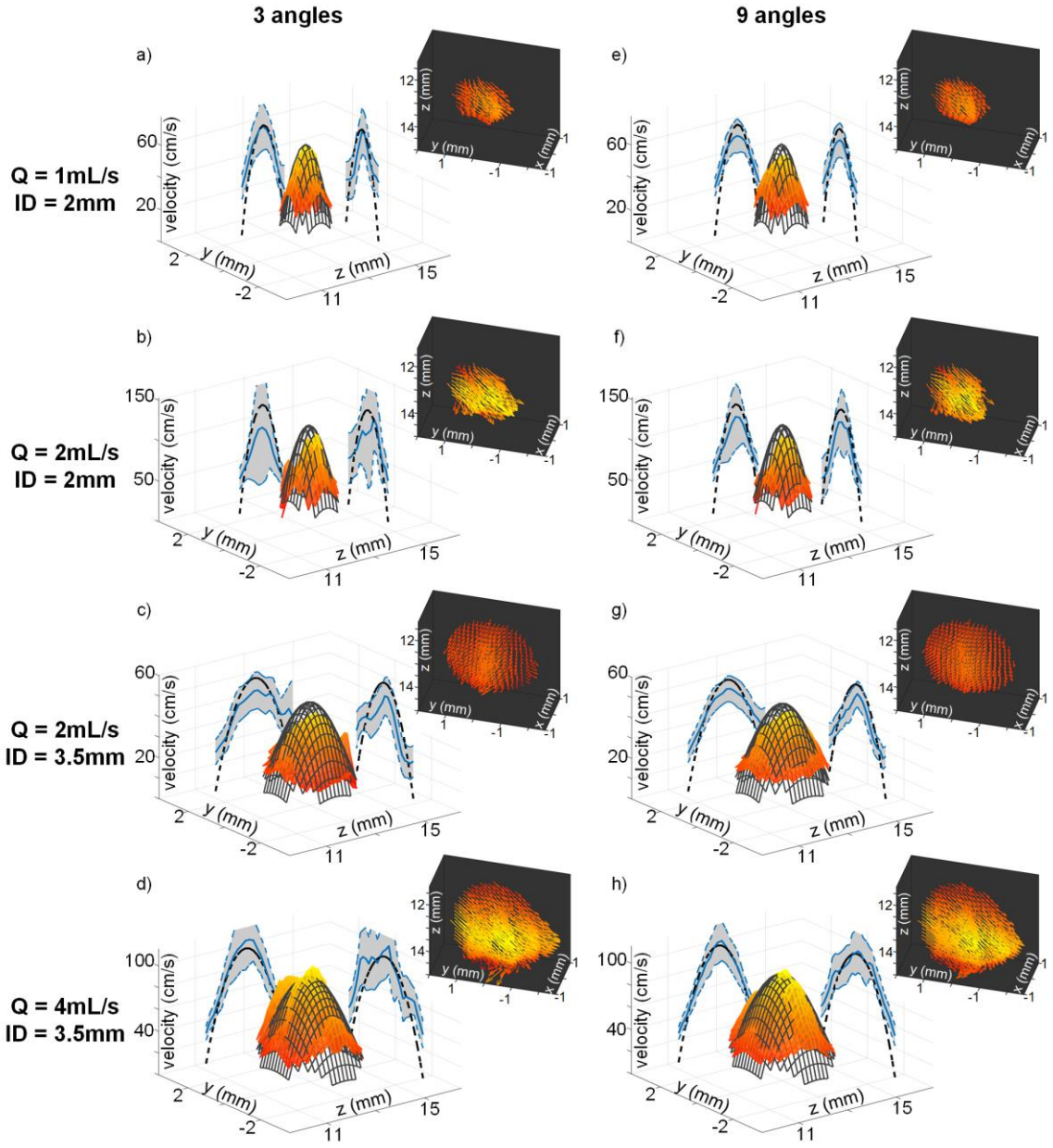


Figure 5-7 Flow magnitude surface plots for 5° elevational steering and 300° azimuthal steering with (a)-(d) 3 and (e)-(h) 9 transmission angles.

5.3.2 Axial Flow is the Most Accurately Estimated in Multi-Directional Flow Profiles

Given the results of the parametric sweep in Section 5.3.1, a transmission scheme with low elevational steering (5°), a wide azimuth angle span (300° span), and a mid-range number of transmissions (6 transmissions) was selected. The vector flow profiles for the helix phantom are analyzed on three planes of interest [Figure 5-9(d)]: one plane with upward flow (negative z-direction), one plane with downward flow (positive z-direction), and one plane with lateral flow (negative y-direction). The upward and downward slices are placed at the midpoint of the phantom depth. The lateral slice is on

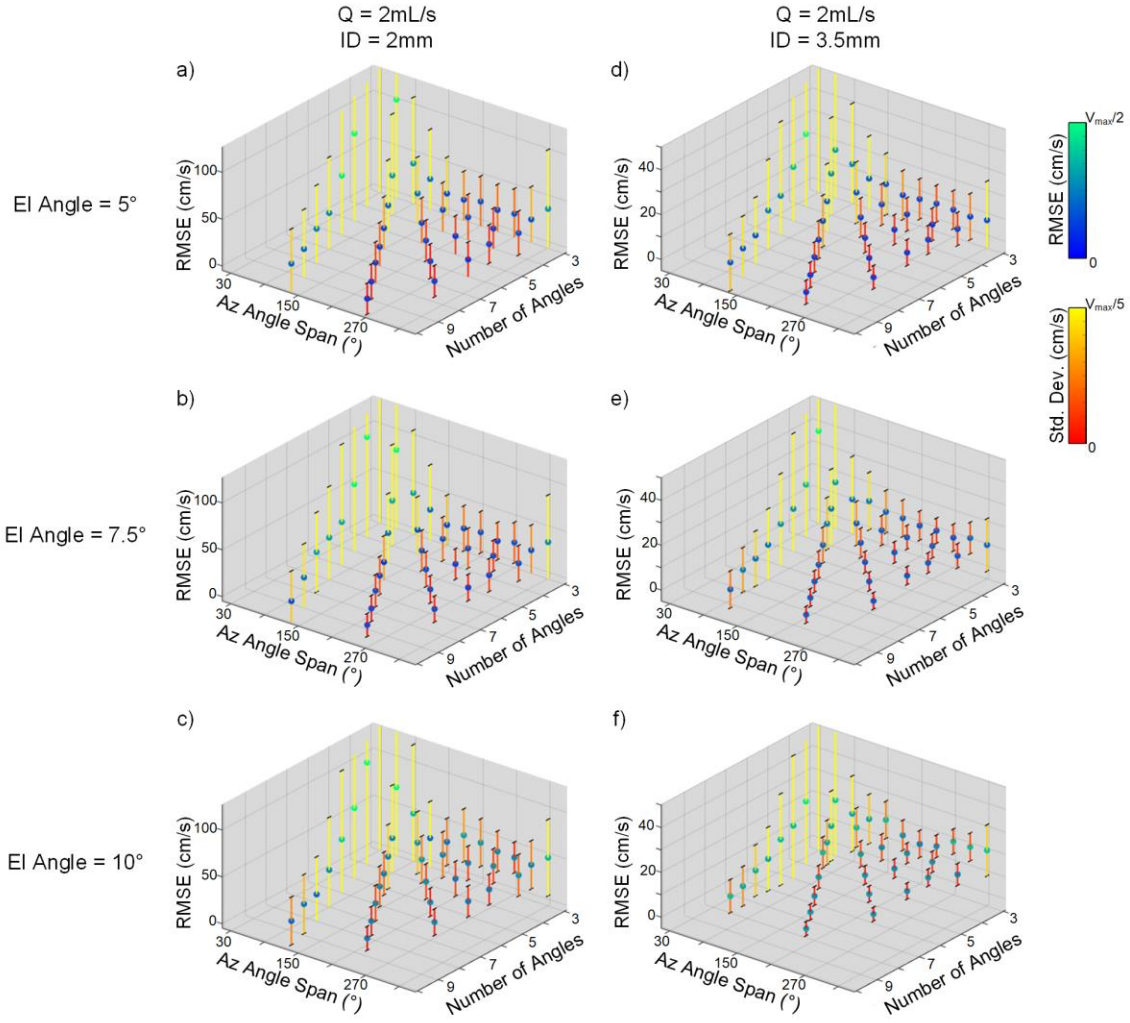


Figure 5-8 RMSE plots for all tested transmission combinations for (a)-(c) 2mL/s flow in a 2mm ID vessel with 5, 7.5, and 10° elevational steering, respectively. (d)-(f) RMSE plots for 2mL/s flow in a 3.5mm ID vessel at the same elevation angles, respectively.

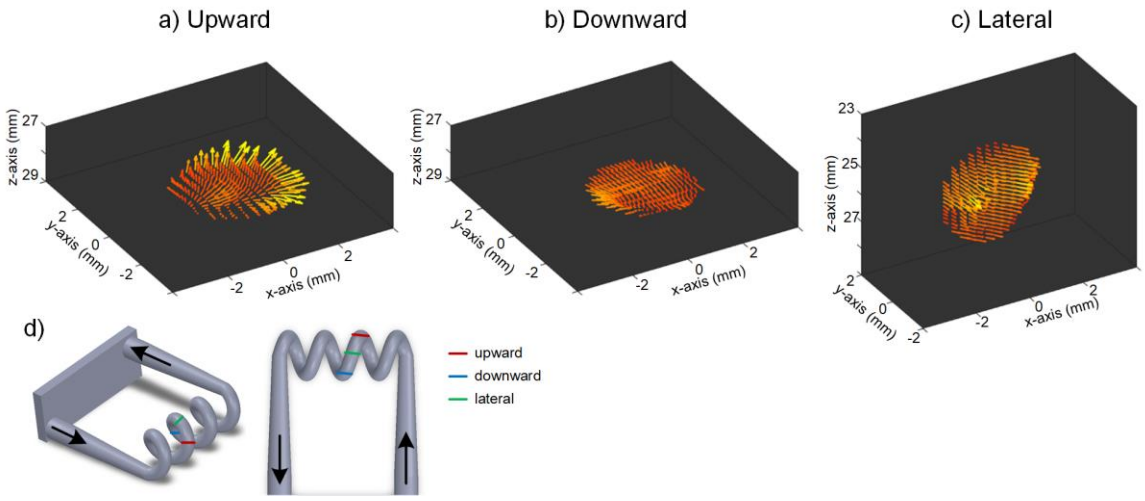


Figure 5-9 Velocity vectors planes from the helix phantom measured by 3D VFI. (a) Upward flow slice, (b) downward flow slice, (c) lateral flow slice, and (d) approximate locations of the slices in the helix phantom.

the shallowest portion of the helix. Figure 5-9(a)-(c) shows the vector plots for each of the planes of interest respectively. In Figure 5-9(a) the vectors near the vessel center have the expected upward flow component with a strong lateral component in the positive x-direction. The edges of the vessel have very strong lateral flow that does not match the expected profile. In Figure 5-9(b) the vectors are aligned downward, as expected, with a smaller lateral component than in Figure 5-9(a). Lastly, Figure 5-9(c) has flow vectors oriented towards the negative y-direction but with generally larger magnitudes than in Figure 5-9(a) and (b).

The flow vector components measured with 3D VFI are compared to the CFD flow components in Figure 5-10. Figure 5-10(a) contains the upward flow slice with subplots (i)-(iii) are the ultrasound measured components and (iv)-(vi) are the CFD components. Of all components, the z-direction flow is the closest match between ultrasound and CFD. In the z-component ultrasound map, the magnitude of the flow is notably less than in CFD, however, the shape of the profile is similar. Conversely, the x- and y-components show significant deviation between the ultrasound and CFD. Figure 5-10(b) contains the same plots for the downward flow slice. Again, the z-component has the most resemblance between ultrasound and CFD, whereas the x- and y-components have large differences. Figure 5-10(c) shows the ultrasound and CFD results for the lateral flow slice. As in the previous slices the z-component is in reasonable agreement between ultrasound and CFD. For the y-component, the ultrasound measurement exceeds the maximum velocity range of the plot and reaches ~20cm/s indicating a

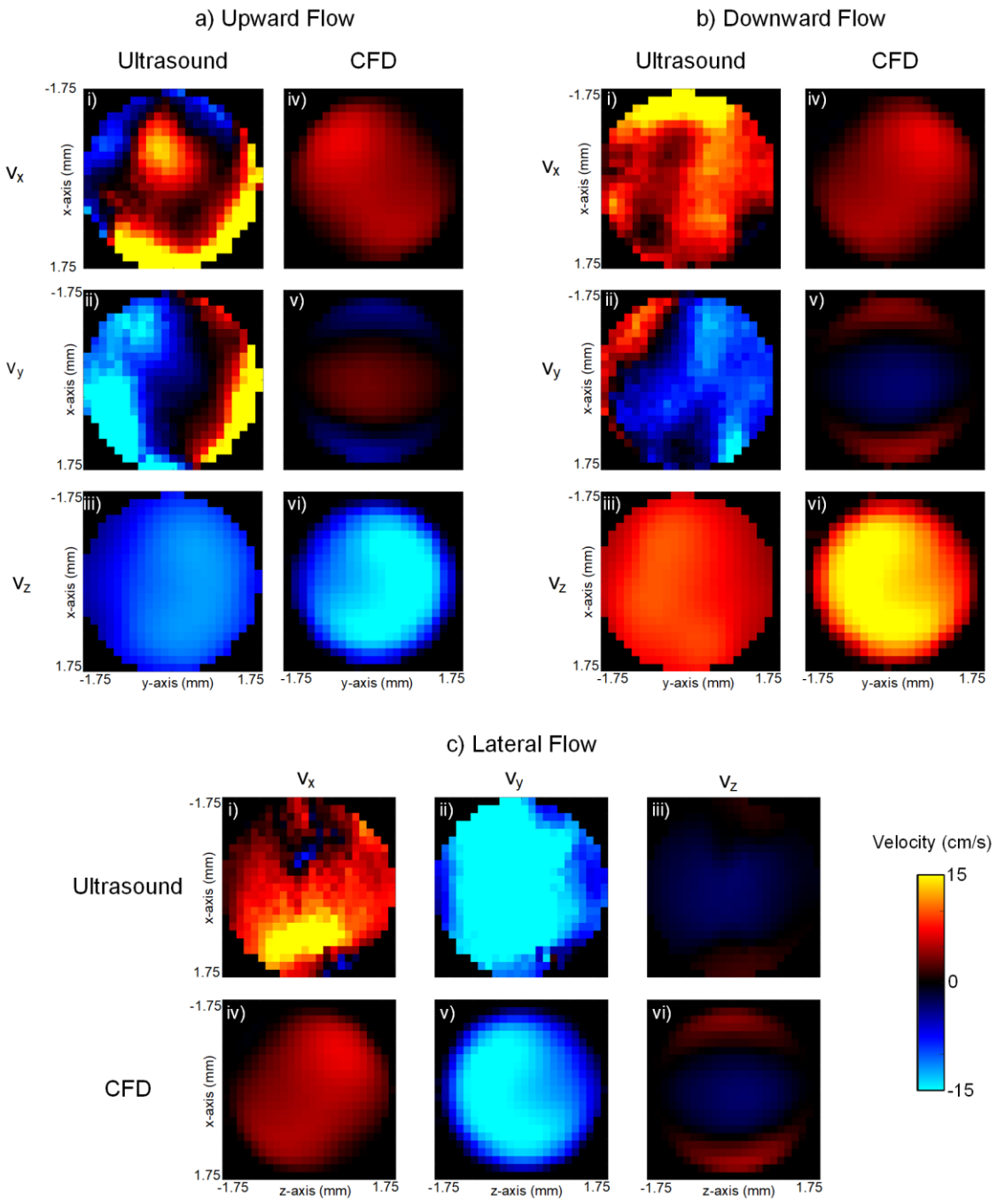


Figure 5-10 Ultrasound measured and CFD flow vector components on three slices of the helix phantom. (a) Upward slice where (i)-(iii) are the x, y, and z-components of the ultrasound measured flow vectors and (iv)-(vi) are the x, y, and z-components of the CFD flow vectors. (b) Downward slice where (i)-(iii) are the ultrasound components and (iv)-(vi) are the CFD components. (c) Lateral slice where (i)-(iii) are the ultrasound components and (iv)-(vi) are the CFD components.

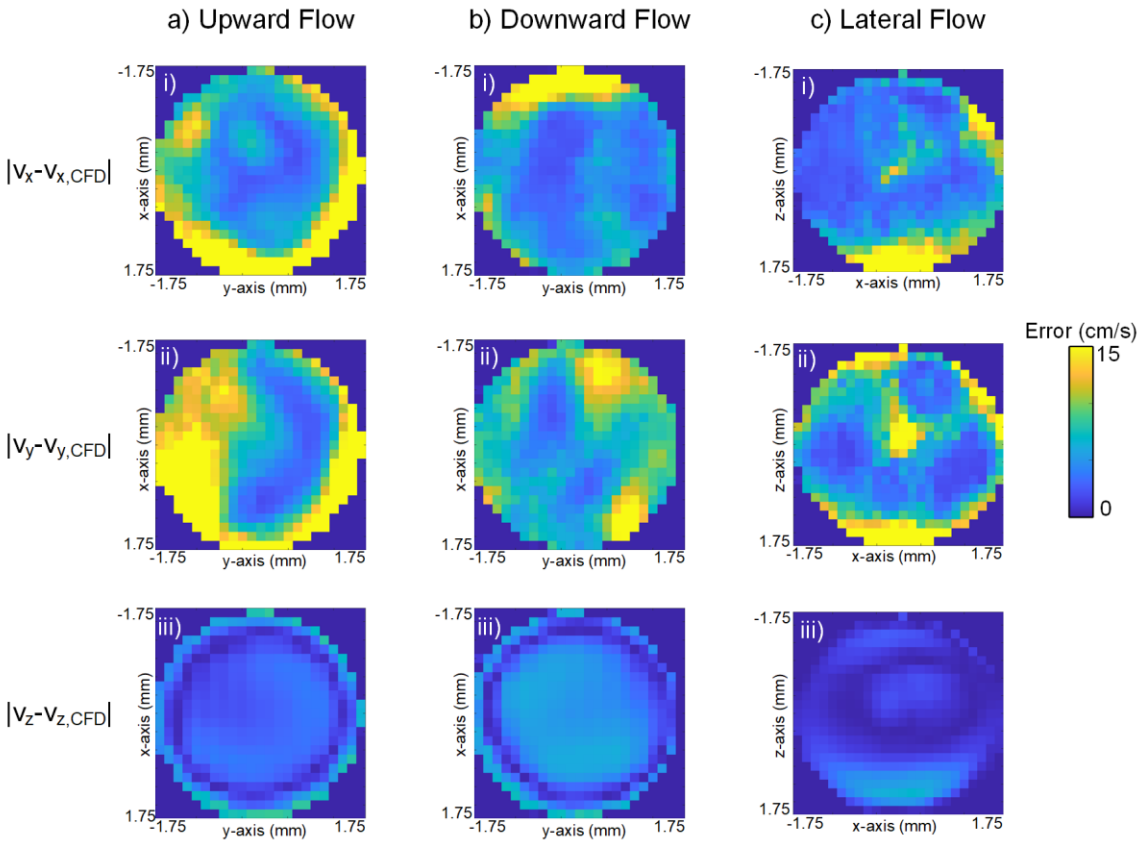


Figure 5-11 Error magnitude of measured velocity vectors compared to CFD for each flow vector component on the (a) upward slice, (b) downward slice, and (c) lateral slice of the helix phantom. Sub-plots (i)-(iii) are the errors of the x, y, z-components of the velocity, respectively.

significant overestimation of the flow velocity compared to CFD. In nearly all slices and components, the magnitude of the flow at the edge of the vessel is higher in ultrasound than in CFD.

Figure 5-11(a)-(c) plots the magnitude of the difference between the ultrasound and CFD flow components for the upward, downward, and lateral slices, respectively. As expected from Figure 5-10, all slices have the largest deviations in the x- and y-components of the flow. In most cases, the highest error in the x- and y-components is located at the edge of the vessel however Figure 5-11(c)(ii) also has high error at the center. The particularly large edge error regions in Figure 5-11(a)(i)-(ii) correspond to the high lateral flow velocities observed in the vector plot in Figure 5-9(a). The high central error in Figure 5-11(c)(ii) corresponds to the relatively high vector magnitude in the vector plot in Figure 5-9(c). Table 5-3 lists the RMSE values for all flow components compared to CFD at each of the three

Table 5-3 Directional error on each of the helix phantom slices.

Slice	RMSE x (cm/s)	RMSE y (cm/s)	RMSE z (cm/s)
Upward	15.7±3.7	16.6±3.4	3.6±0.1
Downward	8.4±1.4	9.3±1.0	4.4±0.1
Lateral	7.5±0.5	8.9±0.8	1.9±0.1

slices. The RMSE values highlight the relatively accurate estimates of the z-flow component. As well it should be noted that the lateral slice had the most accurate estimates of the lateral flow components.

5.3.3 3D VFI Maps Complex and Dynamic Flows

The same transmission scheme from the helix phantom study was employed in the study of the aneurysm phantom (i.e. elevation: 5°, azimuth: 0, 60, 120, 180, 240, 300°). Movie 5-1(a)-(b) show the vector flow maps for the inlet and outlet slices of the aneurysm phantom through the cardiac cycle. The inlet slice (Movie 5-1(a)) shows a flow jet on the right side of the slice (opposite the inlet vessel) prior to systole and subsequently a flow jet on the left side of the slice from the inlet vessel at systole. Figure 5-12(a) shows a snapshot of Movie 5-1(a) at peak systole where the flow jet from the inlet is visible on the left side of the slice. This snapshot also shows the flow circulation in the aneurysm bulb. The outlet slice (Movie 5-1(b)) indicates that a small flow jet towards the PCA outlet vessel forms prior to systole. Figure 5-12(b) shows a snapshot of Movie 5-1(b) just before peak systole while the flow jet towards the PCA outlet is present. The traces in Figure 5-12(a)(ii) and (b)(ii)-(iii) show the magnitude of the flow velocity near the ICA inlet, PCA outlet, and MCA outlet respectively. On the trace in Figure 5-12(b)(ii), the first peak corresponds to the flow jet towards the PCA outlet. Shortly afterwards, as can be seen in Movie 5-1(b), the flow near the PCA outlet changes direction and another flow jet forms at systole which corresponds to the second peak in the trace. The MCA outlet (on the left side of the slice) has more consistent flow towards the outlet across the cardiac cycle. Figure 5-12(b) also highlights some of the flow separation that occurs on the outlet slice because of the bifurcation of the ICA into the PCA and MCA.

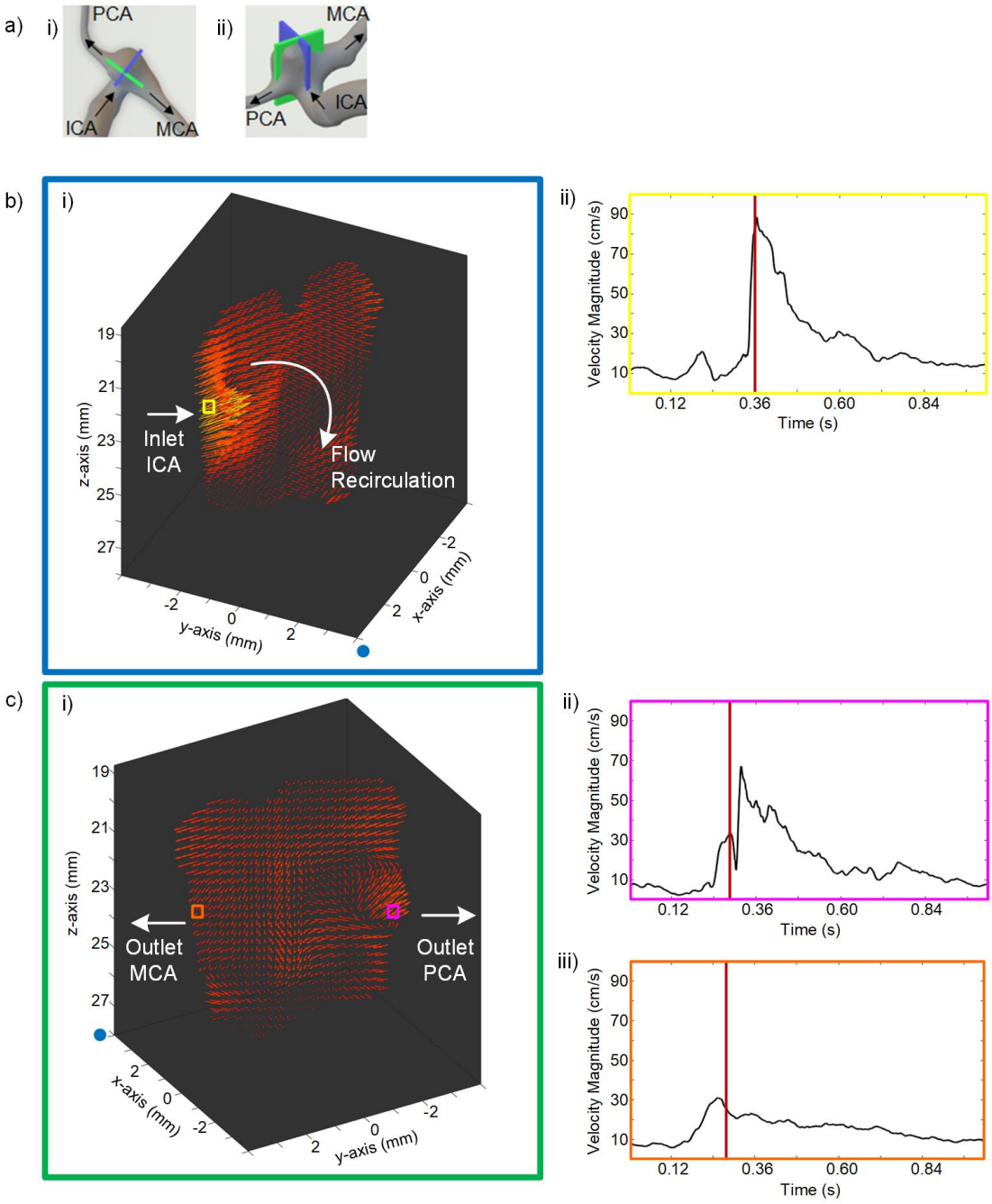


Figure 5-12 Still frames from the dynamic vector flow in the aneurysm phantom (Movie 5-1). (a) Location of the imaging planes within the phantom: blue is the inlet plane and green is the outlet plane. (b) (i) vector profile of the inlet jet and flow recirculation at peak systole, (ii) velocity magnitude profile where the red line indicates the time of the still frame. (c) (i) vector profile of the outlet PCA jet and constant outlet MCA flow, (ii) flow magnitude profile at the PCA outlet (note that the second peak in the magnitude is the flow direction reversal seen in Movie 5-1), (iii) flow magnitude profile at the MCA outlet.

5.4 Discussion

5.4.1 Statement of Contributions

This study presents a rigorous parametric analysis of transmission schemes for 3D least-squares VFI with the objective of optimizing flow velocity estimation accuracy. While several existing works have demonstrated the feasibility and utility of 3D VFI both in vitro (Holbek et al., 2016, Rossi et al., 2020) and in vivo (Wigen et al., 2018, Holbek et al., 2017a, Holbek et al., 2017b, Correia et al., 2016, Correia et al., 2020), there has been little justification for the choice of transmission scheme. The ad hoc selection of the number of transmissions and their angles may result in poorly tuned schemes which limit velocity estimation performance. Optimizing the transmission scheme may enable the use of fewer overall transmissions providing potential gains in the achievable velocity estimation range while simultaneously increasing the estimation fidelity. The results and analysis presented in this work are intended to serve as a reference for future 3D VFI developments and are expected to expedite the application of 3D VFI tools to clinically relevant scenarios.

The parametric sweep presented here studies the effects of azimuthal steering, elevational steering, and the number of transmissions on the velocity estimation accuracy. Figure 5-8 provides an overview of the error trends with respect to each of these three independent variables for the steepest (Figure 5-8(a)) and most gradual (Figure 5-8(b)) flow profiles studied. From Figure 5-8 it is clear that the azimuthal steering has the greatest impact on the flow estimation accuracy (see Figure 5-5 for a qualitative comparison) where larger azimuth angle spans result in lower velocity estimation error. Figure 5-8 also shows that the elevational steering is the second strongest factor in velocity estimation error (see Figure 5-6 for a qualitative comparison) with elevational steering of 5 producing the most accurate estimates. The least impactful variable is the number of transmissions which is observed to cause a subtle error and variance reduction for increased number of transmissions in both Figure 5-8 and Figure 5-7. Thus, an optimized transmission scheme for 3D least-squares VFI utilizes the full 360° range of azimuthal steering, has low elevational steering, and includes as many transmissions as is permissible considering the required velocity estimation limit.

Given the results of the parametric sweep, a transmission scheme was selected to test on multi-directional and dynamic flows in the helix and aneurysm phantoms respectively. This transmission scheme included six transmissions (effective PRF of 1.67kHz) with 5° elevational steering to maximize the imaging depth. An azimuth span of 300° is used which uniformly covers the entire 360° azimuth

steering range (60° spacing). Figure 5-11 shows the error of the flow component estimations across three slices of the helix phantom compared to CFD. In contrast to the straight tube results, velocity estimations on the helix phantom have relatively high errors in the x- and y-components of the flow velocity; however, the maximum flow velocity in the helix phantom is just 16.5cm/s which is notably lower than what was used in the straight tubes and may contribute to the discrepancy. The z-component of the velocity is accurately estimated. Furthermore, Movie 5-1 shows the dynamic flow mapping capabilities of 3D VFI on the aneurysm model. The flow profile near the inlet of the aneurysm closely matches that of the pump output providing an indication that the velocities are being reasonably well estimated. On both the inlet and outlet planes in Movie 5-1, the flows are not only dynamic but also multi-directional containing strong in-plane and out-of-plane components. Certainly, these multi-directional, dynamic flow components emphasize the advantage in 3D VFI methods that capture complete flow profiles compared to the limited planar flow estimations of 2D VFI.

5.4.2 Summative Interpretation of Findings

Overall, this investigation has demonstrated the criticality of selecting an appropriate transmission scheme for 3D least-squares VFI to ensure reliable flow vector estimations. Specifically, the azimuth angles of the transmissions are found to be the foremost indicator of velocity estimation accuracy. In all 3D VFI transmission schemes, the azimuth angles should cover as much of the full 360° range as possible. An important note that can be observed in Figure 5-8, is that the phrasing “highest” azimuth angle span is not always appropriate. Indeed, with three transmissions at azimuth spans >240° a notable increase in estimation error is observed compared to a span of 240°. This error stems from the spacing between the final and initial azimuth angles which, beyond the 240° span, begins to decrease since the angles are no longer equally spaced when the final-to-initial wraparound is considered. Thus, it is more appropriate to state that high azimuth spans up to the complete and equally spaced sampling of the 360° range are favorable. At minimum the azimuth angle span should cover a range of ~150° to ensure reasonable vector estimations.

The relationship between elevational steering and velocity estimation error in this study indicates that lower elevation angles produce more accurate estimates. However, this result is seemingly contradictory to the results of a similar study for 2D VFI (Yiu & Yu, 2016) where larger elevational steering ranges reduced error and variance of the velocity estimates. This discrepancy is likely to be a direct result of the small aperture size of the density tapered spiral array. In least-squares VFI, both 2D

and 3D, velocity estimates are only obtainable in the imaging areas where all transmitted beams overlap. Consequently, elevational steering limits both the width and depth of this overlapping area. In 2D ultrasound, where arrays are several centimeters in length, the impact of elevational steering on the beam overlap area is modest. In 3D ultrasound, on the other hand, the small array apertures severely limit the overlapping region. For example, with a 1cm array aperture (typical of 2D matrix probes) and 10° elevational steering, two oppositely steered plane waves have a lateral beam overlap width of just 3.3mm at a depth of 20mm. By ~29mm depth the overlapping region is completely pinched off. Given that the effective aperture of the density tapered spiral array is just 6mm, because of the density tapering, the overlapping region is even more limited. Even with 5° elevational steering, 3D least-squares VFI with small aperture arrays is limited to only the most superficial peripheral vasculature.

In terms of transmission numbers, our results indicate that velocity estimation error is only marginally reduced with the addition of transmissions. Assuredly, the more important impact of the transmission count is instead the limitation of the velocity estimation range imposed by the effective PRF (true PRF divided by the number of transmissions in a scheme). Considering the direct trade-off in error reduction and velocity estimation range, the number of transmissions will most certainly be selected based on the predicted velocity range of the underlying flow rather than the relatively small decrease in error. Nonetheless, it is advantageous to use the maximum number of transmissions permissible by the underlying flow to obtain the most accurate and least variable velocity estimation.

The helix phantom experiment necessitated the consideration of this trade-off since the vertical flow components are prone to aliasing at relatively low velocities. With the transmission scheme selected, the vertical flows were in fact accurately estimated albeit with some underestimation. This underestimation is not unexpected given the nature of the mean velocity estimator used prior to the least-squares vector calculation. Yet, the horizontal flow components in the helix suffered from significant estimation errors relative to the peak flow velocity (see Figure 5-11 and Table 5-3). As mentioned previously, a likely contributor to this elevated error is the slow velocity present in the helix phantom. Moreover, the limited elevational steering is also undoubtedly a factor; with just 5° elevational steering, the correct estimation of slow lateral flows is challenging given the very high beam-flow angle, σ [see equation (2.1)]. Taken with the results of the straight tube phantoms, which accurately captured faster moving flows with low elevational steering, it indeed seems likely that that the elevated error in the helix phantom is a result of the underlying flow condition. This result is again related to the aperture size of the probe and the consequent limitation of usable elevation angles.

However, it should be noted that many peripheral vascular applications exist within the combined shallow depth and modest velocity estimation ranges of the optimized scheme on a small aperture probe (e.g. carotid artery, brachial artery, etc.).

Given the high velocities observed in the aneurysm phantom, and the close resemblance of the velocity profile to that of the pump, it is assumed that the dynamic flow being estimated is reasonably accurate. Yet, the complex flow conditions here are challenging to directly compare to CFD and are thus left unvalidated. Furthermore, it is not possible to accurately quantify such flows with 2D ultrasound methods given the dynamic shifts between in-plane and out-of-plane flows. These limitations of CFD and 2D ultrasound techniques further highlight the inherent need for 3D VFI methodologies to be optimized for accuracy and reliability. The complex flow dynamics in the aneurysm phantom are, even still, a simplified model of true in vivo dynamics. Such complex flows require optimized transmission schemes that effectively and efficiently sample the flow region while balancing the trade-offs between accuracy and estimation range.

5.4.3 Limitations and Future Work

The most crucial limitation of this work, as stated repeatedly, is the small aperture of the density tapered spiral array which limits the functional elevation steering range, velocity estimation depth, and the estimation accuracy of slow lateral flows. Larger array apertures would likely enable larger elevational steering without seeing the same degradation in performance as observed in this study. It is important to note, however, that this limitation is not specific to the density tapered spiral array as apertures of just 1cm are common amongst sparse and fully addressed 2D arrays in literature [e.g. Petrusca et al., (2018)]. Row-column addressed arrays often have larger apertures, but such arrays are limited to steering only along the x- and y-axes (only 4 possible azimuth steering angles; Sauvage et al., 2018). More recently, a novel large aperture sparse array has been developed called the Costas array (Masoumi et al., 2023) which allows full 3D steering and maintains a low-channel count for portable imaging. Alternatively, to improve the lateral velocity estimation performance on slow flows, other velocity imaging algorithms such as transverse oscillations could be employed. TO are known to have excellent lateral estimation performance but tend to lose accuracy when axial flow components are present such as in the helix phantom (Pihl & Jensen, 2014, Pihl et al., 2014).

Another limitation of this work is the low SNR of the density tapered spiral array which necessitated the use of low attenuation and limited backscattering phantoms as well as microbubble contrast agents.

Both the low attenuation and contrast agents could potentially impact the frequency characteristics of the received transmissions in this study. Tissue attenuation causes a non-linear reduction in signal amplitude that is proportional to the frequency. However, given the shallow imaging depths of this study it is not believed that the lack of attenuation had a perceivable impact on the received frequency spectra. Microbubble contrast agents can result in spectral broadening compared to the transmitted signal which may have had a modest impact on the variance of the mean frequency estimation. But perhaps more importantly is the lack of backscattering from the tissue mimics. Without backscattering, the results of this study are uninhibited by tissue clutter which may have enhanced the performance. Yet, this study still implemented clutter filtering to mitigate the differences between these results and results with a higher SNR probe and tissue clutter.

From the results and analysis presented in this work, there are some research directions which should be further investigated. The first is to test the performance of larger elevational steering on larger aperture 2D arrays. As mentioned above, it is possible that the negative effects seen with increased elevational steering are a direct result of the array aperture and not the steering itself. Furthermore, larger arrays will provide additional performance benefits such as increasing the imaging view enabling the capture of larger vessels. An additional research direction is towards the enhanced validation of 3D VFI studies. While this work leveraged CFD and clinical ultrasound for validation, it was not feasible to validate the complex flow of the aneurysm phantom. To this end, it is possible to employ particle image velocimetry (PIV) to measure 3-component flow on 2D planes or even full volume 3-component flow. Finally, research on intuitive 3D vector visualization strategies will prove invaluable as 3D VFI is advanced and more complex in vivo scenarios are captured. Truly, without clear and interpretable visualizations it is unlikely that clinicians will readily adopt these advanced and valuable techniques.

5.5 Conclusions

To capture the true 3D nature of hemodynamics, clinicians do not currently have a bedside measurement tool; however, with recent advances in 3D ultrasound VFI this critical limitation may be changing. Towards that end, this study has shown a transmission scheme optimization for ultrasound least-squares 3D VFI with the objective of minimizing velocity estimation error. This work has demonstrated that, with informed selections of azimuth angles, elevation angles, and the number of transmissions, accurate 3D flow estimations on a portable research scanner are possible. Future works leveraging least-squares 3D VFI can now be performed without ad hoc transmission scheme selection

and previously performed experiments can be vetted for potential improvements. Additionally, given the relative importance of azimuth angle steering compared to the other parameters, considerations in probe and scanner designs to facilitate full 360° steering capabilities should not be overlooked. Considering the recent rate of advancement in 3D ultrasound research, including both hardware and software innovations, the coming years may see 3D VFI become a frequent contributor to studies of *in vivo* hemodynamics and clinical diagnostics.

Chapter 6
A Volumetric Blood Flow Estimation Framework for a Portable Ultrasound System

6.1 Introduction

In free flap reconstructive surgeries, there is a high rate of post-operative complications and a modest rate of total flap failures (Pohlenz er al., 2012, Kwok & Agarwal, 2017, Bennett et al., 2018, Rose & Puckett, 2023) many of which are related to the vascular function of the flap. Vascular complications include venous or arterial thrombosis, venous congestion, and major bleeding but other high-occurrence complications, such as fat necrosis, have also been linked to vascular function (Lee & Mun, 2016). Complications, depending on severity, and flap failures generally require surgical re-examination, repair, or replacement of the donor tissue (Kwok & Agarwal, 2017) resulting in extended ICU stays and significant risks to the patient. Therefore, the monitoring of vascular function (both arterial inflow and venous outflow) is critical to identify complications as early as possible to prevent extensive damage and minimize hospitalization time.

Despite the clinical importance of post-operative vascular monitoring of free flaps, there is currently no standardized measurement protocol for the flap vascular function (Salgado et al., 2009). As such there are a wide range of methods used at different institutions ranging from simple visual examination and temperature measurements to photoplethysmograms (PPGs) and Doppler pens (Salgado et al., 2009). However, the existing methods are limited to identifying the presence of flow and not quantifying the amount, thus rendering them unable to detect small changes in flow which could indicate an impending complication. Ultrasound imaging presents a promising point-of-care solution to monitor the post-operative blood flow in free flaps, however current 2D clinical methods are not able to reliably quantify the volumetric flow through the vasculature.

Since VBF measurements are inherently 3D, multiple 2D ultrasound scans are required to perform the calculation, opening the door for operator error and repeatability problems. Naturally, 3D ultrasound is better suited to calculating VBF accurately by leveraging 3D VFI methods. However, 3D ultrasound is in a relatively early stage of development and is hindered by high data rates making its implementation on a portable, point-of-care system a significant challenge. While solutions such as sparse arrays (as shown in Chapters 4 and 5) enable the use of benchtop ultrasound systems for 3D

imaging, many do not currently have the SNR required for *in vivo* blood flow measurements, even with signal enhancement methods such as coded excitations (as shown in Chapter 3). Higher SNR solutions being used presently in research often compromise steerability (in the case of RCA; Holbek et al., 2016), require bulky and non-portable equipment (fully populated arrays; Correia et al., 2016, Holbek et al., 2017a, Holbek et al., 2017b, Correia et al., 2020), or have a lack of programmability (micro-beamforming; Savord, 2000).

In this work, we present a 3D ultrasound VBF measurement framework on a benchtop ultrasound scanner by leveraging a fully populated matrix array and 4:1 receive multiplexing. The fully populated transducer array can achieve high enough SNRs for reliable in vivo blood flow measurements, while the 4x1 receive multiplexing limits the acquisition data rates to a level manageable by a benchtop ultrasound scanner. The methodology for VBF calculations is based in the 3D VFI methods presented in Chapter 5 and is validated on both straight tube and tortuous *in vitro* flow conditions. Finally, the VBF estimation framework is applied for *in vivo* VBF estimation on the brachial artery to highlight its applicability for clinical applications including the vascular monitoring of free flaps post reconstructive surgery.

6.2 Methods

VBF is defined as the surface integral of blood flow flux through a closed cross-section of a vessel. To compute VBF, just two quantities are required: 1) the velocity of the blood normal to the closed vessel cross-section (i.e. flux), and 2) the area of the closed vessel cross-section. With ultrasound 3D VFI, these values can be simultaneously acquired. Since 3D VFI outputs the complete 3D, 3-component flow profile within the imaging region, the flux vectors through a vessel in any orientation can be extracted. Additionally, assuming the imaging region is large enough to contain the entire vessel width, the closed vessel cross-section can be identified and segmented. The calculation of VBF from these quantities is simply the numerical integration of the flux over the segmented cross-section.

The VBF estimation framework used in this work is composed of three key steps: 1) a four-stage transmit-receive sequence [Figure 6-1(a)], 2) a 3D least-squares VFI pipeline [Figure 6-1(b)], and 3) VBF estimation from 3D VFI [Figure 6-1(c)].

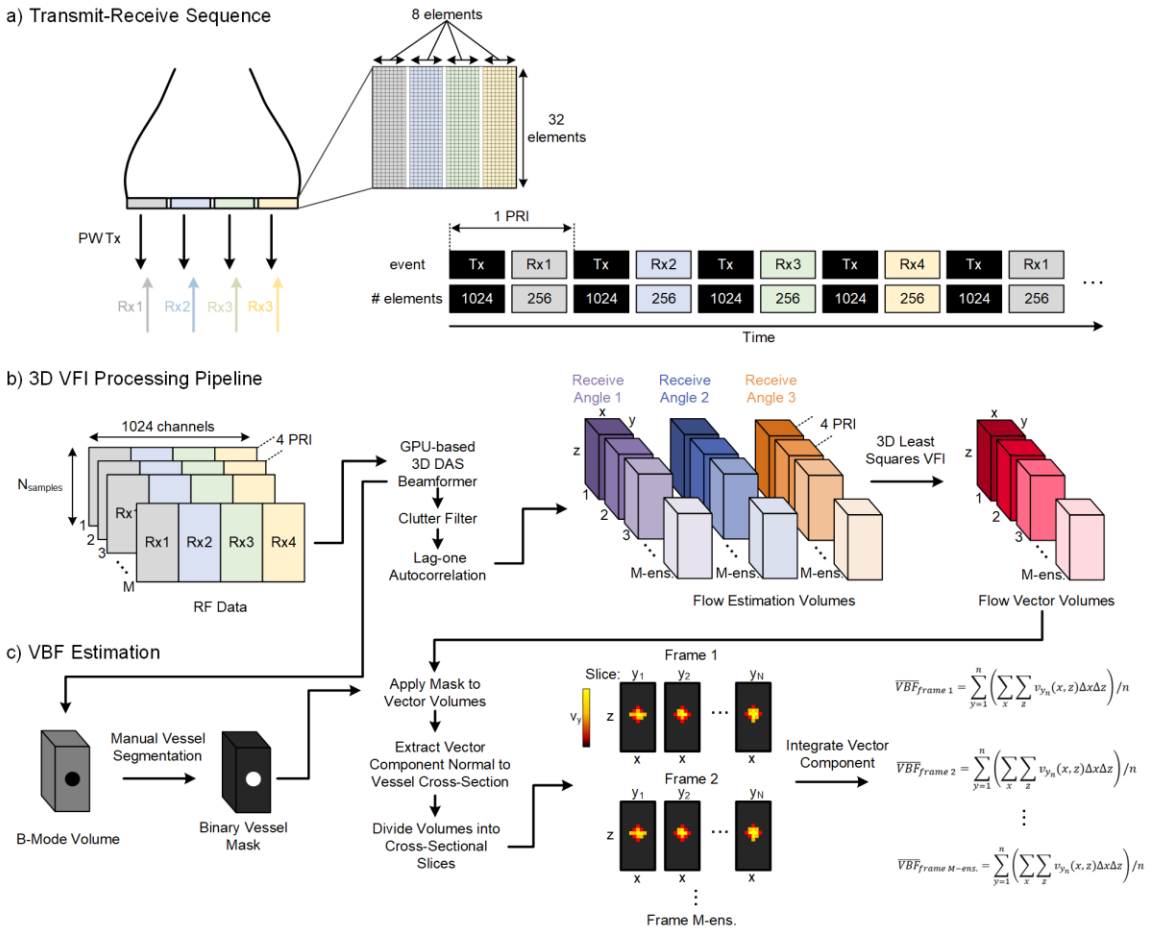


Figure 6-1 Schematic of the transmission scheme and VBF estimation pipeline. (a) Transmit-receive sequence: All elements are used in each transmit event and 256-elements are used in each receive event (1 bank per receive event). The same transmit must be repeated four times to acquire receive signal on all elements. (b) 3D VFI processing pipeline: received channel data from each array bank are combined into a single RF frame for beamforming; the spacing between RF frames is thus 4*PRI. Each RF data frame is beamformed at three different receive steering angles and processed through a mean velocity estimator yielding three velocity estimation volumes per RF frame. The three velocity estimation volumes at different receive angles are passed to a 3D VFI estimator. The output is one vector flow volume per RF frame. (c) VBF estimation: Vessel lumens in the B-mode volumes are manually segmented and converted to binary masks, the masks are applied to the vector volumes and the flow component normal to the closed cross-section of the vessel are extracted. The VBF can be estimated at each slice of the volume with a closed cross-section by integrating the normal flow component.

6.2.1 Imaging Sequence and Methods

The first stage of the VBF estimation framework is the 3D ultrasound data acquisition which was performed using a fully populated 2D matrix array with 1024 active transducer elements (Vermon,

Tours, France). This transducer array consists of four equally sized banks of elements that contain 256 elements each. The banks are 8-by-32 elements and have a one element width gap row between each bank for interconnecting electronics [see Figure 6-2(a)]. The gap rows are parallel to the x-axis of the array. While all elements of the array are intended to produce equal outputs, there is some variability in the performance that is demonstrated in Figure 6-2(b) and (c) which shows the voltages measured at each element. The lower voltage elements are assumed to produce lower transmit pressures and have lower receive sensitivity.

The 2D matrix array is connected to a US4R research ultrasound scanner (US4US Ltd., Warsaw, Poland) which is a benchtop system capable of 1024-element transmissions but is limited to 256-element reception. Therefore, to acquire data from the entire 2D matrix array (i.e. all 1024 elements) the array must repeat the same transmission four times with a reception on a different element bank each time (see Figure 6-1(a) for a schematic of the Tx-Rx scheme). To form images from data acquired by the matrix array, the received signals at the four banks are used together as though they were collected simultaneously. This process yields an effective imaging PRF that is decimated by a factor of four compared to the true transmission rate. In this study, plane wave transmissions [6MHz center frequency, 5-cycle pulse (in vitro), 3-cycle pulse (in vivo), rectangular apodization] are used with a PRI of 1.5e-4s (PRF = 6.67kHz). This yields an effective imaging PRF of 1.67kHz (i.e. 6.67kHz/4).

The use of benchtop imaging hardware and 4:1 receive multiplexing in this work puts a strong limitation on the effective PRF and, in turn, the velocity estimation limits. In particular, the use of multi-angle transmissions for the calculation of 3D flow vectors is not feasible since the effective

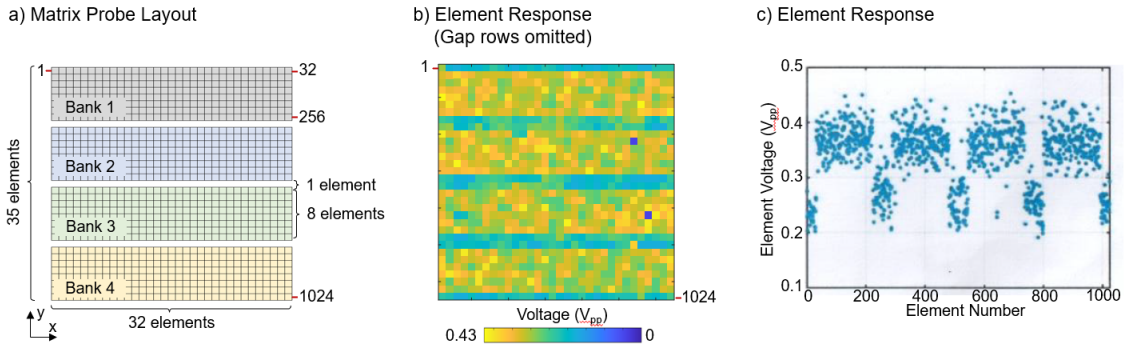


Figure 6-2 Schematic and voltages of the 2D matrix array. (a) Array layout containing four 8x32 element banks with a 1 element space between banks. (b) Element response when a constant activation voltage is applied (gap rows are omitted from the layout). (c) Element response on a scatter plot.

imaging PRF would be further decimated by the number of angles [i.e. 6.67kHz/(4*A)]. Therefore, this framework utilizes a single transmission angle and multiple receive angles. Receive steering is performed during post-processing in the DAS beamformer and has no effect on the data acquisition and subsequent velocity estimation limits. In this study, three receive steering angles are used. The receive steering angles were chosen according to the results on transmit steering in the previous chapter: 5° elevational steering and equally spaced azimuthal steering covering the full 360° range (i.e. 0, 120, 240°).

6.2.2 VBF Estimation Algorithm

Once the data is acquired, steps 2) and 3) of the framework (namely 3D least squares VFI and VBF estimation, respectively), are performed offline in Matlab (MathWorks). The 3D least squares VFI estimation pipeline [depicted in Figure 6-1(b)] begins with the channel-domain RF data from all 1024 array elements (i.e. from four consecutive transmit-receive cycles). This data is bandpass filtered (FIR; passband: 5.5-6.5MHz) and then passed to a GPU-based DAS beamformer modified for 3D imaging (Yiu et al., 2011). The F-number used in the beamformer was 1.5 in all cases. As mentioned above, the beamformer performs receive steering on the RF data which results in a set of B-Mode volumes for each receive steering angle. The images are then clutter filtered (FIR; stopband: ~10Hz) and passed through a lag-one autocorrelator (ensemble length: 64 frames) resulting in the velocity estimation volumes for each steering direction. Finally, a least-squares 3D VFI estimator converts the multi-angled velocity estimates into a single set of flow vector volumes (see Chapter 5 for algorithmic details).

With the velocity vectors computed, the VBF can be estimated by integrating the flux over a closed cross-section of the vessel [depicted in Figure 6-1(c)]. In this study, the vessel lumens are segmented manually on the B-mode images and the size of the segmented region is validated using a clinical ultrasound scanner (GE Venue Go, GE Healthcare) and an L4-12t transducer (GE Healthcare). The segmentation map is applied to the flow vector volumes with all vectors outside of the lumen region being set to zero. From the vessel segmentation, a plane in the imaging volume that contains a closed vessel cross-section can be selected. The vector component normal to the selected plane can be extracted and numerically integrated over the segmented region on the plane to yield a VBF estimate. In this work, multiple adjacent planes are used to obtain a spatial average VBF estimate.

6.2.3 Experimental Methods

To study the performance of the VBF estimation framework, four experimental flow scenarios were used: 1) constant flow in a straight tube, 2) pulsatile flow in a straight tube, 3) constant flow in a helical toroid phantom, and 4) *in vivo* flow in a brachial artery. The straight tube experiment with constant flow is used to assess the baseline accuracy of the VBF estimation framework at different flow rates. The pulsatile flow experiment assesses the ability of the framework to track time-varying flows. The helical toroid phantom enables the validation of the VBF estimation on multi-directional flows. Finally, the in vivo experiment demonstrates the potential of this work for future use in clinical studies.

6.2.3.1 Straight Tube Constant Flow

A walled PVA phantom with an ID of 3.5mm was imaged in water. The phantom was fabricated with a previously described protocol (Chee et al., 2016). BMF was pumped at volumetric flow rates of 1, 2, and 3mL/s by a programmable flow pump (Ho et al., 2017) connected to the inlet of the straight tube. The outlet of the tube was routed back to the pump reservoir. Both the inlet and outlet of the phantom were connected to the pump via flexible vinyl tubing.

At each flow rate, imaging was performed with the probe in two orientations: first, with the y-axis of the probe parallel to the vessel and then with the x-axis of the probe parallel to the vessel. Testing the VBF estimation framework performance in both orientations is essential given the non-uniform layout of the 2D matrix array with respect to its lateral axes [see Figure 6-2(a)]. In each probe orientation, the transmit beam was steered along the flow direction with 5° elevation. That is, when the y-axis of the probe was aligned with the vessel the transmit steering was 5° in elevation and 90° in azimuth and when the x-axis of the probe was aligned with the vessel the transmit steering was 5° elevation and 0° azimuth. In each case, the estimated VBF was compared directly to the programmed output of the pump.

6.2.3.2 Straight Tube Pulsatile Flow

The pulsatile flow experiment used the same walled PVA phantom and flow pump. The pump was programmed to output a carotid pulse profile with a peak systolic flow rate of 2mL/s and a pulse rate of 60bpm. Imaging was performed with the y-axis of the probe parallel to the vessel and the transmission steered 5° in elevation and 90° in azimuth. The measured VBF profile was compared to a

Doppler spectrogram acquired from a clinical ultrasound scanner (GE Venue Go, GE Healthcare) and an L4-12t transducer (GE Healthcare) on the same experimental setup.

6.2.3.3 Helical Toroid Constant Flow

The helical toroid phantom used in this study was previously developed for the investigation of 3D flow imaging methods and was fabricated here using its original protocol (Chee et al., 2021). The geometry of the phantom, which produces omni-directional 3D flow profiles, is shown in Figure 6-3. The programmable flow pump was connected to the inlet of the toroid phantom and was set to output a constant 1mL/s flow. Since the phantom spans a 3.4x3.4cm lateral area, multiple acquisitions were required to capture the flows in each of the four loops of the vessel. The probe was kept in the same orientation with respect to the phantom in all acquisitions and was laterally translated to image different regions.

6.2.3.4 *In Vivo* Flow in a Brachial Artery

An *in vivo* proof-of-concept experiment was conducted on the brachial artery of a healthy volunteer (28 years of age, female) with ethics approval (#22794) from the institutional review board. The volunteer was asked to rest in a seated position for 10 minutes prior to the data acquisition. During the acquisition, the volunteer's left arm was positioned with 90° forward flexion at the shoulder, 180° extension at the elbow, the palm supinated, and resting on a flat surface. The first acquisition was performed using the research imaging system and the 2D matrix array. The probe was oriented with the x-axis parallel to the brachial artery and positioned approximately 5mm distal to the elbow and 25mm proximal to the brachial bifurcation where the brachial artery was found to be ~5mm deep and slightly descending. After data acquisition, the location of the 2D matrix array was marked on the volunteer's

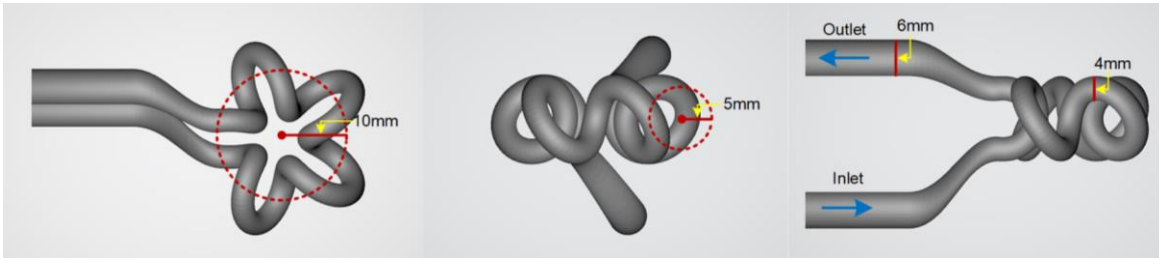


Figure 6-3 Schematic of the helical toroid phantom from a top view (left), end view (center), and side view (right)

arm. Then, the clinical scanner was used to measure the longitudinal plane of the brachial artery with the transducer centered on the mark placed during the first scan.

6.3 Results

6.3.1 Constant Straight Tube VBF is Precisely Estimated with an Offset from the True Value

The straight tube, constant flow VBF estimates in each probe orientation are presented in Table 6-1. For each flow rate and orientation, the VBF was calculated on seven image planes (total range of 1.1mm) centered below the probe and averaged. The estimates were also temporally averaged over 1s of the acquisition. The results show a consistent estimation error between flow rates in each flow orientation; however, the errors vary significantly between the two orientations. With the x-axis of the probe parallel to the flow, the VBF is underestimated by ~40% on average. With the y-axis of the probe parallel to the flow, the VBF is overestimated by ~11% on average. These results suggest that the gap rows in the array layout [see Figure 6-2(a)] impact the performance of the VBF estimation.

6.3.2 Estimated Pulsatile VBF Profile Aligns with the Clinical Velocity Profile

Figure 6-4 shows the results from the straight tube pulsatile flow experiment. As in the constant flow study, the VBF was calculated on seven image planes centered below the probe and averaged. Figure 6-4(a) is the Doppler spectrogram from the clinical ultrasound scanner and Figure 6-4(b) is the estimated VBF profile measured from 3D VFI. The two profiles have similar landmark features, notably the pre-systolic peak, systolic peak, and dicrotic notch. The timings of these landmarks are noted in red in each plot and, relative to the systolic peak, are generally well aligned between the two measurements. The dicrotic notch, however, does occur later in the clinical scanner spectrogram than in the VBF

Table 6-1 VBF measurement results from straight tube experiments

X-Direction Flow			Y-Direction Flow		
True Value (mL/s)	VBF Estimate (mL/s)	Error (%)	True Value (mL/s)	VBF Estimate (mL/s)	Error (%)
-1	-0.51±0.07	-49.4	1	1.12±0.11	12.1
-2	-1.24±0.10	-38.0	2	2.19±0.18	9.7
-3	-1.90±0.13	-36.6	3	3.37±0.31	12.5

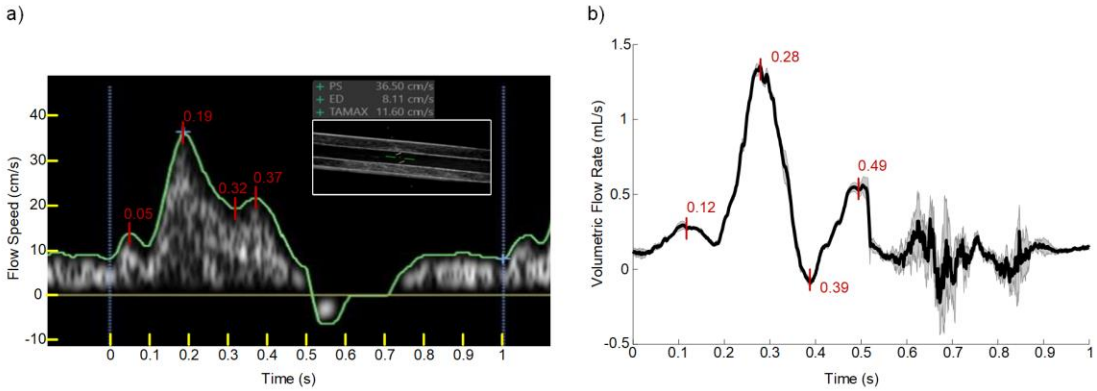


Figure 6-4 *in vitro* carotid pulse from (a) a clinical ultrasound scanner Doppler spectrogram and (b) the VBF estimation framework (black line – mean, grey shaded area – ±1SD). Red annotations mark key points of the cardiac cycle on each plot as measured from time = 0s on the plots. Note that time = 0s between (a) and (b) are not exactly aligned.

profile. Additionally, the dicrotic notch is much deeper in the VBF plot. During diastole, the flow signal is weak resulting in noisy VBF estimates that are not seen in the clinical scanner. This is expected given the higher SNR of the clinical scanner compared to the high-volume-rate 3D VFI system.

Quantitatively, the VBF measured from the 3D ultrasound framework agrees with that from the clinical scanner. From the 3D ultrasound system, the peak systolic VBF is measured to be 1.35±0.04mL/s. In the Doppler spectrogram, the peak systolic velocity is recorded as 36.5cm/s which, considering the inner diameters of the phantom (axial: 3.5mm, lateral: 3.1mm), converts to an approximate VBF of 1.56mL/s if the flow is assumed to be parabolic. Finally, the standard deviation of VBF estimate is very low across the pulse cycle indicating that there is little spatial variation in the estimates across the central image planes.

6.3.3 Multi-Directional VBF is Well-Estimated at Shallow Depths

Flow in the helical toroid phantom was estimated in each of the four phantom loops according to the slices shown in Figure 6-5. VBF estimates were calculated over a single image slice and averaged over 1s of the acquisition. The VBF estimates at each slice and their corresponding measurement depths are reported in Table 6-2. It is observed that the VBF estimates on many slices have errors below 20% of the expected VBF, however, other slices are found to have much higher errors. To visualize this dichotomy, the VBF estimation error on each slice is plotted against the depth of measurement in Figure 6-6. Here, it becomes clear that the slices with high error are exclusively the lateral VBF estimates (x-

and y-direction) at high depths in the phantom (i.e. on the bottom segments of the toroid loops). Meanwhile, the z-direction VBF estimates as well as the shallow lateral estimates have less than 20% error.

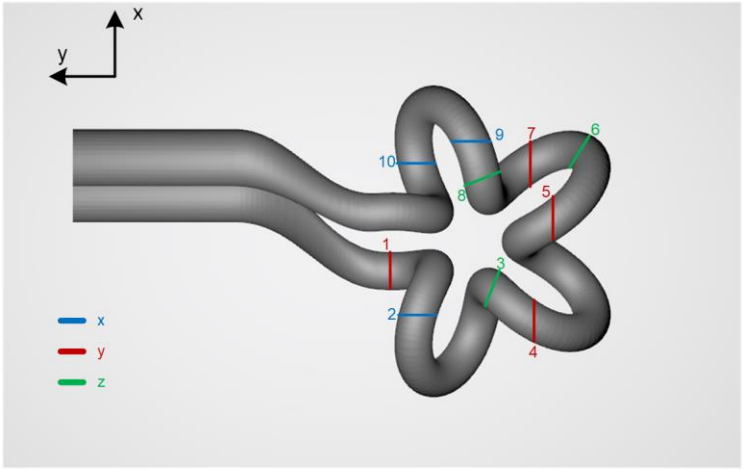


Figure 6-5 Approximate measurement plane locations on the helical toroid phantom. Blue indicates VBF measurements in the x-direction, red indicates measurements in the y-direction, and green indicates measurements in the z-direction. Probe x- and y-axes orientations are indicated in the top left.

Table 6-2 VBF measurement results from the helical toroid phantom experiments

Slice Number	Flow Component	True Value (mL/s)	VBF Estimate (mL/s)	Error (%)	Depth (mm)
1	Y	1	0.35±0.08	-64.8	32.5
2	X	1	0.85±0.09	-15.5	23.5
3	Z	-1	-0.99±0.03	-1.0	26.8
4	Y	1	0.84±0.12	-15.7	22.7
5	Y	1	0.87±0.13	-13.3	22.2
6	Z	1	0.85±0.02	-14.6	27.4
7	Y	-1	-0.40±0.20	-59.6	29.5
8	Z	-1	-0.92±0.02	-8.1	27.4
9	X	-1	-0.97±0.11	-2.8	23.0
10	X	1	-0.01±0.07	-101.4	30.7

6.3.4 *In Vivo* Volumetric Flows Agree with the Clinical Velocity Profile

The results from the *in vivo* implementation of the VBF framework are presented in Figure 6-7. Figure 6-7(a) shows the clinical B-mode image of the brachial artery in the longitudinal view at a depth of ~5mm. Figure 6-7(b) shows the Doppler spectrogram acquired at the location in (a). Figure 6-7(c) presents the estimated VBF profile from the 3D ultrasound framework. Qualitatively, the two profiles are similar in shape with sharp systolic peaks and pronounced dicrotic waves. The Doppler spectrogram indicates that some beat-to-beat variability is present which could impact the comparison of the profiles to some extent. Additionally, approximately 5 minutes was required to switch from the 3D ultrasound system to the clinical system which resulted in a ~10bpm difference in heart rate between the measurements. The peak systolic VBF measured in with the 3D ultrasound system is 2.84±0.56mL/s. With the clinical scanner, the peak systolic velocity is 80.6cm/s which, given the measured inner diameter of 2.96mm, converts to a VBF of 2.77mL/s assuming the flow profile is parabolic.

6.4 Discussion

6.4.1 Statement of Contributions

This work presents a VBF estimation framework based on 3D VFI methodologies that enables repeatable VBF measurements on a portable ultrasound system. By leveraging a fully-populated 2D matrix array, the system SNR was sufficient to obtain *in vivo* VBF estimates with a single plane wave

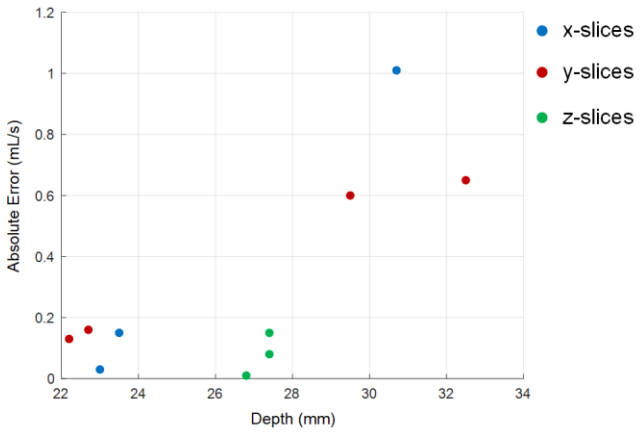


Figure 6-6 Error of VBF measurements in the helical toroid phantom versus measurement depth. X-direction measurements are marked in blue, y-direction in red, and z-direction in green.

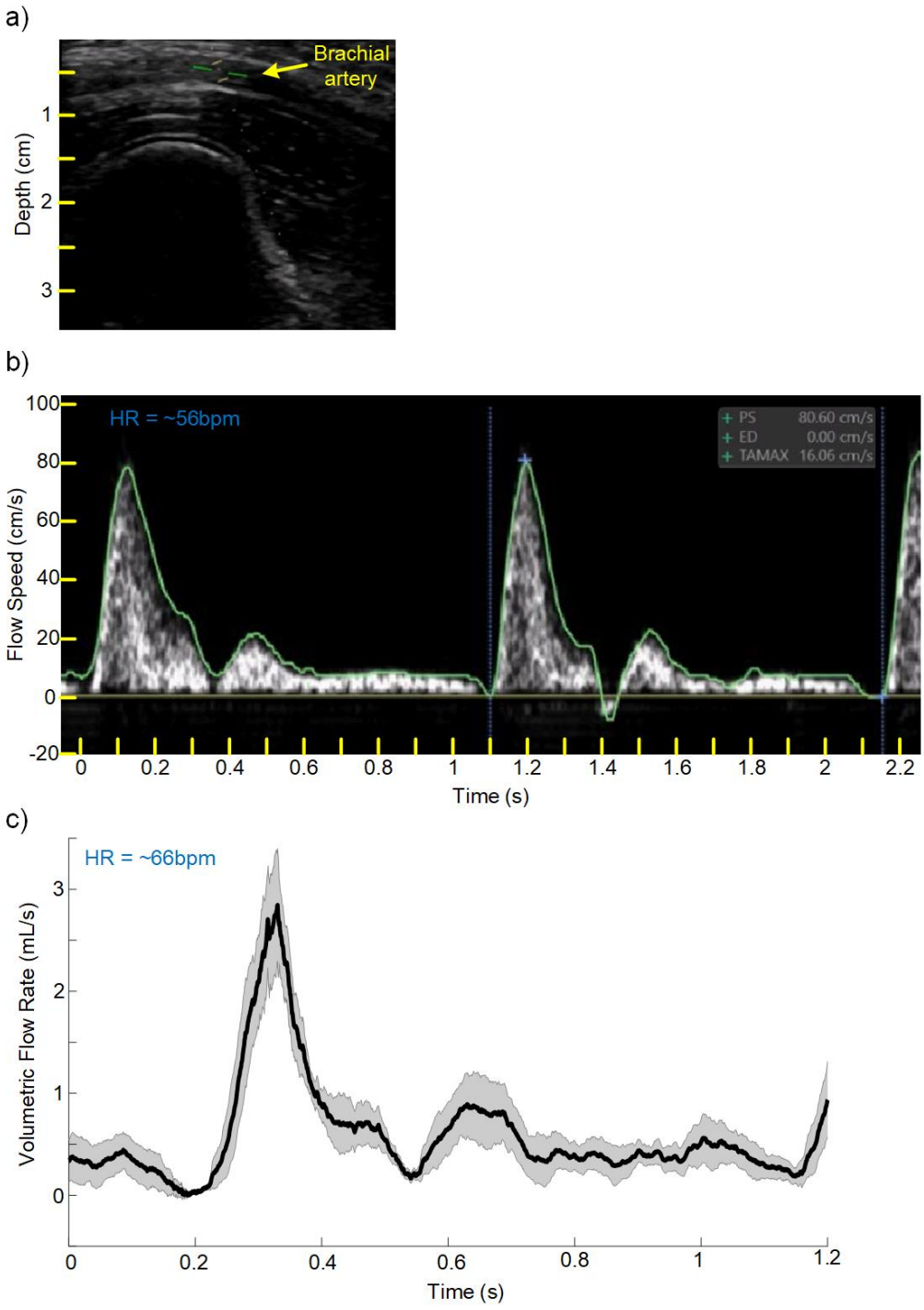


Figure 6-7 Measurements of the *in vivo* brachial artery flow. (a) Clinical B-mode image of the brachial artery in the longitudinal view, (b) Clinical scanner Doppler spectrogram, (c) estimation profile from the VBF framework.

transmission. To the best of our knowledge, this is the first work that demonstrates VBF measurements from a single plane wave transmission angle thereby maximizing the velocity estimation limit before the onset of aliasing. Yet, despite the numerous existing works with the same 2D matrix array for 3D flow imaging (Provost et al., 2014, Correia et al., 2016, Holbek et al., 2017a, Holbek et al., 2017b, Correia et al., 2020), the axis-dependent architecture of the array necessitated the investigation of VBF estimation performance along different flow directions. Certainly, the accuracy of any VBF estimation tool must be rigorously tested and calibrated on a range of scenarios prior to any application for clinical blood flow monitoring.

This study demonstrates the precision of VBF estimations when 3D VFI is leveraged for the calculation. Table 6-1 shows the VBF estimations for different flow rates and probe orientations. Here it is observed that both the x- and y-directions have a significant, but consistent, offset from the underlying true flow value. When the flow is aligned with the y-axis of the array it is more accurately estimated than along the x-axis indicating that the array architecture has an impact on the VBF estimations. With pulsatile flow, shown in Figure 6-4, the estimated VBF profile matches the Doppler spectrogram acquired from a clinical scanner. This result indicates that, while there may be an offset between the estimated and true VBF, estimating VBF from 3D VFI enables the reliable acquisition of time varying VBF profiles. When tested on multi-directional flows, as shown in Table 6-2, the VBF estimation framework demonstrated good performance regardless of flow direction. However, the performance on lateral flows was severely degraded at higher depths. With the current limitations in probe aperture sizes and in turn elevational steering, accurately resolving lateral velocities at depths greater than ~25mm is challenging.

Finally, the VBF estimation framework was tested on an *in vivo* flow to demonstrate the feasibility of its application to future clinical scenarios. Figure 6-7 shows the comparison between the estimated VBF profile and a Doppler spectrogram from a clinical scanner on a brachial artery. As in the *in vitro* pulsatile flow study, the shape of the VBF estimation generally matches the Doppler spectrogram. However, there may be an offset between the measured VBF values and the true underlying flow that cannot be directly assessed in an *in vivo* experiment. Again, there is a strong need for rigorous calibration of the VBF estimation framework prior to clinical application. Nevertheless, the *in vivo* results show the substantial potential for reliable VBF measurements to move to the clinic in the coming years including for the vascular monitoring of free flaps.

6.4.2 Summative Interpretation of Findings

Generally, this work has shown the promise in deriving VBF estimations from 3D VFI, but the criticality of characterizing both the axis dependence of the results and the offset from the true flow value cannot be understated. The axis dependence shown in the constant flow straight tube results (Table 6-1) is an indication that the gap rows in the array layout have a strong effect on the 3D VFI and consequently VBF estimates. Further, the voltage map of the elements (presented in Figure 6-2) shows that the potential impact of the gap rows extends beyond the single line of non-active elements and lowers the responsiveness of the surrounding rows as well. This fact may result in greater than expected secondary lobe levels or a non-uniform main beam profile that could alter the velocity estimates (as discussed in Chapters 4 and 5). The results on multi-directional flows, however, indicate that the x-direction performance is not unanimously poor as indicated by the straight tube results. Instead, it seems as though the performance is spatially dependent which is further evidence of a potentially non-uniform beam profile or high side lobe levels. Regardless, if the spatial and directional dependence of the results can be characterized, calibration of the VBF estimation framework may be possible to mitigate the resulting errors.

The pulsatile flow results presented here highlight a new VBF estimation capability from 3D VFI that would be time-consuming and inaccurate if performed manually from 2D ultrasound scans. Indeed, the high-temporal resolution of 3D VFI enables hundreds or even thousands of VBF estimations per pulse cycle. This resolution enables more accurate estimates of VBF during key points of the cardiac cycle (e.g. peak systole) with minimal temporal averaging. While such time-resolved measurements may not be critical in peripheral vascular assessments, they pose a unique opportunity for the assessment of more complex and dynamic flows in the future (e.g. cardiac).

Finally, the *in vivo* proof of concept on the brachial artery shows that reliable VBF estimation may soon be ready for wider clinical studies and eventual translation. The SNR of the high-volume-rate 3D ultrasound system used in this study is sufficient for the acquisition of in vivo flows and its live 3D imaging mode enables navigation to the desired measurement location. Additionally, the use of a portable research ultrasound system in this work is critical to its extension to future clinical research. In the case of vascular monitoring of free flaps post reconstructive surgery, VBF measurements must be performed at the bedside since the patients are typically kept in critical care wards for multiple days after surgery. Therefore, any practical VBF measurement solution must be, at minimum, a cart-based tool that can be readily moved to a patient's bedside with minimal disruption to the clinician's

workflow. Indeed, the portability of the 3D ultrasound system used in this work is of critical importance and sets it apart from many previous works on large scale systems (Correia et al., 2016, Holbek et al., 2017a, Holbek et al., 2017b, Correia et al., 2020).

6.4.3 Limitations and Future Work

While this work has demonstrated the precision of VBF estimations from 3D VFI, it has also shown that the current method lacks accuracy. The errors introduced into the VBF estimation likely stem from many factors which should be thoroughly and independently investigated. The first factor, as indicated above, is the beam profile from the 2D matrix array. Given the non-rotationally symmetric array layout, it is likely that the spatial and axis-dependent changes in the VBF estimations are a result of the gap rows in the array; especially considering that axis independent 3D VFI performance was demonstrated in Chapter 5 with a radially uniform array. Thus, it is critical that a thorough field profile study is performed on the 2D matrix array to assess both the main beam uniformity and the secondary lobe levels (such as was performed on the spiral array in Chapter 4). Additionally, if higher SNR sparse arrays are developed that can effectively perform *in vivo* acquisitions (see Section 4.4.3), it may be possible to use a radially uniform array such as the density tapered spiral array instead of a fully populated array for VBF measurements. Not only would this alleviate the axis-dependent performance found in this study, but it would also eliminate the need for 4:1 receive multiplexing.

The second factor that may be introducing error into the VBF estimation is the vessel segmentation. Naturally, accurate vessel segmentation is critical to achieving accurate VBF estimations, but, with the image quality available in 3D high-volume-rate imaging, it is exceedingly challenging. In this work the vessels were manually segmented and compared to clinical B-mode measurements, however, this process is time consuming and operator dependent making it impractical in a larger clinical research setting. Certainly, for this VBF estimation framework to be applicable in a broad context a reliable, automatic vessel segmentation pipeline must be implemented. Such a pipeline could leverage recent advances in machine learning-based ultrasound image segmentation (Mishra et al., 2019, Azzopardi et al., 2020, Dong et al., 2021). Moreover, the vessel segmentation should also account for changes in vessel diameter throughout the cardiac cycle (which was not done in this work) to further increase the VBF estimation accuracy.

A third factor creating error in the VBF estimates is the effect of the clutter filter. While suppressing the vessel wall signal is essential for the accurate estimation of flows within the vessel, it is well known

that clutter filtering hinders the estimation of low velocity flows. In this work, a simple FIR high-pass filter was implemented to remove signals with low Doppler frequencies, however, some of these signals were undoubtably from blood flow near the vessel walls. In the future, the application of more sophisticated clutter filtering techniques such as eigen-based filters (Yu & Lovstakken, 2010) may help to retain the low velocity blood flow signals while sufficiently suppressing the tissue clutter.

Aside from factors listed above, it is also true that the four-times repetition of the transmit sequence is a limitation of the VBF estimation framework presented here. This repetition strongly limits the ability of this framework to accurately estimate high velocity flows due to the early onset of aliasing with such low achievable PRFs. However, the use of four scanners simultaneously (as is being tested in many research settings) is not seen as a practical solution to this problem since the size of such a system makes it unusable in the clinic. Alternatively, using advanced techniques to increase the velocity estimation range (such as ChiVE presented in Chapter 3) may be more suitable. However, the limitations of the ultrasound scanner itself must be considered in the implementation (e.g. many scanners cannot produce chirps). Additionally, novel machine learning techniques could be used to artificially increase the PRF in post-processing which would increase the velocity estimation range without making any changes to the system.

6.5 Conclusions

Clinicians do not currently have a bedside tool to quantify the volume of blood perfusing free flaps post reconstructive surgery despite the established clinical significance of this metric (Salgado et al., 2009, Lee & Mun, 2016). To address this technological gap, this work has presented a VBF estimation framework leveraging a portable 3D ultrasound system. The framework devised here provides consistent VBF estimation performance that may be appropriate for future clinical studies on the perfusion of free flaps. Yet, the results of this study have also indicated the need for rigorous calibration of VBF estimations since there are many opportunities for biases to impact the output values. Indeed, future works should thoroughly investigate the parameters that influence VBF calculations in a wide range of flow scenarios before any clinical applications. Despite these hurdles, 3D ultrasound has strong potential to improve the vascular monitoring of free flaps; with close collaboration with clinicians, 3D ultrasound researchers have the potential to address a significant clinical need in the coming years.

Chapter 7
Summary of Contributions and Future Research Directions

7.1 Summary of Thesis

Free flap surgery is a procedure used to reconstruct tissue after extensive damage from the surgical removal of tumors (Başaran et al., 2021, Rose & Puckett, 2023), major trauma (Bullocks et al., 2006, Koepple et al., 2019, Khundkar, 2019, Alam Atiq et al., 2020), and even burns (Brewin et al., 2020, Jabir et al., 2015). The differentiating characteristic of free flaps compared to other tissue transplants (e.g. grafts, local flaps, rotator flaps) is that free flaps contain major blood vessels which are severed from the donor site and reattached at the recipient site (Icahn School of Medicine at Mount Sinai, 2019, Saber et al., 2022). This technique gives clinicians the flexibility to use far-away donor tissues from the recipient site while also enabling immediate perfusion of the transplanted tissue. Because of the delicate nature of the transplanted vasculature, free flap surgeries have a high risk of complications resulting from insufficient or occluded blood flow (Salgado et al., 2009). Thus, there is a strong clinical need for a quantitative and reliable vascular monitoring tool for patients post-operatively. While several tools are used in the clinic currently, none can reliably and quantitively provide the volume of blood perfusing the flap (Salgado et al., 2009, Steenbeek et al., 2022). Ultrasound, as a point-of-care imaging modality, could be implemented as a solution for free flap vascular monitoring. However, current clinical ultrasound technology, because of its 2D nature, requires numerous approximations to estimate VBF and has questionable reliability (Hussain et al., 1996, Rubin, 1999, Hoyt et al., 2009). 3D ultrasound presents a natural solution to this problem, but many modern solutions lack the portability, volume rates, or SNR required for dynamic blood flow mapping at the bedside.

The goal of this thesis was to advance the current state-of-the-art of 3D ultrasound imaging for the application to free flap vascular monitoring at the bedside. To this end, four research objectives were proposed:

1) to increase the SNR of ultrasound flow estimation for plane wave imaging paradigms,
2) to investigate the feasibility of high-volume-rate imaging on a sparse transducer array which lowers the size required for the ultrasound system,
3) to optimize 3D VFI for accurate and reliable velocity estimations, and

4) to devise the first realization of VBF estimations from 3D VFI on a portable ultrasound scanner suitable for bedside imaging.

These research objectives were addressed in Chapters 3-6 of this dissertation, respectively. In Chapter 3, a novel ultrasound velocity estimation framework was developed and validated. This framework successfully enhanced the SNR of the flow signal compared to the traditional method, lag-one autocorrelation. Additionally, the framework outperformed lag-one autocorrelation in velocity estimation accuracy and range. In Chapter 4, the performance of a density tapered-spiral array was assessed for high-volume-rate imaging compatibility through a field profile analysis of unfocused transmissions. The transmitted waves from the sparse array were found to be homogeneous with low secondary lobes and predictable arrival times indicating that the array is suitable for both imaging and flow estimations with unfocused transmissions. Chapter 5 applied the spiral array to an optimization study of transmission schemes for 3D VFI. This work revealed that maximizing the span of azimuthal steering angles and maintaining a low elevational steering are critical considerations in transmission scheme design. It was also discovered that the number of transmissions has only a modest impact on the estimation accuracy. Finally, Chapter 6 realized the first 3D ultrasound VBF estimation framework with a portable ultrasound system *in vivo*. The results of the VBF estimations demonstrate the framework's ability to accurately quantify VBF while also highlighting the necessity of rigorous calibration studies. In summary, each of the outlined research objectives were addressed in a systematic and comprehensive manner to advance the state-of-the-art of bedside 3D ultrasound and to move the field closer to reliable, clinically relevant measurement capabilities.

From an engineering perspective, this body of work enhances the understanding of 3D ultrasound methodologies and presents novel frameworks that build upon the capabilities of the technology. The algorithmic innovations of ChiVE (Chapter 3) leverage the newfound capabilities of open-platform research ultrasound scanners with arbitrary waveform generators (Boni et al., 2016) to increase SNR and produce enhanced velocity estimations via chirp-coded excitations. Next, concerns in the ultrasound community on sparse array unfocused transmission quality were investigated (Chapter 4). This investigation found that a density tapered spiral array produces uniform unfocused beams and that the element sparsity does not greatly impact the wavefront profile. These results may encourage future sparse array investigations for high-volume-rate imaging (e.g. novel array layouts or imaging applications). Given the radial uniformity of the spiral array transmissions with steering, the array was applied to the parametric optimization of 3D VFI transmission schemes (Chapter 5). This study

revealed the significant impact of transmission schemes on the velocity estimation error and should be used to inform scheme selection in future studies. The 3D VFI optimization results were leveraged for accurate VBF estimations (Chapter 6), albeit in receive steering instead of transmit steering. The VBF estimation framework presented is not only the first on a portable research scanner, but also the first to utilize a single transmission angle for multi-angle 3D VFI.

Clinically speaking, this dissertation also demonstrates several new developments for vascular monitoring of free flaps as well as other VBF measurement applications. Any technology to be used for free flap monitoring must have a small enough footprint to prevent disruption to the ICU workflow; this requirement is satisfied by performing 3D ultrasound VBF measurements on a system the size of a clinical 2D ultrasound scanner. Indeed, this work highlights the capabilities of small-scale 3D ultrasound technology and its potential for future clinical applications. A core focus of the work presented here is the accuracy of blood flow measurements performed with this technology to ensure that clinicians have access to reliable, quantitative data that accurately represents the true flow conditions. This focus was driven by the identified need in free flap monitoring for repeatable and objective measurements to assess vascular health (Salgado et al., 2009). Another focal point of this work was maximizing the achievable velocity estimation range through novel pipelines (Chapter 3) and carefully designed acquisition schemes (Chapters 5 and 6). With extended velocity estimation ranges, clinicians can measure a broad scope of vessels and pathologies, including a wider array of free flaps and as well other vascular conditions such as arterial stenosis which have characteristically high blood velocities (de Bray et al., 1997). Additionally, Chapter 3 presented a means to increase the SNR of high-frame-rate flow imaging which could facilitate the acquisition of deeper vessels. This advancement may be critical to the vascular monitoring of larger free flaps where the main flap vessels are deeper such as those used in breast reconstructions (Lee & Mun, 2016). While the VBF estimation framework presented in this dissertation is not yet ready for clinical trials on free flap monitoring, the critical steps to reach that point have been detailed. With calibration of the VBF estimator and refinements to the system functionality (e.g. user interface, on-board processing) it is hoped that the coming years will see the first 3D ultrasound studies on the post-operative vascular function of free flaps.

7.1.1 Specific Contribution 1: Enhanced Flow Estimations with Wideband Transmissions

Chapter 3 presented a novel ultrasound velocity estimation framework, called ChiVE, which is designed to increase the SNR of high-frame-rate velocity estimations, using chirp-coded excitations, without sacrificing the velocity estimation performance. Chirp-coded excitations have previously been considered ill-suited to Doppler ultrasound applications because of their wide bandwidth which increases velocity estimation variance. Recent work has shown their ability to increase Doppler SNR (Ramalli et al., 2021) but has not addressed issues related to the bandwidth. The ChiVE framework is the first fully customized pipeline for Doppler processing with wideband transmissions.

The results of ChiVE show its ability to map the underlying flow profiles more accurately than lag-one autocorrelation (Figure 3-4). As well, ChiVE has a built-in aliasing resistance that enables extended range velocity estimation passed the Nyquist limit [Figure 3-4(e) and (f)]. In low SNR imaging scenarios ChiVE significantly reduced velocity estimation error (Figure 3-7) and increased Doppler SNR by 6 to 9dB over standard transmissions. This performance was consistent on dynamic, anthropomorphic flows (Movie 3-1) indicating its promise for future *in vivo* applications.

Overall, the ChiVE framework was found to enhance velocity estimation performance compared to standard transmissions and lag-one autocorrelation. The framework demonstrates the advantages of utilizing the complete ultrasound and Doppler frequency spectra to generate a more robust velocity estimator than lag-one autocorrelation and enable anti-aliasing functionality. The increased Doppler SNR realized with chirped excitations may enable the capture of deeper vessels which are subject to greater acoustic attenuation along the beam path. Additionally, ChiVE could be applied to 3D VFI imaging which suffers from even lower SNRs than 2D due to the complete defocusing of the transmissions.

7.1.2 Specific Contribution 2: 3D VFI with a Sparse Array

Chapters 4 and 5 both detailed work on a density tapered spiral array with a focus on the transmissions and their impact on 3D VFI. Previously, it was uncertain whether sparse arrays could produce unfocused beams without wavefront irregularities corresponding to the large gaps between the elements. Additionally, there had been no investigation on the optimal transmissions for 3D VFI resulting in studies using potentially excessive numbers of transmissions. Thus, there has been notable

uncertainty surrounding transmissions in high-volume-rate 3D VFI, particularly on the feasibility of sparse arrays and the requirements for accurate vector flow estimates.

The results in Chapter 4 show that the spiral array can produce homogeneous wavefronts in both steered and unsteered conditions (Figure 4-6). The performance of the array was found to be radially-uniform with no axis-dependent artifacts. It was also found that the wavefronts had smooth arrival times with no irregularities stemming from the sparsity of the elements (Figure 4-7). Generally, Chapter 4 concluded that the spiral array is suitable for high-volume-rate imaging with unfocused transmissions which enabled the study presented in Chapter 5. Indeed, the parametric sweep of transmissions for 3D VFI estimations would not have been possible without an array capable of producing radially uniform beam profiles regardless of steering.

The results of Chapter 5 show the critical importance of transmission scheme design to ensure accurate 3D VFI estimations. The parametric sweep found that azimuthal steering is the most important consideration in transmission scheme design. Low azimuth angle spans (closely spaced transmit beams) are found to produce highly erroneous velocity vectors compared to high azimuth angle spans (widely spaced transmit beams) which produce vectors that closely match the underlying flow profile (Figure 5-5). Additionally, it was found that low elevational steering produced more accurate flow vector estimates than high elevational steering (Figure 5-6) which is counter-intuitive considering previous work in 2D ultrasound (Yiu & Yu, 2016). Yet, the negative impact of high elevational steering is reasonable when the small aperture of the sparse array is considered. Lastly, the number of transmissions used in the least-squares vector estimation was found to have the least significant effect of the vector estimation quality (Figure 5-7). When applied to dynamic and multi-directional flows, the optimal transmission scheme produced reasonable results (Movie 5-1) but struggled to capture slow lateral flows due to the low elevational steering (Figure 5-11).

The work on the density tapered spiral array in this dissertation has demonstrated the promising characteristics of the array and its utility in 3D VFI. This array architecture is one of the only designs that enables full 3D steering without directional dependence on the beam profile making it highly desirable for the study of multi-angled transmission schemes. The performance of the array ensures that the results in Chapter 5 are a result of the steering angles independent of the array properties. As such, the results from the 3D VFI optimization can be directly applied to future 3D VFI imaging schemes regardless of the array type (e.g. sparse, RCA, fully populated) to minimize estimation error and

variance. Additionally, the limited impact of transmission count on the 3D VFI results found in this work signifies that transmission schemes can be tuned to the desired velocity estimation range with a modest trade-off in estimation variance (i.e. fewer transmissions for wider estimation ranges and increased variance).

7.1.3 Specific Contribution 3: VBF Estimation on a Portable Ultrasound System

Chapter 6 presents a framework for VBF estimations from 3D VFI on a portable ultrasound system. Previous works on VBF estimations with 3D ultrasound have shown good results but have been limited in their clinical applicability because of the large-scale scanners being used (Correia et al., 2016, Holbek et al., 2017a, Holbek et al., 2017b, Correia et al., 2020). This work demonstrates a means for collecting VBF data at the bedside that could promote the adoption of 3D ultrasound as a vascular research and diagnostic tool. This is particularly important in the context of free flap vascular monitoring where a portable VBF estimation tool could significantly improve the detection of post-operative complications (Salgado et al., 2009, Chao et al., 2013, Knoedler et al., 2023).

The results presented in Chapter 6 indicate that VBF can be accurately estimated from 3D VFI using the proposed framework, however there are directional and spatial dependencies in the results which produce consistent offsets from the ground truth (Table 6-1 and Table 6-2). These dependencies likely stem from the gap rows and non-uniform voltage profile on the 2D matrix array being used (see Figure 6-2 for a schematic) which are expected to produce interference patterns in the beam profile. Additionally, the small aperture of the probe contributed to the poor performance with increasing depth (Figure 6-6). Despite the offsets in the results, the framework has exhibited good relative performance on dynamic flows both *in vitro* and *in vivo* (Figure 6-4 and Figure 6-7). The framework traced the expected shape of the VBF profile in both dynamic flow cases when compared to a clinical scanner velocity profile.

Generally, the results of the VBF estimation framework show a positive future for bedside VBF estimation using 3D ultrasound. Yet, before this can be implemented, extensive calibration of the estimates is required considering the spatial variability. It is expected that such a calibration could be performed by considering the unfocused transmission beam profiles and identifying fluctuations in the intensity and arrival times (like the protocol used in Chapter 4). A unique aspect of this work was the use of a single transmission angle and multiple receive angles for the 3D VFI calculation. The single transmit angle maximized the achievable velocity estimation range and thus facilitated the application

of the framework to *in vivo* estimates. The unconventional acquisition scheme used in this framework highlights the critical design trade-offs that must be reconciled to implement 3D ultrasound at the bedside (e.g. estimation variance was sacrificed for higher velocity estimation range).

7.2 Future Research Directions

7.2.1 Extension of ChiVE to 3D Ultrasound

A natural extension of the work presented in this thesis is to implement the ChiVE framework (Chapter 3) in 3D ultrasound for SNR enhancement. While the signal enhancement strategies used in ChiVE were intended to enhance 3D ultrasound SNR, this has not yet been performed due to hardware limitations. The density tapered spiral array utilized in Chapter 4 and 5 is presently constructed with a passive receive ASIC that adds substantial parasitic capacitance to the device (Savoia et al., 2018). This capacitance renders the array unable to receive echoes from flow scatterers unless contrast agents are used, regardless of the SNR enhancements provided by ChiVE. An additional restriction on the implementation of ChiVE is the need for an ultrasound system capable of generating chirp pulses. Currently, the ULA-OP 256 system is one of the few available systems with this functionality (Boni et al., 2016) but this system does not have the built-in multiplexing capabilities of the US4R system (US4US Ltd.) required to run the 2D matrix array used in Chapter 6. Despite these hardware challenges, ChiVE would be highly advantageous in 3D ultrasound because of its SNR increases, improved velocity estimates, and extended velocity estimation range.

7.2.2 Calibration of VBF Estimations

Another clear future direction is the calibration of the VBF measurement framework as described in Chapter 6. Currently, the VBF estimations are consistent but have a notable offset from the ground truth in some cases. This offset was found to be directionally and spatially dependent due to the architecture of the 2D matrix array used (see Figure 6-2). Therefore, an extensive calibration protocol is required before this framework can be implemented in broader clinical studies. As a first step of this calibration, a detailed field profile study, as performed in Chapter 4, should be carried out on the 2D matrix array. With a detailed map of the transmitted field profile, it may be possible to compensate for the potential field irregularities with customized apodizations and delay profiles. Afterwards, a systematic phantom study should be conducted to assess any remaining spatial or directional variations in performance.

Naturally, another related future direction is the investigation of the VBF estimation framework on other arrays. It is likely that sparse arrays or RCA arrays, which do not have the regularly spaced gap rows of the fully populated array, could produce more spatially uniform VBF estimates. The density tapered spiral array would be an ideal candidate for such an investigation if the receive sensitivity can be increased to a level capable of measuring *in vitro* and *in vivo* flows without contrast agents.

7.2.3 Visualization of 3D Ultrasound

A constant challenge in the field of 3D ultrasound is the intuitive visualization of 3D ultrasound data (both structures and flow). Since the advent of 3D ultrasound in the early 1990s, visualization of the image volume has been a topic of ongoing research. Most of this work has focused on presenting a subset of the image volume either as a set of slices through the volume or as a structural surface within the volume (Nelson & Elvins, 1993, Nelson & Bailey, 2000, Fattal & Lischinski, 2001, Gee et al., 2004, Varandas et al., 2004, Cho et al., 2020). Such renderings have been adapted and applied in augmented reality as an intuitive means to guide surgical interventions since tumors and other masses are generally segmentable surfaces within the volume (Sato et al., 1998, Cattari et al., 2021). Applications to ultrasound flow imaging, however, have been more limited. Most dedicated works to 3D visualization of vasculature present surface representations of vessels with limited or no flow rendering (Bamber et al, 1992, Schulte zu Berge et al., 2014, Šteňo et al, 2016). Without any standardized method of 3D flow visualization, recent works on 3D VFI have often had to modify existing 2D VFI visualizations such as vectors or streamlines with mixed results in terms of intuitiveness (see Chapter 5, Correia et al., 2016, Holbek et al., 2016). For 3D VFI to be adopted clinically, there is a pressing need for improved visualizations that intuitively present the data to practitioners. Dedicated studies on novel 3D B-mode and flow visualization techniques should be performed in the coming years. Such studies should leverage surveys of clinicians on the usability and clarity of the representations to advance clinical adoption.

7.2.4 Wearable Ultrasound for Continuous Monitoring

For the vascular monitoring of free flaps, the ideal solution is generally accepted to be a continuous monitoring tool that eliminates the need for frequent clinician check-ins (see Section 1.1.2, Salgado et al., 2009). To that end, the development of a wearable ultrasound VBF monitor is a potential avenue for investigation. Recent works have shown the potential of wearable ultrasound patches for hemodynamic, tissue, and organ monitoring including cardiac imaging (Kenny et al., 2021, Wang et

al., 2022, Lin et al., 2023, Hu et al., 2023). These novel devices are opening the door to advanced critical care monitoring and personalized medicine (Kenny et al., 2022) and could also be applied to free flaps. However, there are a number of challenges that need to be addressed before wearable ultrasonic devices can be used in the free flap post-operative setting. Of particular note, is the adhesion of the patch to the patient's skin which, in the case of a recent tissue transfer, is extremely delicate. Current research on wearable patches focuses primarily on the biocompatibility, acoustic coupling, and longevity of the adhesives being used (La & Le, 2022) but in the case of free flaps additional research will be required to ensure the adhesion and removal of the patch does not damage the tissue. Additionally, the implementation of 3D VFI methods for VBF estimation is typically computationally intensive (even with low channel count systems) and would need to be heavily streamlined and simplified for compatibility with a wearable device with no physical connections to external processors and limited data transmission bandwidth.

References

Alam Atiq, M. M., Shahid, S., Ubaid, M., Rahman, M. F., & Shaikh, S. A. (2020). Free flap reconstruction after lower limb trauma - outcome analysis using national surgical quality improvement programme (NSQIP) parameters. *Journal of the Pakistan Medical Association, 70*(Suppl 1)(2), S113-S117. https://www.ncbi.nlm.nih.gov/pubmed/31981349

Allam, O., Shah, R., Cadwell, J., Dinis, J., Peck, C., Junn, A., . . . Alperovich, M. (2022). Evaluation of complication rates of free flap reconstruction in pediatric patients. *Journal of Indian Association of Pediatric Surgeons, 27*(4), 428-434. doi:10.4103/jiaps.jiaps_129_21

Austeng, A., & Holm, S. (2002). Sparse 2-D arrays for 3-D phased array imaging - design methods. *IEEE Transactions on Ultrasonics, Ferroelectrics, and Frequency Control, 49*(8), 1073-1086. doi:10.1109/TUFFC.2002.1026019

Azzopardi, C., Camilleri, K. P., & Hicks, Y. A. (2020). Bimodal automated carotid ultrasound segmentation using geometrically constrained deep neural networks. *IEEE Journal of Biomedical and Health Informatics, 24*(4), 1004-1015. doi:10.1109/JBHI.2020.2965088

Bamber, J. C., Eckersley, R. J., Hubregtse, P., Bush, N. L., Bell, D. S., & Crawford, D. C. (1992, Sep 22). *Data processing for 3-D ultrasound visualization of tumor anatomy and blood flow* [Conference Paper]. Proceedings of SPIE 1808: Visualization in Biomedical Computing '92, Chapel Hill, North Carolina, 651-663. doi:10.1117/12.131117

Başaran, B., Ünsaler, S., Kesimli, M. C., & Aslan, İ. (2021). Free flap reconstruction of the head and neck region: A series of 127 flaps performed by otolaryngologists. *Turkish Archives of Otorhinolaryngology, 59*(2), 103-110. doi:10.4274/tao.2021.2021-1-9

Bennett, K. G., Qi, J., Kim, H. M., Hamill, J. B., Pusic, A. L., & Wilkins, E. G. (2018). Comparison of 2-year complication rates among common techniques for postmastectomy breast reconstruction. *Archives of Surgery (Chicago. 1960), 153*(10), 901-908. doi:10.1001/jamasurg.2018.1687

Boni, E., Bassi, L., Dallai, A., Guidi, F., Meacci, V., Ramalli, A., . . . Tortoli, P. (2016). ULA-OP 256: A 256-channel open scanner for development and real-time implementation of new ultrasound methods. *IEEE Transactions on Ultrasonics, Ferroelectrics, and Frequency Control, 63*(10), 1488-1495. doi:10.1109/TUFFC.2016.2566920

Brewin, M. P., Hijazi, Y., Pope-Jones, S., Exton, R. J., & Khan, M. S. (2020). Free tissue transfer for burns reconstruction: A single-site experience. *Burns, 46*(7), 1660-1667. doi:10.1016/j.burns.2020.04.001

Bui, D. T., Cordeiro, P. G., Hu, Q., Disa, J. J., Pusic, A., & Mehrara, B. J. (2007). Free flap reexploration: Indications, treatment, and outcomes in 1193 free flaps. *Plastic and Reconstructive Surgery, 119*(7), 2092-2100. doi:10.1097/01.prs.0000260598.24376.e1

Bullocks, J., Naik, B., Lee, E., & Hollier Jr, L. (2006). Flow-through flaps: A review of current knowledge and a novel classification system. *Microsurgery, 26*(6), 439-449. doi:10.1002/micr.20268

Cattari, N., Condino, S., Cutolo, F., Ferrari, M., & Ferrari, V. (2021). In situ visualization for 3D ultrasound-guided interventions with augmented reality headset. *Bioengineering, 8*(10), 131. doi:10.3390/bioengineering8100131

Chao, A. H., Meyerson, J., Povoski, S. P., & Kocak, E. (2013). A review of devices used in the monitoring of microvascular free tissue transfers. *Expert Review of Medical Devices, 10*(5), 649-660. doi:10.1586/17434440.2013.827527

Chee, A. J. Y., Ishii, T., Yiu, B. Y. S., & Yu, A. C. H. (2021). Helical toroid phantom for 3D flow imaging investigations. *Physics in Medicine & Biology, 66*(4), 045029. doi:10.1088/1361-6560/abda99

Chee, A. J. Y., Chung Kit Ho, Yiu, B. Y. S., & Yu, A. C. H. (2016). Walled carotid bifurcation phantoms for imaging investigations of vessel wall motion and blood flow dynamics. *IEEE Transactions on Ultrasonics, Ferroelectrics, and Frequency Control, 63*(11), 1852-1864. doi:10.1109/TUFFC.2016.2591946

Chen, K., Mardini, S., Chuang, D. C., Lin, C., Cheng, M., Lin, Y., . . . Wei, F. (2007). Timing of presentation of the first signs of vascular compromise dictates the salvage outcome of free flap transfers. *Plastic and Reconstructive Surgery, 120*(1), 187-195. doi:10.1097/01.prs.0000264077.07779.50

Chiao, R. Y., & Xiaohui Hao. (2005). Coded excitation for diagnostic ultrasound: A system developer's perspective. *IEEE Transactions on Ultrasonics, Ferroelectrics, and Frequency Control, 52*(2), 160-170. doi:10.1109/TUFFC.2005.1406543

Cho, S., Baik, J., Managuli, R., & Kim, C. (2020). 3D PHOVIS: 3D photoacoustic visualization studio. *Photoacoustics, 18,* 100168. doi:10.1016/j.pacs.2020.100168

Cobbold, R. S. C. (2007). *Foundations of biomedical ultrasound*. New York: Oxford University Press.

Correia, M., Maresca, D., Goudot, G., Villemain, O., Bizé, A., Sambin, L., . . . Pernot, M. (2020). Quantitative imaging of coronary flows using 3D ultrafast doppler coronary angiography. *Physics in Medicine & Biology, 65*(10), 105013. doi:10.1088/1361-6560/ab8d78

Correia, M., Provost, J., Tanter, M., & Pernot, M. (2016). 4D ultrafast ultrasound flow imaging: In vivo quantification of arterial volumetric flow rate in a single heartbeat. *Physics in Medicine & Biology, 61*(23), L48-L61. doi:10.1088/0031-9155/61/23/L48

Couture, O., Fink, M., & Tanter, M. (2012). Ultrasound contrast plane wave imaging. *IEEE Transactions on Ultrasonics, Ferroelectrics, and Frequency Control, 59*(12), 2676-2683. doi:10.1109/TUFFC.2012.2508

de Bray, J. M., Baud, J. M., & Dauzat, M. (1997). Consensus concerning the morphology and the risk of carotid plaques. *Cerebrovascular Diseases, 7*(5), 289-296. doi:10.1159/000108415

Demore, C. E. M., Joyce, A., Wall, K., & Lockwood, G. (2009). Real-time volume imaging using a crossed electrode array. *IEEE Transactions on Ultrasonics, Ferroelectrics, and Frequency Control, 56*(6), 1252-1261. doi:10.1109/TUFFC.2009.1167

Denis, B., Gourbeix, C., Coninckx, M., Foy, J., Bertolus, C., Constantin, J., & Degos, V. (2022). Maxillofacial free flap surgery outcomes in critical care: A single-center investigation looking for clues to improvement. *Perioperative Medicine, 11*(1), 11. doi:10.1186/s13741-022-00244-5

Diarra, B., Robini, M., Tortoli, P., Cachard, C., & Liebgott, H. (2013). Design of optimal 2-D nongrid sparse arrays for medical ultrasound. *IEEE Transactions on Biomedical Engineering, 60*(11), 3093-3102. doi:10.1109/TBME.2013.2267742

Díaz-Gómez, J. L., Mayo, P. H., & Koenig, S. J. (2021). Point-of-care ultrasonography. *The New England Journal of Medicine, 385*(17), 1593-1602. doi:10.1056/NEJMra1916062

Dong, J., Ai, D., Fan, J., Deng, Q., Song, H., Cheng, Z., . . . Yang, J. (2021). Local-global active contour model based on tensor-based representation for 3D ultrasound vessel segmentation. *Physics in Medicine & Biology, 66*(11), 115017. doi:10.1088/1361-6560/abfc92

Duan, X., Yu, A. C. H., & Wan, J. M. F. (2019). Cellular bioeffect investigations on low-intensity pulsed ultrasound and sonoporation: Platform design and flow cytometry protocol. *IEEE Transactions on Ultrasonics, Ferroelectrics, and Frequency Control, 66*(9), 1422-1434. doi:10.1109/TUFFC.2019.2923443

Duck, F. A. (2007). Medical and non-medical protection standards for ultrasound and infrasound. *Progress in Biophysics and Molecular Biology, 93*(1), 176-191. doi:10.1016/j.pbiomolbio.2006.07.008

Dunmire, B., Beach, K. W., Labs, K.-H., Plett, M., & Strandness, D. E. (2000). Cross-beam vector doppler ultrasound for angle-independent velocity measurements. *Ultrasound in Medicine and Biology,* 26(8), 1213-1235. doi:10.1016/S0301-5629(00)00287-8

Dusseldorp, J., & Pennington, D. (2014). Quantifying blood flow in the DIEP flap: An ultrasonographic study. *Plastic and Reconstructive Surgery, 2*(10), e228. doi:10.1097/GOX.0000000000000191

Ekroll, I. K., Swillens, A., Segers, P., Dahl, T., Torp, H., & Lovstakken, L. (2013). Simultaneous quantification of flow and tissue velocities based on multi-angle plane wave imaging. *IEEE Transactions on Ultrasonics, Ferroelectrics, and Frequency Control, 60*(4), 727-738. doi:10.1109/TUFFC.2013.2621

Fadnes, S., Ekroll, I. K., Nyrnes, S. A., Torp, H., & Lovstakken, L. (2015). Robust angle-independent blood velocity estimation based on dual-angle plane wave imaging. *IEEE Transactions on Ultrasonics, Ferroelectrics, and Frequency Control, 62*(10), 1757-1767. doi:10.1109/TUFFC.2015.007108

Fattal, R., & Lischinski, D. (2001, Oct 21). *Variational classification for visualization of 3D ultrasound data*. [Conference Paper] Proceedings of the conference on visualization '01, San Diego, CA, USA, 403-410. doi:10.1109/VISUAL.2001.964539

Fenster, A., Downey, D. B., & Cardinal, H. N. (2001). Three-dimensional ultrasound imaging. *Physics in Medicine and Biology, 46*(5), R67-R99.

Frey, G., & Chiao, R. (2008). 4Z1c real-time volume imaging transducer, *Whitepaper ACUSON SC2000 Volume Imaging Ultrasound System,* Siemens.

Gee, A., Prager, R., Treece, G., Cash, C., & Berman, L. (2004). Processing and visualizing three-dimensional ultrasound data. *British Journal of Radiology, 77*(2), S186-S193. doi:10.1259/bjr/80676194

Goddi, A., Bortolotto, C., Raciti, M. V., Fiorina, I., Aiani, L., Magistretti, G., . . . Calliada, F. (2018). High–Frame rate vector flow imaging of the carotid bifurcation in healthy adults: Comparison with color doppler imaging. *Journal of Ultrasound in Medicine, 37*(9), 2263-2275. doi:10.1002/jum.14579

Gran, F., Udesen, J., Nielsen, M., & Jensen, J. (2008). Coded ultrasound for blood flow estimation using subband processing. *IEEE Transactions on Ultrasonics, Ferroelectrics, and Frequency Control, 55*(10), 2211-2220. doi:10.1109/TUFFC.920

Hansen, P. M., Olesen, J. B., Pihl, M. J., Lange, T., Heerwagen, S., Pedersen, M. M., . . . Nielsen, M. B. (2014). Volume flow in arteriovenous fistulas using vector velocity ultrasound. *Ultrasound in Medicine & Biology, 40*(11), 2707-2714. doi:10.1016/j.ultrasmedbio.2014.06.004

Harput, S., Christensen-Jeffries, K., Ramalli, A., Brown, J., Zhu, J., Zhang, G., . . . Tang, M. (2020). 3-D super-resolution ultrasound imaging with a 2-D sparse array. *IEEE Transactions on Ultrasonics, Ferroelectrics, and Frequency Control, 67*(2), 269-277. doi:10.1109/TUFFC.2019.2943646

Ho, C. K., Chee, A. J. Y., Yiu, B. Y. S., Tsang, A. C. O., Chow, K. W., & Yu, A. C. H. (2017). Wall-less flow phantoms with tortuous vascular geometries: Design principles and a patient-specific model fabrication example. *IEEE Transactions on Ultrasonics, Ferroelectrics, and Frequency Control, 64*(1), 25-38. doi:10.1109/TUFFC.2016.2636129

Holbek, S., Christiansen, T. L., Stuart, M. B., Beers, C., Thomsen, E. V., & Jensen, J. A. (2016). 3-D vector flow estimation with row-column-addressed arrays. *IEEE Transactions on Ultrasonics, Ferroelectrics, and Frequency Control, 63*(11), 1799-1814. doi:10.1109/TUFFC.2016.2582536

Holbek, S., Ewertsen, C., Bouzari, H., Pihl, M. J., Hansen, K. L., Stuart, M. B., . . . Jensen, J. A. (2017a). Ultrasonic 3-D vector flow method for quantitative in vivo peak velocity and flow rate

estimation. *IEEE Transactions on Ultrasonics, Ferroelectrics, and Frequency Control, 64*(3), 544-554. doi:10.1109/TUFFC.2016.2639318

Holbek, S., Hansen, K. L., Bouzari, H., Ewertsen, C., Stuart, M. B., Thomsen, C., . . . Jensen, J. A. (2017b). Common carotid artery flow measured by 3-D ultrasonic vector flow imaging and validated with magnetic resonance imaging. *Ultrasound in Medicine & Biology, 43*(10), 2213-2220. doi:10.1016/j.ultrasmedbio.2017.06.007

Hoskins, P. R. (2010). Haemodynamics and blood flow measured using ultrasound imaging. Proceedings of the Institution of Mechanical Engineers. *Part H, Journal of Engineering in Medicine, 224*(2), 255-271. doi:10.1243/09544119JEIM572

Hoyt, K., Hester, F. A., Bell, R. L., Lockhart, M. E., & Robbin, M. L. (2009). Accuracy of volumetric flow rate measurements: An in vitro study using modern ultrasound scanners. *Journal of Ultrasound in Medicine, 28*(11), 1511-1518. doi:10.7863/jum.2009.28.11.1511

Hu, H., Huang, H., Li, M., Gao, X., Yin, L., Qi, R., . . . Xu, S. (2023). A wearable cardiac ultrasound imager. *Nature*, 613(7945), 667-675. doi:10.1038/s41586-022-05498-z

Huisman, R. M., van Dijk, M., de Bruin, C., Loonstra, J., Sluiter, W. J., Zeebregts, C. J., & van den Dungen, Jan J. A. M. (2005). Within-session and between-session variability of haemodialysis shunt flow measurements. *Nephrology, Dialysis, Transplantation, 20*(12), 2842-2847. doi:10.1093/ndt/gfi142

Hussain, S. T., Smith, R. E., Wood, R. F. M., & Bland, M. (1996). Observer variability in volumetric blood flow measurements in leg arteries using duplex ultrasound. *Ultrasound in Medicine & Biology, 22*(3), 287-291. doi:10.1016/0301-5629(95)02050-0

Icahn School of Medicine at Mount Sinai. (2019). What is a free flap? Retrieved from https://health.mountsinai.org/blog/what-is-a-free-flap-free-tissue-transfer-flap/

Jabir, S., Frew, Q., Magdum, A., El-Muttardi, N., Philp, B., & Dziewulski, P. (2015). Microvascular free tissue transfer in acute and secondary burn reconstruction. *Injury, 46*(9), 1821-1827. doi:10.1016/j.injury.2015.04.029

Jensen, J. A. (1997). Field: A program for simulating ultrasound systems. *Medical and Biological Engineering and Computing, 34*(1), 351-353.

Jensen, J. A., Holten-Lund, H., Nilsson, R. T., Hansen, M., Larsen, U. D., Domsten, R. P., . . . Rasmussen, M. F. (2013). SARUS: A synthetic aperture real-time ultrasound system. *IEEE Transactions on Ultrasonics, Ferroelectrics, and Frequency Control, 60*(9), 1838-1852. doi:10.1109/TUFFC.2013.2770

Jensen, J. A., & Svendsen, N. B. (1992). Calculation of pressure fields from arbitrarily shaped, apodized, and excited ultrasound transducers. *IEEE Transactions on Ultrasonics, Ferroelectrics, and Frequency Control, 39*(2), 262-267. doi:10.1109/58.139123

Jensen, J. A., Nikolov, S. I., Yu, A. C. H., & Garcia, D. (2016a). Ultrasound vector flow imaging-part I: Sequential systems. *IEEE Transactions on Ultrasonics, Ferroelectrics, and Frequency Control, 63*(11), 1704-1721. doi:10.1109/TUFFC.2016.2600763

Jensen, J. A., Nikolov, S. I., Yu, A. C. H., & Garcia, D. (2016b). Ultrasound vector flow imaging-part II: Parallel systems. *IEEE Transactions on Ultrasonics, Ferroelectrics, and Frequency Control, 63*(11), 1722-1732. doi:10.1109/TUFFC.2016.2598180

Johns Hopkins Medicine. (2023). *Reconstructive plastic surgery overview*. Johns Hopkins Medicine. https://www.hopkinsmedicine.org/health/treatment-tests-and-therapies/reconstructive-plastic-surgery-overview

Kasai, C., Namekawa, K., Koyano, A., & Omoto, R. (1985). Real-time two-dimensional blood flow imaging using an autocorrelation technique. *IEEE Transactions on Sonics and Ultrasonics, 32*(3), 458-464. doi:10.1109/T-SU.1985.31615

Kenny, J. S., Munding, C. E., Eibl, A. M., & Eibl, J. K. (2022). Wearable ultrasound and provocative hemodynamics: A view of the future. *Critical Care, 26*(1), 1-329. doi:10.1186/s13054-022-04206-7

Kenny, J. S., Munding, C. E., Eibl, J. K., Eibl, A. M., Long, B. F., Boyes, A., . . . Demore, C. E. M. (2021). A novel, hands-free ultrasound patch for continuous monitoring of quantitative doppler in the carotid artery. *Scientific Reports, 11*(1), 7780. doi:10.1038/s41598-021-87116-y

Khundkar, R. (2019). Lower extremity flap coverage following trauma. *Journal of Clinical Orthopaedics and Trauma, 10*(5), 839-844. doi:10.1016/j.jcot.2019.08.007

Kino, G. S., & DeSilets, C. S. (1979). Design of slotted transducer arrays with matched backings. *Ultrasonic Imaging, 1*(3), 189-209. doi:10.1016/0161-7346(79)90016-6

Knoedler, S., Hoch, C. C., Huelsboemer, L., Knoedler, L., Stögner, V. A., Pomahac, B., . . . Colen, D. (2023). Postoperative free flap monitoring in reconstructive surgery-man or machine? *Frontiers in Surgery, 10*, 1130566. doi:10.3389/fsurg.2023.1130566

Koepple, C., Kallenberger, A., Pollmann, L., Hundeshagen, G., Schmidt, V., Kneser, U., & Hirche, C. (2019). Comparison of fasciocutaneous and muscle-based free flaps for soft tissue reconstruction of the upper extremity. *Plastic and Reconstructive Surgery, 7*(12), e2543. doi:10.1097/GOX.0000000000002543

Kwok, A. C., & Agarwal, J. P. (2017). An analysis of free flap failure using the ACS NSQIP database. does flap site and flap type matter? *Microsurgery, 37*(6), 531-538. doi:10.1002/micr.30121

La, T., & Le, L. H. (2022). Flexible and wearable ultrasound device for medical applications: A review on materials, structural designs, and current challenges. *Advanced Materials Technologies, 7*(3), n/a. doi:10.1002/admt.202100798

Lee, K., & Mun, G. (2016). Volumetric planning using computed tomographic angiography improves clinical outcomes in DIEP flap breast reconstruction. *Plastic and Reconstructive Surgery, 137*(5), 771e-780e. doi:10.1097/PRS.0000000000002045

Lenge, M., Ramalli, A., Tortoli, P., Cachard, C., & Liebgott, H. (2015). Plane-wave transverse oscillation for high-frame-rate 2-D vector flow imaging. *IEEE Transactions on Ultrasonics, Ferroelectrics, and Frequency Control, 62*(12), 2126-2137. doi:10.1109/TUFFC.2015.007320

Leow, C. H., Bazigou, E., Eckersley, R. J., Yu, A. C. H., Weinberg, P. D., & Tang, M. (2015). Flow velocity mapping using contrast enhanced high-frame-rate plane wave ultrasound and image tracking: Methods and initial in Vitro and in Vivo evaluation. *Ultrasound in Medicine & Biology, 41*(11), 2913-2925. doi:10.1016/j.ultrasmedbio.2015.06.012

Lese, I., Biedermann, R., Constantinescu, M., Grobbelaar, A. O., & Olariu, R. (2021). Predicting risk factors that lead to free flap failure and vascular compromise: A single unit experience with 565 free tissue transfers. *Journal of Plastic, Reconstructive & Aesthetic Surgery, 74*(3), 512-522. doi:10.1016/j.bjps.2020.08.126

Lin, M., Zhang, Z., Gao, X., Bian, Y., Wu, R. S., Park, G., . . . Xu, S. (2023). A fully integrated wearable ultrasound system to monitor deep tissues in moving subjects. *Nature Biotechnology,* doi:10.1038/s41587-023-01800-0

Lookwood, G. R., & Foster, F. S. (1996). Optimizing the radiation pattern of sparse periodic two-dimensional arrays. *IEEE Transactions on Ultrasonics, Ferroelectrics, and Frequency Control, 43*(1), 15-19. doi:10.1109/58.484458

Macovski, A. (1979). Ultrasonic imaging using arrays. *Proceedings of the IEEE, 67*(4), 484-495. doi:10.1109/PROC.1979.11278

Maffett, R., Boni, E., Chee, A. J. Y., Yiu, B. Y. S., Savoia, A. S., Ramalli, A., . . . Yu, A. C. H. (2022). Unfocused field analysis of a density-tapered spiral array for high-volume-rate 3-D ultrasound imaging. *IEEE Transactions on Ultrasonics, Ferroelectrics, and Frequency Control, 69*(10), 2810-2822. doi:10.1109/TUFFC.2022.3188245

Martínez-Graullera, O., Martín, C. J., Godoy, G., & Ullate, L. G. (2010). 2D array design based on fermat spiral for ultrasound imaging. *Ultrasonics, 50*(2), 280-289. doi:10.1016/j.ultras.2009.09.010

Masoumi, M. H., Kaddoura, T., & Zemp, R. J. (2023). Costas sparse 2-D arrays for high-resolution ultrasound imaging. *IEEE Transactions on Ultrasonics, Ferroelectrics, and Frequency Control, 70*(5), 460-472. doi:10.1109/TUFFC.2023.3256339

Mattesini, P., Ramalli, A., Petrusca, L., Basset, O., Liebgott, H., & Tortoli, P. (2020). Spectral doppler measurements with 2-D sparse arrays. *IEEE Transactions on Ultrasonics, Ferroelectrics, and Frequency Control, 67*(2), 278-285. doi:10.1109/TUFFC.2019.2944090

Merritt, C. R. B. (1987). Doppler color flow imaging. *Journal of Clinical Ultrasound, 15*(9), 591-597. doi:10.1002/jcu.1870150904

Misaridis, T., & Jensen, J. A. (2005a). Use of modulated excitation signals in medical ultrasound. part I: Basic concepts and expected benefits. *IEEE Transactions on Ultrasonics, Ferroelectrics, and Frequency Control, 52*(2), 177-191. doi:10.1109/TUFFC.2005.1406545

Misaridis, T., & Jensen, J. A. (2005b). Use of modulated excitation signals in medical ultrasound. part II: Design and performance for medical imaging applications. *IEEE Transactions on Ultrasonics, Ferroelectrics, and Frequency Control, 52*(2), 192-207. doi:10.1109/TUFFC.2005.1406546

Misaridis, T., & Jensen, J. A. (2005c). Use of modulated excitation signals in medical ultrasound. part III: High frame rate imaging. *IEEE Transactions on Ultrasonics, Ferroelectrics, and Frequency Control, 52*(2), 208-219. doi:10.1109/TUFFC.2005.1406547

Mishra, D., Chaudhury, S., Sarkar, M., & Soin, A. S. (2019). Ultrasound image segmentation: A deeply supervised network with attention to boundaries. *IEEE Transactions on Biomedical Engineering, 66*(6), 1637-1648. doi:10.1109/TBME.2018.2877577

Mitchell, D. G. (1990). Color doppler imaging: Principles, limitations, and artifacts. *Radiology, 177*(1), 1-10. doi:10.1148/radiology.177.1.2204956

Montaldo, G., Tanter, M., Bercoff, J., Benech, N., & Fink, M. (2009). Coherent plane-wave compounding for very high frame rate ultrasonography and transient elastography. *IEEE Transactions on Ultrasonics, Ferroelectrics, and Frequency Control, 56*(3), 489-506. doi:10.1109/TUFFC.2009.1067

Morton, C. E., & Lockwood, G. R. (2003, Oct 5-8). *Theoretical assessment of a crossed electrode 2-D array for 3-D imaging*. [Conference Paper]. IEEE Symposium on Ultrasonics, Honolulu, HI, USA, 968-971. doi:10.1109/ULTSYM.2003.1293560

Muth, S., Dort, S., Sebag, I. A., Blais, M., & Garcia, D. (2011). Unsupervised dealiasing and denoising of color-doppler data. *Medical Image Analysis, 15*(4), 577-588. doi:10.1016/j.media.2011.03.003

Nahas, H., Au, J. S., Ishii, T., Yiu, B. Y. S., Chee, A. J. Y., & Yu, A. C. H. (2020). A deep learning approach to resolve aliasing artifacts in ultrasound color flow imaging. *IEEE Transactions on Ultrasonics, Ferroelectrics, and Frequency Control, 67*(12), 2615-2628. doi:10.1109/TUFFC.2020.3001523

Nelson, T. R., & Elvins, T. T. (1993, Nov 1,). Visualization of 3D ultrasound data. *IEEE Computer Graphics and Applications, 13*, 50-57. doi:10.1109/38.252557

Nelson, T., & Bailey, M. (2000, Apr 12). *Solid object visualization of 3D ultrasound data*. [Conference Paper]. Proceedings of SPIE 3982, Medical Imaging 2000: Ultrasonic Imaging and Signal Processing, San Diego, CA, USA. doi: 10.1117/12.382245

Oelze, M. L. (2007). Bandwidth and resolution enhancement through pulse compression. *IEEE Transactions on Ultrasonics, Ferroelectrics, and Frequency Control, 54*(4), 768-781. doi:10.1109/TUFFC.2007.310

Pedersen, M. H., Misaridis, T. X., & Jensen, J. A. (2003). Clinical evaluation of chirp-coded excitation in medical ultrasound. *Ultrasound in Medicine & Biology, 29*(6), 895-905. doi:10.1016/S0301-5629(02)00784-6

Petrusca, L., Varray, F., Souchon, R., Bernard, A., Chapelon, J., Liebgott, H., . . . Viallon, M. (2018). Fast volumetric ultrasound B-mode and doppler imaging with a new high-channels density platform for advanced 4D cardiac imaging/therapy. *Applied Sciences, 8*(2), 200. doi:10.3390/app8020200

Pihl, M. J., & Jensen, J. A. (2014). A transverse oscillation approach for estimation of three-dimensional velocity vectors, part I: Concept and simulation study. *IEEE Transactions on Ultrasonics, Ferroelectrics, and Frequency Control, 61*(10), 1599-1607. doi:10.1109/TUFFC.2013.006237

Pihl, M., Stuart, M., Tomov, B., Rasmussen, M., & Jensen, J. (2014). A transverse oscillation approach for estimation of three-dimensional velocity vectors, part II: Experimental validation. *IEEE Transactions on Ultrasonics, Ferroelectrics, and Frequency Control, 61*(10), 1608-1618. doi:10.1109/TUFFC.2013.006238

Pohlenz, P., Klatt, J., Schön, G., Blessmann, M., Li, L., & Schmelzle, R. (2012). Microvascular free flaps in head and neck surgery: Complications and outcome of 1000 flaps. *International Journal of Oral and Maxillofacial Surgery, 41*(6), 739-743. doi:10.1016/j.ijom.2012.02.012

Provost, J., Papadacci, C., Arango, J. E., Imbault, M., Fink, M., Gennisson, J., . . . Pernot, M. (2014). 3D ultrafast ultrasound imaging in vivo. *Physics in Medicine & Biology, 59*(19), L1-L13. doi:10.1088/0031-9155/59/19/L1

Ramalli, A., Boni, E., Giangrossi, C., Mattesini, P., Dallai, A., Liebgott, H., & Tortoli, P. (2021). Real-time 3-D spectral doppler analysis with a sparse spiral array. *IEEE Transactions on Ultrasonics, Ferroelectrics, and Frequency Control, 68*(5), 1742-1751. doi:10.1109/TUFFC.2021.3051628

Ramalli, A., Boni, E., Savoia, A. S., & Tortoli, P. (2015). Density-tapered spiral arrays for ultrasound 3-D imaging. *IEEE Transactions on Ultrasonics, Ferroelectrics, and Frequency Control, 62*(8), 1580-1588. doi:10.1109/TUFFC.2015.007035

Ramnarine, K. V., Nassiri, D. K., Hoskins, P. R., & Lubbers, J. (1998). Validation of a new blood-mimicking fluid for use in doppler flow test objects. *Ultrasound in Medicine & Biology, 24*(3), 451-459. doi:10.1016/S0301-5629(97)00277-9

Risser, C., Welsch, H. J., Fonfara, H., Hewener, H., & Tretbar, S. (2016, Sept 18-21). *High channel count ultrasound beamformer system with external multiplexer support for ultrafast 3D/4D ultrasound*. [Conference Paper]. 2016 IEEE International Ultrasonics Symposium, Tours, France. doi: 10.1109/ULTSYM.2016.7728714

Rose, J., & Puckett, Y. (2023). Breast reconstruction free flaps. *StatPearls [Internet]*, Treasure Island, FL, USA. https://www.ncbi.nlm.nih.gov/books/NBK541048/

Rossi, S., Ramalli, A., Fool, F., & Tortoli, P. (2020). High-frame-rate 3-D vector flow imaging in the frequency domain. *Applied Sciences, 10*(15), 5365. doi:10.3390/app10155365

Roux, E., Ramalli, A., Liebgott, H., Cachard, C., Robini, M. C., & Tortoli, P. (2017). Wideband 2-D array design optimization with fabrication constraints for 3-D US imaging. *IEEE Transactions on Ultrasonics, Ferroelectrics, and Frequency Control, 64*(1), 108-125. doi:10.1109/TUFFC.2016.2614776

Roux, E., Ramalli, A., Tortoli, P., Cachard, C., Robini, M. C., & Liebgott, H. (2016). 2-D ultrasound sparse arrays multidepth radiation optimization using simulated annealing and spiral-array inspired energy functions. *IEEE Transactions on Ultrasonics, Ferroelectrics, and Frequency Control, 63*(12), 2138-2149. doi:10.1109/TUFFC.2016.2602242

Roux, E., Varray, F., Petrusca, L., Cachard, C., Tortoli, P., & Liebgott, H. (2018). Experimental 3-D ultrasound imaging with 2-D sparse arrays using focused and diverging waves. *Scientific Reports, 8*(1), 9108-12. doi:10.1038/s41598-018-27490-2

Rubin, J. M. (1999). Flow quantification. *European Radiology*, *9*(Suppl 3), S368-S371. https://doi.org/10.1007/PL00014076

Rubino, C., Ramakrishnan, V., Figus, A., Bulla, A., Coscia, V., & Cavazzuti, M. A. (2009). Flap size/flow rate relationship in perforator flaps and its importance in DIEAP flap drainage. *Journal of Plastic, Reconstructive & Aesthetic Surgery, 62*(12), 1666-1670. doi:10.1016/j.bjps.2008.05.045

Saaristo, A. M., Niemi, T. S., Viitanen, T. P., Tervala, T. V., Hartiala, P., & Suominen, E. A. (2012). Microvascular breast reconstruction and lymph node transfer for postmastectomy lymphedema patients. *Annals of Surgery, 255*(3), 468-473. doi:10.1097/SLA.0b013e318242675

Saber, A. Y., Hohman, M. H. & Dreyer, M. A. (2022). Basic flap design. *StatPearls,* Treasure Island, FL, USA. https://www.ncbi.nlm.nih.gov/books/NBK563252/

Salgado, C. J., Moran, S. L., & Mardini, S. (2009). Flap monitoring and patient management. *Plastic and Reconstructive Surgery (1963), 124*(6 Suppl), e295-e302. doi:10.1097/PRS.0b013e3181bcf07b

Santos, P., Haugen, G. U., Lovstakken, L., Samset, E., & D'hooge, J. (2016). Diverging wave volumetric imaging using subaperture beamforming. *IEEE Transactions on Ultrasonics, Ferroelectrics, and Frequency Control, 63*(12), 2114-2124. doi:10.1109/TUFFC.2016.2616172

Sato, Y., Nakamoto, M., Tamaki, Y., Sasama, T., Sakita, I., Nakajima, Y., . . . Tamura, S. (1998). Image guidance of breast cancer surgery using 3-D ultrasound images and augmented reality visualization. *IEEE Transactions on Medical Imaging, 17*(5), 681-693. doi:10.1109/42.736019

Sauvage, J., Flesch, M., Férin, G., Nguyen-Dinh, A., Porée, J., Tanter, M., . . . Deffieux, T. (2018). A large aperture row column addressed probe for in vivo 4D ultrafast doppler ultrasound imaging. *Physics in Medicine & Biology, 63*(21), 215012. doi:10.1088/1361-6560/aae427

Savord, B. J. (2000). *Beamforming methods and apparatus for three-dimensional ultrasound imaging using two-dimensional transducer array* (U.S. Patent No. 6,013,032). U.S. Patent and Trademark Office. https://patents.google.com/patent/US6013032A/en

Schulte zu Berge, C., Baust, M., Kapoor, A., & Navab, N. (2014). Predicate-based focus-and-context visualization for 3D ultrasound. *IEEE Transactions on Visualization and Computer Graphics, 20*(12), 2379-2387. doi:10.1109/TVCG.2014.2346317

Schwarz, C., Mitterbauer, C., Boczula, M., Maca, T., Funovics, M., Heinze, G., . . . Oberbauer, R. (2003). Flow monitoring: Performance characteristics of ultrasound dilution versus color doppler ultrasound compared with fistulography. *American Journal of Kidney Diseases, 42*(3), 539-545. doi:10.1016/S0272-6386(03)00786-8

Steenbeek, L. M., Peperkamp, K., Ulrich, D. J. O., & Hummelink, S. (2022). Alternative imaging technologies for perforator mapping in free flap breast reconstructive surgery – A comprehensive overview of the current literature. *Journal of Plastic, Reconstructive & Aesthetic Surgery, 75*(11), 4074-4084. doi:10.1016/j.bjps.2022.06.100

Šteňo, A., Jezberová, M., Hollý, V., Timárová, G., & Šteňo, J. (2016). Visualization of lenticulostriate arteries during insular low-grade glioma surgeries by navigated 3D ultrasound power doppler: Technical note. *Journal of Neurosurgery, 125*(4), 1016-1023. doi:10.3171/2015.10.JNS151907

Savoia, A. S., Matrone, G., Bardelli, R., Bellutti, P., Quaglia, F., Caliano, G., . . . Sautto, M. (2018, Oct 22-25). *A 256-element spiral CMUT array with integrated analog front end and transmit beamforming circuits*. [Conference Paper] 2018 IEEE International Ultrasonics Symposium, Kobe, Japan. 206-212. doi:10.1109/ULTSYM.2018.8579867

Tanter, M., & Fink, M. (2014). Ultrafast imaging in biomedical ultrasound. *IEEE Transactions on Ultrasonics, Ferroelectrics, and Frequency Control, 61*(1), 102-119. doi:10.1109/TUFFC.2014.2882

Trucco, A. (1999). Thinning and weighting of large planar arrays by simulated annealing. *IEEE Transactions on Ultrasonics, Ferroelectrics, and Frequency Control, 46*(2), 347-355. doi:10.1109/58.753023

Turnbull, D. H., & Foster, F. S. (1991). Beam steering with pulsed two-dimensional transducer arrays. *IEEE Transactions on Ultrasonics, Ferroelectrics, and Frequency Control, 38*(4), 320-333. doi:10.1109/58.84270

Varandas, J., Baptista, P., Santos, J., Martins, R., & Dias, J. (2004). VOLUS—a visualization system for 3D ultrasound data. *Ultrasonics, 42*(1), 689-694. doi:10.1016/j.ultras.2003.11.006

von Ramm, O. T., & Smith, S. W. (1990). Real time volumetric ultrasound imaging system. *Journal of Digital Imaging, 3*(4), 261-266. doi:10.1007/BF03168124

Wang, C., Chen, X., Wang, L., Makihata, M., Liu, H., Zhou, T., & Zhao, X. (2022). Bioadhesive ultrasound for long-term continuous imaging of diverse organs. *Science, 377*(6605), 517-523. doi:10.1126/science.abo2542

Wehner, D. R. (1995). High resolution radar (2. ed., 1. print. ed.). Boston, Mass. [u.a.]: Artech House.

Wigen, M. S., Fadnes, S., Rodriguez-Molares, A., Bjastad, T., Eriksen, M., Stensath, K. H., . . . Lovstakken, L. (2018). 4-D intracardiac ultrasound vector flow imaging-feasibility and comparison to phase-contrast MRI. *IEEE Transactions on Medical Imaging, 37*(12), 2619-2629. doi:10.1109/TMI.2018.2844552

Yatchenko, A. M., Krylov, A. S., Sandrikov, V. A., & Kulagina, T. Y. (2014). Regularizing method for phase antialiasing in color doppler flow mapping. *Neurocomputing (Amsterdam), 139*, 77-83. doi:10.1016/j.neucom.2013.09.060

Yen, J. T., Steinberg, J. P., & Smith, S. W. (2000). Sparse 2-D array design for real time rectilinear volumetric imaging. *IEEE Transactions on Ultrasonics, Ferroelectrics, and Frequency Control, 47*(1), 93-110. doi:10.1109/58.818752

Yiu, B. Y. S., Tsang, I. K. H., & Yu, A. C. H. (2011). GPU-based beamformer: Fast realization of plane wave compounding and synthetic aperture imaging. *IEEE Transactions on Ultrasonics, Ferroelectrics, and Frequency Control, 58*(8), 1698-1705. doi:10.1109/TUFFC.2011.1999

Yiu, B. Y. S., Walczak, M., Lewandowski, M., & Yu, A. C. H. (2019). Live ultrasound color-enhanced speckle imaging platform for real-time complex flow visualization in vivo. *IEEE Transactions on Ultrasonics, Ferroelectrics, and Frequency Control, 66*(4), 656-668. doi:10.1109/TUFFC.2019.2892731

Yiu, B. Y. S., & Yu, A. C. H. (2016). Least-squares multi-angle doppler estimators for plane-wave vector flow imaging. *IEEE Transactions on Ultrasonics, Ferroelectrics, and Frequency Control, 63*(11), 1733-1744. doi:10.1109/TUFFC.2016.2582514

Yiu, B. Y. S., Lai, S. S. M., & Yu, A. C. H. (2014). Vector projectile imaging: Time-resolved dynamic visualization of complex flow patterns. *Ultrasound in Medicine & Biology, 40*(9), 2295-2309. doi:10.1016/j.ultrasmedbio.2014.03.014

Yiu, B. Y. S., & Yu, A. C. H. (2013). High-frame-rate ultrasound color-encoded speckle imaging of complex flow dynamics. *Ultrasound in Medicine & Biology, 39*(6), 1015-1025. doi:10.1016/j.ultrasmedbio.2012.12.016

Yu, A., & Lovstakken, L. (2010). Eigen-based clutter filter design for ultrasound color flow imaging: A review. *IEEE Transactions on Ultrasonics, Ferroelectrics and Frequency Control, 57*(5), 1096-1111. doi:10.1109/TUFFC.2010.1521

Appendix A
List of Movies

This appendix lists the video files referenced in this dissertation.

Movie 3-1.mp4: CFI cineloop of the carotid bifurcation phantom imaged with (a) ChiVE with the CH6 pulse and (b) lag-one autocorrelation with the ST5 pulse. It can be observed that ChiVE successfully prevents CFI aliasing artifacts in the flow jet at peak systole. It is also observed that the estimation variance in the lower branch of the bifurcation is reduced with ChiVE. See Section 3.5.4 for interpretation.

Movie 4-1.mp4: Wavefront propagation from 20 to 40mm depth for 1° steered PW, 0° steered DIV30, and 0° steered DIV20 transmissions. The white lines indicate the outline of the expected main beam area based on the array size, steering, and transmission type. It can be observed that the wavefront profile remains smooth throughout propagation. Additionally, some secondary lobes and comet tails are observed. See section 4.3.2 for interpretation.

Movie 4-2.mp4: Wavefront propagation from 20 to 40mm depth for 10° steered PW, 10° steered DIV30, and 10° steered DIV20 transmissions. The white lines indicate the outline of the expected main beam area based on the array size, steering, and transmission type. The wavefront in the main beam remains smooth throughout propagation as in Movie 4-1. The side lobe levels are notably higher with steering than in Movie 4-1. See section 4.3.2 for interpretation.

Movie 5-1.mp4: Vector flow maps of the aneurysm phantom with pulsatile flow on (a) a slice parallel with the ICA inlet vessel, and (b) a slice parallel to the MCA and PCA outlet vessels. Pre-systole an outlet jet toward the PCA is observed which changes direction away from the outlet as systole approaches. At peak systole, a strong flow jet from the ICA is observed which results in flow recirculation on the inlet plane. Throughout the cardiac cycle, a constant flow is observed toward the MCA outlet and there is some flow separation on the outlet plane. See section 5.3.3 for interpretation.

Appendix B

Full Table of RMSE Values from 3D VFI Parametric Sweep

Table B-1 RMSE Values for 4mL/s flow in 3.5mm ID straight tube with 5° elevational steering. All values are in cm/s.

Azimuth spacing \ # Angles	3	4	5	6	7	8	9	10
15°	164.2±312.4	75.2±138.3	42.0±95.7	29.6±59.2	28.6±38.8	26.1±29.7	20.9±26.1	16.3±23.1
30°	46.7±99.6	28.3±41.7	21.3±30.2	12.1±22.3	11.4±16.6	10.3±13.5	9.5±11.4	9.4±10.4
45°	31.0±49.6	16.5±24.7	11.4±17.3	9.3±13.4	9.0±111.5	9.0±10.6	\	\
60°	20.9±33.9	14.1±18.2	9.5±13.1	9.3±11.7	\	\	\	\
75°	13.9±25.3	10.9±15.2	11.0±13.1	\	\	\	\	\
90°	12.0±20.2	9.9±14.4	\	\	\	\	\	\
105°	12.6±16.8	11.5±14.5	\	\	\	\	\	\
120°	12.7±15.9	\	\	\	\	\	\	\
135°	12.4±16.5	\	\	\	\	\	\	\
150°	16.0±21.8	\	\	\	\	\	\	\
165°	18.7±35.5	\	\	\	\	\	\	\

Table B-2 RMSE Values for 4mL/s flow in 3.5mm ID straight tube with 7.5° elevational steering. All values are in cm/s.

Azimuth spacing

 # Angles

	3	4	5	6	7	8	9	10
15°	232.7±272.7	102.1±115.1	61.9±78.9	38.3±48.1	24.2±32.4	21.2±24.1	21.4±20.8	18.5±18.5
30°	63.1±82.7	26.8±36.0	23.5±24.9	18.3±18.1	10.8±12.4	10.6±10.1	9.1±8.7	9.0±7.9
45°	24.9±39.1	19.0±21.3	11.6±12.3	9.3±10.7	8.9±8.8	8.9±8.2		
60°	20.5±28.1	12.3±14.0	8.0±10.2	7.7±9.1				
75°	19.7±20.1	10.0±12.3	9.3±10.7					
90°	12.7±15.0	10.3±10.5						
105°	13.4±12.4	11.9±10.7						
120°	8.7±12.5							
135°	11.1±13.6							
150°	12.6±18.0							
165°	20.8±27.8							

Table B-3 RMSE Values for 4mL/s flow in 3.5mm ID straight tube with 10° elevational steering. All values are in cm/s.

Azimuth spacing

 # Angles

	3	4	5	6	7	8	9	10
15°	216.2±315.2	95.7±133.0	77.5±87.7	53.2±54.3	37.0±43.7	31.5±27.8	33.4±25.8	29.5±22.4
30°	73.5±90.9	37.6±49.2	35.8±31.3	28.3±20.6	21.1±15.1	18.5±13.1	15.8±10.9	15.6±9.2
45°	38.5±49.2	31.0±28.1	21.1±16.9	16.9±15.3	15.4±11.3	15.7±10.6		
60°	31.8±34.3	18.0±17.2	16.4±13.2	16.7±11.6				
75°	29.1±22.1	15.6±16.0	15.6±13.6					
90°	22.0±19.5	18.2±12.5						
105°	18.4±14.5	16.5±12.8						
120°	15.9±16.4							
135°	16.0±15.2							
150°	19.5±19.4							
165°	49.8±32.8							

Table B-4 RMSE Values for 2mL/s flow in 3.5mm ID straight tube with 5° elevational steering. All values are in cm/s.

Azimuth spacing

 # Angles

	3	4	5	6	7	8	9	10
15°	70.3±151.3	27.4±69.6	19.0±50.6	12.5±33.1	12.3±22.7	7.5±17.0	8.0±14.4	8.1±12.6
30°	16.5±52.1	13.5±24.9	8.7±16.7	7.5±11.5	6.7±8.5	6.5±6.8	6.1±5.7	6.0±5.3
45°	12.7±27.0	8.8±13.6	6.5±8.6	6.2±6.6	6.0±5.7	6.2±5.2		
60°	8.7±18.9	7.2±9.2	6.0±6.6	5.8±5.8				
75°	8.7±13.7	6.5±7.4	6.5±6.4					
90°	6.3±10.9	5.7±7.3						
105°	7.0±9.0	7.4±7.4						
120°	7.4±8.2							
135°	7.2±8.5							
150°	6.6±10.3							
165°	7.5±17.4							

Table B-5 RMSE Values for 2mL/s flow in 3.5mm ID straight tube with 7.5° elevational steering. All values are in cm/s.

Azimuth spacing

 # Angles

	3	4	5	6	7	8	9	10
15°	36.1±107.8	18.5±48.3	14.0±33.7	13.6±22.4	10.6±16.1	10.8±12.3	12.1±9.9	9.7±8.3
30°	15.7±34.6	11.5±17.6	12.4±11.6	10.4±8.0	9.2±6.1	9.3±4.8	9.6±4.0	9.6±3.7
45°	10.6±19.1	8.7±9.7	8.8±6.5	9.0±4.7	9.2±4.1	9.3±3.7		
60°	12.3±12.8	9.3±6.6	9.5±4.7	9.2±4.0				
75°	10.0±9.5	9.9±5.3	9.8±4.5					
90°	9.6±8.1	9.8±5.4						
105°	8.8±6.5	9.1±5.4						
120°	9.0±5.6							
135°	8.4±6.0							
150°	10.7±7.0							
165°	10.1±11.7							

Table B-6 RMSE Values for 2mL/s flow in 3.5mm ID straight tube with 10° elevational steering. All values are in cm/s.

Azimuth spacing

 # Angles

	3	4	5	6	7	8	9	10
15°	5.51±109.9	23.1±47.8	18.6±31.3	18.8±20.4	16.4±14.2	17.6±11.4	16.9±8.8	18.8±7.4
30°	19.8±32.8	15.9±15.6	16.1±9.9	19.2±6.9	15.8±5.2	14.9±4.2	15.3±3.5	15.5±3.2
45°	16.3±16.8	18.9±8.7	15.9±5.7	15.3±4.1	15.7±3.5	15.5±3.1		
60°	16.4±11.0	13.8±5.9	14.4±4.2	14.4±3.6				
75°	18.5±8.3	14.9±4.5	15.3±3.8					
90°	14.1±6.7	14.8±4.7						
105°	12.7±6.0	12.9±4.9						
120°	14.2±5.0							
135°	18.8±5.5							
150°	18.8±6.2							
165°	19.8±11.4							

Table B-7 RMSE Values for 1mL/s flow in 2mm ID straight tube with 5° elevational steering. All values are in cm/s.

Azimuth spacing

 # Angles

	3	4	5	6	7	8	9	10
15°	94.5±162.9	44.2±72.0	35.2±63.5	41.6±38.6	30.5±23.8	19.6±19.2	14.0±18.7	14.4±17.3
30°	43.3±6.5	29.9±23.9	14.2±21.9	11.9±15.1	9.6±11.4	9.0±9.3	7.7±7.9	7.7±7.3
45°	31.7±31.0	16.1±16.6	9.2±11.5	8.5±9.0	8.1±7.7	8.0±7.1		
60°	16.3±11.6	10.3±12.1	8.0±8.9	7.8±7.8				
75°	9.9±13.5	8.8±9.7	8.3±8.5					
90°	9.9±11.4	8.6±9.4						
105°	9.0±11.0	9.4±10.0						
120°	8.0±11.0							
135°	10.1±11.4							
150°	10.9±15.3							
165°	20.4±26.0							

Table B-8 RMSE Values for 1mL/s flow in 2mm ID straight tube with 7.5° elevational steering. All values are in cm/s.

Azimuth spacing

 # Angles

	3	4	5	6	7	8	9	10
15°	163.7±152.1	31.7±61.2	23.0±45.8	21.7±28.1	12.4±17.9	15.4±14.3	10.6±13.6	9.6±12.1
30°	22.8±45.9	13.8±19.1	10.6±15.9	9.1±10.7	8.7±7.9	9.5±6.5	9.3±5.6	9.3±5.1
45°	14.6±23.2	11.6±12.2	9.2±8.0	8.9±6.3	9.0±5.4	8.9±5.1		
60°	10.8±17.5	9.2±8.8	9.1±6.4	8.8±5.8				
75°	9.4±12.3	9.7±7.1	9.6±6.4					
90°	10.6±9.3	10.4±6.5						
105°	11.1±8.0	11.0±7.1						
120°	9.8±8.1							
135°	10.5±8.2							
150°	10.5±11.1							
165°	16.4±17.5							

Table B-9 RMSE Values for 1mL/s flow in 2mm ID straight tube with 10° elevational steering. All values are in cm/s.

Azimuth spacing

 # Angles

	3	4	5	6	7	8	9	10
15°	95.3±121.3	26.3±53.9	32.9±36.1	20.7±22.6	15.3±16.4	13.4±12.4	12.9±10.5	10.5±9.0
30°	30.6±37.7	12.5±17.6	12.7±11.9	12.2±8.1	12.1±6.5	12.3±5.3	11.3±4.6	11.4±4.1
45°	20.1±19.2	11.5±9.7	12.8±6.7	12.2±5.2	11.8±4.5	11.8±4.1		
60°	11.7±13.1	12.4±7.2	10.7±5.4	10.6±4.7				
75°	13.0±9.6	12.0±5.7	11.7±4.9					
90°	13.8±7.9	12.3±5.7						
105°	13.1±6.6	11.8±5.6						
120°	10.5±6.7							
135°	12.0±6.5							
150°	15.0±8.6							
165°	25.9±15.2							